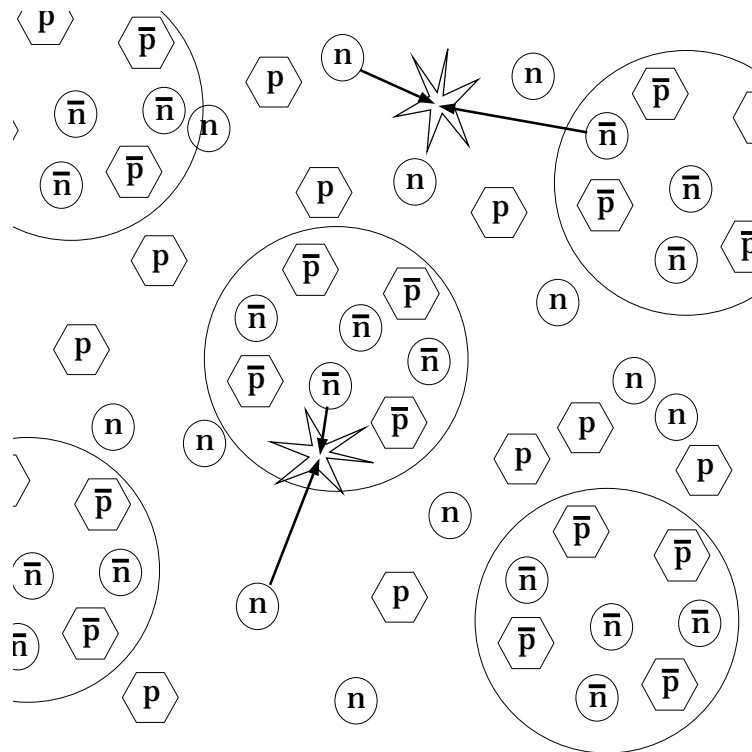


The Influence of Matter-Antimatter Domains on Big Bang Nucleosynthesis



Dissertation der Fakultät für Physik
der
Ludwig-Maximilians-Universität München

vorgelegt von
Jan Bernhard Rehm
aus München

München, den 15. Februar 2000

1. Gutachter:
2. Gutachter:
Tag der mündlichen Prüfung:

Priv.-Doz. Dr. habil. Peter Schneider
Prof. Dr. Harald Lesch
26. Juni 2000

Contents

1 Zusammenfassung	5
Introduction	9
2 Antimatter in the Universe	13
2.1 Is the Universe Baryo-Symmetric?	13
2.2 Antimatter in Today's Universe?	15
2.3 Antimatter in the Early Universe	18
3 Big Bang Nucleosynthesis	23
3.1 Thermodynamics of the Early Universe	23
3.2 Element Synthesis	25
3.3 Observations	29
3.4 Discussion	35
4 Annihilation of Antimatter Domains in the Early Universe	37
4.1 Setting the Stage	38
4.2 Diffusive and Hydrodynamic Processes	40
4.2.1 Pressure Equilibrium	40
4.2.2 Baryon Diffusion	42
4.2.3 Heat Diffusion and Hydrodynamic Expansion	44
4.3 Matter-Antimatter Annihilation	47
4.3.1 Annihilation Cross Sections	47
4.3.2 Secondaries in Nucleon-Nucleon Annihilations	52
4.3.3 Secondaries in Nucleon-Nucleus Annihilations	53
5 BBN with Antimatter	61
5.1 Initial Conditions	61
5.2 The Annihilation Region	62
5.3 Annihilations Well Before Weak Freeze Out	67
5.4 Annihilations Between Weak Freeze Out and ^4He Synthesis	70
5.5 Late Time Annihilation	74
5.6 Modified Abundances	79

6 Big Bang Nucleosynthesis and Antimatter	
– Summary and Conclusions –	87
Appendix: Numerical Methods	93
Bibliography	99

Chapter 1

Zusammenfassung

In der vorliegenden Arbeit habe ich mich mit den Auswirkungen eventuell im frühen Universum vorhandener Antimaterieregionen auf die Häufigkeiten der leichten Elemente beschäftigt.

Praktisch das gesamte Deuterium und der überwiegende Teil der Helium-4 Kerne, die wir heute im Universum beobachten, wurden in einem frühen Evolutionsstadium des Kosmos — nur wenige Minuten nach dem Urknall — gebildet. In der Theorie der sogenannten *Primordialen Nukleosynthese* — oder auch *Big Bang Nukleosynthese (BBN)* — werden die relativen Häufigkeiten der einzelnen Kerne abhängig von den genauen physikalischen Bedingungen im jungen Universum vorhergesagt. Die im Rahmen des Standardmodells der Kosmologie vorhergesagten Elementhäufigkeiten stimmen im Allgemeinen gut mit aus Beobachtungen abgeleiteten Werten überein. Dies begründet den großen Erfolg dieser Theorie und macht sie zu einem der Grundpfeiler des kosmologischen Standardmodells.

Denkbare Erweiterungen des Standardmodells können jedoch potentiell Auswirkungen auf den Ablauf der Kernsynthese haben. Da aber jedes glaubwürdige Szenario ebenso wie die Standardtheorie die aus den Beobachtungen abgeleiteten Häufigkeiten vorhersagen muss, dürfen die Häufigkeiten nur minimal beeinflusst werden. Diese Überlegungen gestatten es uns, die Kernsynthese als „Werkzeug“ zur Untersuchung der physikalischen Bedingungen im jungen Universum zu verwenden. Dies ist bereits in der Vergangenheit vielfach praktiziert worden. Eine häufig untersuchte Variante ist die sogenannte *inhomogene* Nukleosynthese. In einem solchen Modell wird eine Grundannahme des kosmologischen Standardmodells, die Homogenität der Verteilung der baryonischen Materie im jungen Universum, fallengelassen. Das von mir untersuchte Szenario geht noch einen Schritt weiter und läßt auch Fluktuationen in der Baryonendichte mit negativem Vorzeichen zu. In einem solchen Modell besteht das junge Universum aus getrennten Materie- und Antimaterieregionen. Diese Art spezieller Anfangsbedingungen wird in einigen Modellen der elektroschwachen Baryogenese vorhergesagt. Solche Materie- und Antimaterieregionen werden sich gegenseitig annihilieren, sobald der Transport von Baryonen über die Grenzen der Regionen möglich ist. Nach der vollständigen Annihilation aller Antimaterieregionen bleibt nur der im

Zuge der Baryogenese gebildete Überschuß an Materie übrig.

Zur numerischen Behandlung dieses Problems habe ich ein Computerprogramm entwickelt. In diesem Programm werden sowohl die nuklearen Reaktionen, die zum Aufbau der leichten Elemente führen, als auch Annihilationen berücksichtigt. Da die Kernsynthese und die Annihilation der Antimaterieregionen im expandierenden Universum ablaufen, und die genauen Werte der einzelnen thermodynamischen Variablen, wie Druck, Dichte und Temperatur der beteiligten Teilchen, von entscheidender Wichtigkeit sind, muss das Programm auf dem Hintergrund der Expansion des Kosmos gerechnet werden. Weiterhin musste neben den Reaktionen, die zwischen den einzelnen Nukleonen ablaufen können, auch der Transport von Nukleonen und Antinukleonen in die jeweilige Anti-Region behandelt werden. Diese Transportprozesse werden zu frühen Zeiten durch Diffusion von Baryonen beschrieben, zu späten Zeiten hingegen durch hydrodynamische Expansion von Regionen mit höherer Dichte gegen solche mit niedrigerer Dichte.

Abhängig vom Zeitpunkt der Annihilation können die Häufigkeiten der leichten Elemente durch zwei Haupteffekte beeinflusst werden. Im Zuge der Heliumsynthese, die bei einer kosmischen Temperatur von etwa 80 keV abläuft, werden praktisch alle freien Neutronen in Helium-4 Kerne eingebaut. Die primordiale Helium-4 Häufigkeit hängt also stark von der Anzahl verfügbarer Neutronen ab. Zu Zeiten vor der Heliumsynthese läuft der Transport von Baryonzahl über die Domänengrenzen durch Neutronendiffusion ab, Protonen können auf Grund ihrer elektrischen Ladung nur über wesentlich kürzere Distanzen diffundieren. Frühe Annihilation wird also bevorzugt auf Neutronen stattfinden und führt so zu einer Reduzierung der Neutronendichte, und damit unmittelbar auch zu einer geringeren Menge an primordial produziertem Helium-4. Sind die Antimaterieregionen größer als die Diffusionslänge von Neutronen zur Zeit der Heliumsynthese, ist ein nennenswerter Transport von Baryonzahl erst zu wesentlich späteren Zeiten möglich. Antiprotonen, die nun in die Materieregion eindringen, können sowohl auf Protonen als auch auf die bereits gebildeten Helium-4 Kerne annihilieren. Weiterhin können die Helium-4 Kerne auch durch die im Annihilationprozess entstehenden Gammaquanten photodisintegriert werden. Beide Prozesse führen zur Bildung energetischer Sekundärkerne, in erster Linie Helium-3. Diese energetischen Kerne können in einem weiteren Schritt durch nicht-thermische Reaktionen mit Helium-4 Kernen Lithium-6 Kerne bilden. Späte Annihilation wird also zu einer erhöhten Helium-3 und Lithium-6 Häufigkeit im Vergleich zum Standardszenario führen.

Als ein wichtiges Ergebnis meiner Arbeit habe ich auf Grund dieser Effekte Schranken sowohl an den maximal erlaubten Antimateriegehalt im jungen Universum, als auch an den Zeitpunkt der Annihilation, bestimmt durch die Größe der Antimaterieregionen, hergeleitet. Diese neuen und rigiden Schranken decken einen weiten Annihilationszeitraum ab, von der Epoche des Ausfrierens der schwachen Wechselwirkungen bei einer Temperatur von etwa 1 MeV bis hinunter zur Epoche der Rekombination bei einer kosmischen Temperatur von etwa 10^{-7} MeV. Im Vergleich zu bisher existierenden Schranken für diese Epoche der kosmischen Entwicklung, beispielsweise auf Grund von Beobachtungen der kosmischen Hintergrundstrahlung, sind meine Ergeb-

nisse wesentlich restriktiver. Der relative Antimateriegehalt in Regionen die unmittelbar nach dem Ende der Kernsynthese annihilieren kann beispielsweise nicht höher als wenige Prozent der gesamten baryonischen Materie sein, für spätere Annihilation sinkt dieser Wert um mehr als zwei Größenordnungen. In einem zweiten Hauptaspekt meiner Arbeit habe ich gezeigt, dass die durchaus im Detail vorhandenen Diskrepanzen zwischen den im Standardszenario der Big Bang Nukleosynthese vorhergesagten Elementhäufigkeiten und den aus Beobachtungen abgeleiteten Werten durch die Präsenz einer gewissen Menge Antimaterie in einem bestimmten Längenskalenbereich beseitigt werden können. Weiterhin habe ich untersucht, ob die im Standardszenario gültige obere Grenze für die Baryondichte im Universum in einem Szenario mit Antimateriedomänen ebenso gültig ist. Auf Grund meiner Ergebnisse erscheint es sehr unwahrscheinlich, dass die Baryondichte in einem Materie-Antimaterie Szenario wesentlich größer sein kann, als im Standardszenario vorhergesagt.

Introduction

In the past decades our knowledge of two fundamental fields of physics on very different scales, namely particle physics on the one hand and cosmology on the other, has enormously increased. In particle physics, phenomena on the smallest accessible length scales are studied at very high energies, whereas in cosmology we are mostly concerned with gravitational interactions at rather low energies over very long distances. The physics of the early Universe, however, may only be understood if know-how from both fields is combined. This connection between inner space and outer space is consummated in the rapidly developing field of astro-particle physics.

The earliest connection between particle physics and cosmology in the history of science is probably the theory of the formation of helium and the other light elements up to lithium in the early Universe, usually designated Big Bang Nucleosynthesis (BBN), which I will discuss in some detail in Chapter 3. BBN predicts the formation of about 25 % (by mass) ^4He , a few $\times 10^{-5}$ deuterium and ^3He nuclei relative to hydrogen and $\mathcal{O}(10^{-10})$ ^7Li . The precise abundances depend on the particle content and the expansion history of the early Universe, and on the contribution of baryons to the density of the Universe. Within the cosmological and particle physics standard model, the first two ingredients are well known and thus the only parameter of a standard BBN calculation is the baryon density. The predicted abundances agree reasonably well with values deduced from observations of the element abundances in stars and other astrophysical objects for a certain range of the baryon density. It is thus possible to infer an upper limit on the baryon density in the Universe from BBN considerations. The success of BBN makes it one of the three pillars supporting the cosmological standard model, together with the cosmic microwave background radiation (CMBR; the ‘echo of the Big Bang’) and the recession of the galaxies. Within this model, the Universe is believed to have its origin in an initial singularity, the Big Bang, about 10^{10} years back in time. The subsequent evolution from this very hot and dense state proceeds by adiabatic expansion of the primordial plasma. For this reason, the cosmic temperature T instead of the time t is commonly used to describe the time evolution of the early Universe. Matter, as is observed in stars and galaxies today, is only a negligible contamination in this primordial soup.

Besides its role as evidence for the correctness of the cosmological standard model, BBN is a powerful tool to scrutinize a wide range of ideas for physics beyond the standard model. Any physical theory which affects the evolution of the Universe has to predict the elemental abundances inferred from observations. No other mechanism to

synthesize the observed amounts of especially helium and deuterium apart from thermonuclear burning in a radiation dominated dense and hot plasma is known. Therefore all extensions or modifications of the standard model have to allow for such a phase in the evolution of the Universe, or present another yet unknown successful nucleosynthesis scenario.

Another important field of interest at the crossroad of high-energy physics and cosmology is the question how the matter we and everything else in the observable Universe is made of came into being. A tiny fraction of a second after the Big Bang, the very early Universe consisted of a plasma of particles and antiparticles, which were constantly annihilated into and created from light. In thermodynamic equilibrium, the creation of particles and antiparticles has equal probability. When the energy of the photons, which is given by the cosmic temperature, drops below the rest mass of some species, creation of that species ends and particles and antiparticles eventually annihilate, leaving behind only a very small residual out-of-equilibrium abundance. Thus a Universe which was always very close to thermodynamic equilibrium would be a rather dull and boring place today, consisting of a thermal background of photons and neutrinos and about one proton and antiproton for every 10^{20} photons. Clearly, this cannot be the whole story, since we see about one proton per 10^{10} photons and practically no antiprotons in the Universe. In the 1960's it has been shown that such an excess of matter over antimatter may have been created during temporary deviations from thermodynamic equilibrium, e.g. during phase transitions, which occurred in the early Universe. Today's Universe would thus consist of this excess of matter, which survived the catastrophic annihilation. The process of baryogenesis is however still not fully understood.

Some models for baryogenesis predict not just an excess of matter over antimatter, but separated regions in space, in which the creation of either matter or antimatter is favoured. Thus, after annihilation of the thermally created particle-antiparticle pairs, domains of matter and antimatter emerge. Whenever transport of particles and antiparticles over the boundaries of these domains and thus mixing of matter and antimatter is possible, annihilation proceeds. Observational limits, which will be discussed in the first chapter, practically exclude the existence of such domains today, unless they are about as large as the currently observable Universe. Nevertheless, antimatter domains on much smaller scales, which would have had annihilated in the early Universe, are not excluded on observational grounds. In order to explain the dominance of matter we observe today, this class of baryogenesis models also has to create a net excess of baryons over antibaryons, which remains after complete antimatter annihilation. This could be accomplished by models predicting a smaller fraction of space filled with antimatter than with matter. Such regions should be sufficiently small, so that they annihilate in the early Universe, and leave behind the already imprinted net baryon number.

Such small-scale antimatter regions present in the early Universe may drastically modify the standard picture of the Big Bang Universe, in particular BBN and thus the predicted element abundances, but have as yet not been constrained in detail. In Chapter 4, I will set the stage for discussing the evolution of small-scale antimatter regions and the impact they have on BBN. Further, I will describe the relevant physical pro-

cesses, such as baryon diffusion, heat transport and nucleonic annihilation.

The detailed results of this study, the influence of antimatter domains on BBN, will be presented in Chapter 5. Annihilation of antimatter domains at different times during the evolution of the early Universe may have different consequences. At early times, prior to the formation of ${}^4\text{He}$, annihilation will mainly proceed via neutrons. The decrease of the neutron abundance may result in a significantly reduced ${}^4\text{He}$ mass fraction as compared to the standard BBN scenario. Antimatter domains may however be of a typical size such that annihilation is delayed until after ${}^4\text{He}$ synthesis. In this case, annihilation proceeds mainly via protons and antiprotons. Reprocessing of the now abundant light elements either via annihilations or via production from secondary particles arising in the annihilation process may also modify the abundances. In both cases, stringent constraints on the presence of antimatter in the early Universe may thus be derived. The last chapter is dedicated to summary and conclusions. I will compare my new constraints on the allowed amount of annihilation, as well as the allowed maximum size of antimatter regions with other limits. It will turn out that my new results allow one to constrain the presence of antimatter more tightly than previously possible, e.g. on grounds of the measurements of the cosmic microwave background radiation. Further, I will show, that for some combinations of the antimatter parameters the agreement between the predicted and observationally inferred abundances may even be improved. Despite the possible reduction of the primordial ${}^4\text{He}$ mass fraction, it is however unlikely that a scenario with matter-antimatter domains may reconcile a Universe at a baryonic density which exceeds the bound from standard BBN with the observationally inferred values for the light element abundances.

Chapter 2

Antimatter in the Universe

With the advent of quantum physics in the first decades of the 20th century, it became clear that most particles come in pairs. Solving the equation he developed to describe electrons, Dirac (1930, 1931) found solutions corresponding to particles with negative energies. This feature led to the hypothesis of the existence of the positron as the antiparticle of the electron, which was eventually discovered by Anderson (1933) some years later. After the discovery of the antiproton (Chamberlain, Segre, Wiegand & Ypsilantis 1955), the question if and how much antimatter is present in the Universe has stimulated much observational and theoretical effort. Today, the concept of particles and antiparticles is an integral part of modern particle physics and has been widely tested experimentally. Particles and antiparticles obey the same laws of physics; only one case is known, the K^0 , where particles and their anti-partners show a different behaviour. One would therefore expect similar abundances of matter and antimatter in the Universe, but despite great effort, which will be described in Sec. 2.2 and 2.3, no evidence for any substantial amount of antimatter in the Universe has been found. Thus the question arises, why is there no antimatter present in the Universe we observe? Or, to be more precise, why do we not live in a baryo-symmetric Universe and thus do not see the same amount of antimatter as we see of matter?

2.1 Is the Universe Baryo-Symmetric?

The Universe is believed to have evolved from a very hot and dense initial state, the Big Bang, which is initially in thermodynamic equilibrium. Since the equilibrium abundances for particles and antiparticles of one species, e.g. protons and antiprotons, are identical, we generically expect equal amounts of matter and antimatter. When the interaction rates for a species fall below the Hubble expansion rate of the Universe, particles and antiparticles of that species eventually annihilate on each other and leave behind a residual freeze out abundance. For baryons, this would be the case at a temperature of about 20 MeV and would result in extremely low number densities for baryons and antibaryons of the order of $n/s = \mathcal{O}(10^{-20})$ relative to the entropy density of the Universe s (see e.g. Kolb & Turner 1990). This baryo-symmetric scenario is however

not realised, since we know from the theory of Standard Big Bang Nucleosynthesis that $n/s = \mathcal{O}(10^{-10})$, see Sec. 3. The question posed above should therefore be rephrased; Why do we see so much matter around us?

One solution would be to start with initial conditions such that the excess of matter over antimatter is just there from the beginning. Apart from being ‘unnatural’ in the sense that this could not be understood from first principles, it does not seem to be compatible with our current understanding of the evolution of the Universe. For several reasons, such as the horizon problem and the dilution of some ‘unwanted’ relics predicted by Grand Unified Theories (GUTs), a period of exponential expansion, so-called inflation, should have occurred in a very early phase of the history of the Universe. Such an exponential expansion would erase any pre-existing asymmetry in the baryon number. After the inflationary epoch, the Universe is typically reheated to a temperature less than or of order of 10^{12} GeV.

In the context of an initially baryo-symmetric Universe, there are in principle two different possibilities to end up with the world we see. One possibility is that matter and antimatter were actually created in equal amounts, but some still unknown mechanism has separated them on very large scales. Up to now, no plausible and working physical model in which such a separation would occur has been found. Observational searches for antimatter indicate that this scale should be nearly as large as the observable part of the Universe today.

The alternative explanation for baryogenesis is that there were temporary deviations from thermodynamic equilibrium in the early Universe, as for example during phase transitions, in which an excess of matter over antimatter in the initially symmetric Universe was created. After annihilation of all the thermally created antimatter, some matter was left over. This baryo-asymmetric solution is currently favoured by cosmologists, even though the first scenario cannot be fully excluded on observational grounds.

Following a seminal paper by Sakharov (1967), much attention has been directed toward explaining the presently observed baryon number asymmetry as the natural result of the evolution of an initially symmetric Universe, thus avoiding the imposition of unnatural, asymmetric initial conditions or separation mechanisms. In this work, the three necessary ingredients for successful baryogenesis were formulated. (1) Breaking of charge (C) and combined charge and parity (CP) invariance, (2) Deviation from thermodynamic equilibrium in the primordial plasma, and (3) baryon number violation. The first explicit realisation of Sakharov’s original scenario came with the development of GUTs, which predict baryon number violation and possibly CP violation. But since it is believed today that the GUT scale is larger than the inflationary scale, GUT scale baryogenesis suffers from the same incompatibility with inflation as the ‘unnatural’ solution. The reheating temperature reached after inflation is too cool to reinstate the inflation-diluted baryon asymmetry through GUT processes.

Currently, the most promising baryogenesis scenario is probably still that of electroweak baryogenesis, mediated by baryon number violating sphaleron transitions. In this class of models baryogenesis takes place at the electroweak scale, at a temperature of $T_{EW} \approx 100$ GeV. At this stage during the evolution of the Universe the symmetry be-

tween electromagnetic and weak interactions is broken. If this phase transition is of first order, all three Sakharov criteria may be fulfilled. It has however now been established that the electroweak phase transition is not of first order, at least not in the minimal standard model. Nevertheless, electroweak baryogenesis may still be accomplished in extensions of the minimal standard model, such as a supersymmetric model. For a detailed discussion of the various baryogenesis scenarios the reader is referred to reviews written by e.g. Dolgov (1992), Cohen, Kaplan & Nelson (1993), and Riotto & Trodden (1999).

In some of the electroweak baryogenesis scenarios, domains containing predominantly matter or antimatter may emerge. This is not in conflict with the idea of explaining the observed baryon asymmetry of the Universe, since the net baryon-to-entropy ratio, $(n_b - n_{\bar{b}})/s$, is now different from zero, whereas prior to baryogenesis it was equal to zero. In the course of the evolution of the Universe, these domains annihilated, leaving behind the imprinted net baryon number. Annihilation of antimatter domains in the early Universe may lead to a highly non-standard cosmic evolution, as I will discuss in detail in this work.

2.2 Antimatter in Today's Universe?

Direct Searches. In the past, several direct searches for antimatter have been carried out. A very direct proof that our closest vicinity is not made out of antimatter are the successful landings of various spacecrafts on planets throughout the solar system, and of course the fact that the Apollo astronauts were able to make a second small step. More sophisticated searches using the balloon-borne spectrometer BESS to look for antimatter in cosmic rays have been performed. The first evidence for antiprotons in cosmic rays was reported by Golden et al. (1979) and Bogomolov et al. (1979), whereas the first unambiguous detection had to wait until the mid-nineties (Yoshimura et al. 1995, Mitchell et al. 1996, Moiseev et al. 1997, Boezio et al. 1997). The antiproton/proton ratio derived from these data is $\mathcal{O}(10^{-6})$ (Moiseev et al. 1997). No antiparticles heavier than protons have been found in any of these experiments; the most stringent upper limit on the presence of ${}^4\overline{\text{He}}$ is given by Saeki et al. (1998), ${}^4\overline{\text{He}}/{}^4\text{He} \lesssim 3 \times 10^{-6}$. The current limits for antimatter in cosmic rays are displayed in Fig. 2.1, which I borrowed from the original work. Further improvement on both antiproton and ${}^4\overline{\text{He}}$ data is expected from AMS, the Alpha Magnetic Spectrometer (Ahlen et al. 1994), which will be part of the International Space Station Alpha (ISSA) in the near future.

Since the observed antimatter-to-matter ratio is nowhere near unity, and furthermore no antinuclei with charge > 1 have been found, there is no evidence for a primary antimatter component. A primary component would have been produced either in the big bang, surviving annihilation in some isolated region, or by exotic elementary particle processes such as the decay of heavy supersymmetric particles or black hole evaporation. All cosmic ray data may be explained by secondary antiprotons, which stem from interactions of high-energy cosmic rays with the interstellar gas.

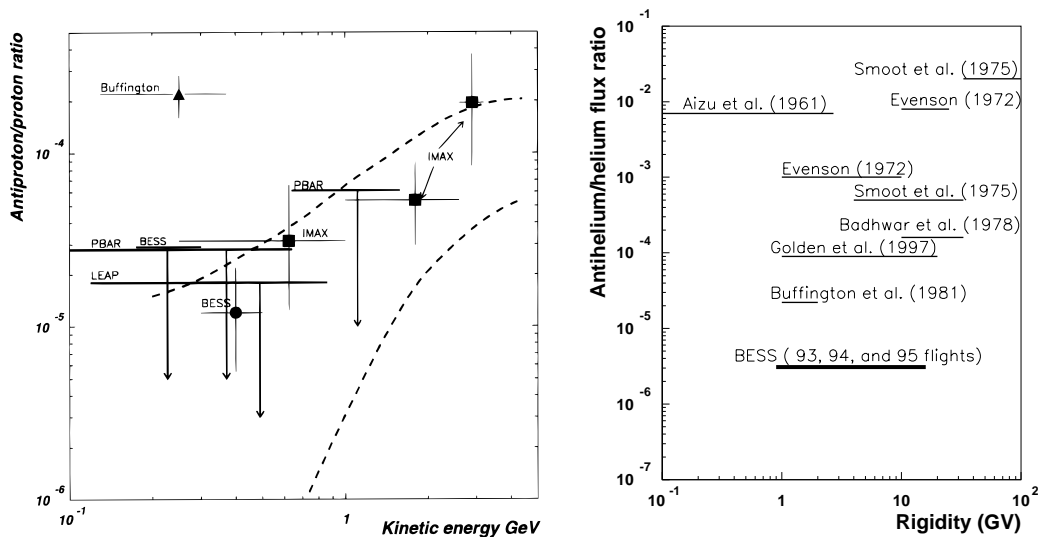


Figure 2.1: *Left panel:* Antiproton-to-proton ratio derived from cosmic ray observations (Moiseev et al. 1997). The dashed lines indicate the range which is predicted for antiprotons originating in cosmic rays in the 'leaky box' model (Gaisser & Schaefer 1992). *Right Panel:* Upper limits on the ${}^4\overline{\text{He}}/{}^4\text{He}$ ratio compatible with cosmic ray data (Saeki et al. 1998). The rigidity of a particle is defined as momentum/charge. (See original works for references)

There is thus no evidence for regions containing considerable amounts of antimatter within our own galaxy. The observations of cosmic rays can however not tell us about antimatter at extragalactic distances much larger than about 10 Mpc, since the travel time for cosmic rays over such distances should be longer than the Hubble time. Extragalactic domains of size 10–20 Mpc may therefore well be consistent with a null-result of the searches for ${}^4\overline{\text{He}}$ in cosmic rays (Ormes et al. 1997).

In order to distinguish between the two fundamentally different scenarios of baryosymmetry or -antisymmetry, information about the putative presence of antimatter on larger scales than those accessible with direct searches is needed.

Indirect searches. Indirect evidence for the existence or non-existence of antimatter in the Universe will turn out to be more helpful to derive limits on the allowed dimensions of antimatter domains, as was described in a comprehensive review by Steigman (1976). Whenever matter and antimatter come into contact, annihilation occurs and eventually energetic photons are produced. In order to obtain constraints, one therefore measures the flux of gamma-rays. These may or may not stem from annihilations of antimatter, so only upper limits on the amount of annihilations may be obtained. The absence of this annihilation radiation from within the solar system, from within the galaxy and from the neighbouring Virgo cluster shows that little antimatter is present within 20 Mpc of the solar system. This distance corresponds to the typical size of a galactic cluster. The non-observation of annihilation radiation from X-ray emitting clusters implies that

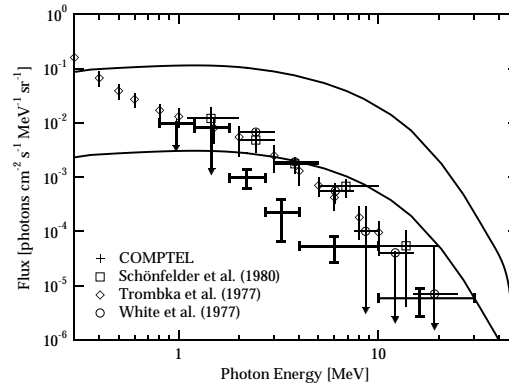


Figure 2.2: Observations of the diffuse gamma-ray background (Kappadath et al. 1996) and predictions for the flux resulting from annihilations of regions with size 20 Mpc (upper curve) and 1000 Mpc (lower curve). The predicted signal is inversely proportional to the size of the antimatter regions (Cohen, de Rújula & Glashow 1998)

these structures do not contain significant admixtures of matter and antimatter.

Photons resulting from annihilation of domains separated on even larger scales add to the cosmic diffuse gamma-ray radiation (CDG) and may distort the cosmic microwave background radiation (CMBR). In a recent paper, Cohen et al. (1998) studied the observable consequences of antimatter domains of size bigger than 20 Mpc today. These authors claim that there is an era of unavoidable annihilation of assumed regions of matter or antimatter. Putative voids separating these regions in the early Universe may be restricted to be of size ≈ 16 Mpc. Smaller voids should have been erased by Silk-damping by the time of recombination, whereas larger voids are in conflict with the observed uniformity of the CMBR. After the onset of structure formation, i.e. when fluctuations in the baryon density become large ($\delta\rho/\rho \approx 1$), matter and antimatter may again be separated. For these reasons, Cohen et al. (1998) calculated the contributions to the CMBR and CDG for annihilations occurring between recombination and the onset of structure formation. The resulting CMBR distortions are four times smaller than the distortions allowed by the data obtained with the FIRAS instrument on board the COBE satellite (Fixsen et al. 1996), therefore no such limit may be imposed. Concerning the contribution of the annihilation radiation to the CDG, the situation is more promising. I show the results of Cohen et al. (1998) in Fig. 2.2. For all domain sizes $\lesssim 1000$ Mpc, which is approximately the current size of the observable Universe, the predictions are in conflict with the observations reported by Kappadath et al. (1996). Note that it is not possible to exclude on these grounds the existence of small and distant pockets of antimatter (Dolgov & Silk 1993). Annihilation of antimatter domains during the epoch of recombination has been studied by Kinney, Kolb & Turner (1997) and Cohen & de Rújula (1998). Despite some differences in these studies, both predict ‘ribbon’- or ‘scar’-like structures on the CMBR which show a Sunyaev-Zel’dovich-type distortion of the order of 10^{-6} . In Fig. 2.3, a map of the CMBR with a pattern of matter and antimat-

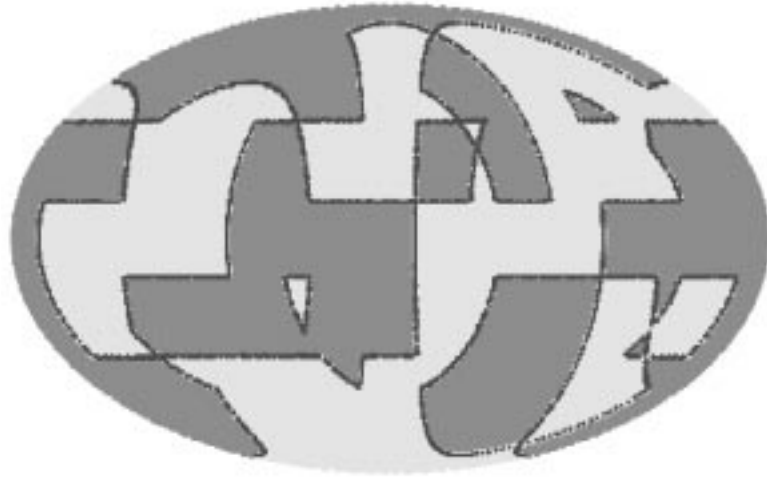


Figure 2.3: Map of the sky at the epoch of recombination with a pattern of matter and antimatter regions of typical size 2400 Mpc (for a Hubble constant of $100 \text{ km s}^{-1} \text{ Mpc}^{-1}$). Distortions of the CMBR spectrum are confined to the interfaces (taken from Kinney et al. 1997).

ter regions is shown. The spectral distortions are confined to the interfaces of these regions, the ‘scars’ or ‘ribbons’. Such small distortions are beyond the resolution of current CMBR observations, but may possibly be detectable with the planned experiments PLANCK or MAP. In summary, it seems very unlikely that we live in a Universe containing any considerable amount of antimatter today, whereas small scale domains of antimatter which have completely annihilated prior to recombination are not excluded by these findings.

2.3 Antimatter in the Early Universe

Since the annihilation of antimatter regions in the early Universe may lead to deviations from the cosmological standard model, it is subject to constraints derived from observations, as I will discuss below.

Distortions of the CMBR. In contrast to the case of large-scale antimatter regions present today, which are probably excluded, distortions of the CMBR by annihilations of small scale antimatter regions in the early Universe will provide valuable limits in some areas of the parameter space. From the results of the FIRAS instrument we have very detailed information on the nature of the CMBR. The CMBR spectrum as displayed in the left panel of Fig. 2.4 (Fixsen et al. 1996) is the most precise realisation of a black body spectrum ever measured. Any non-thermal energy input ΔU at redshifts $z \lesssim 3 \times 10^6$ is subject to tight constraints due to the very stringent limits on the allowed devia-

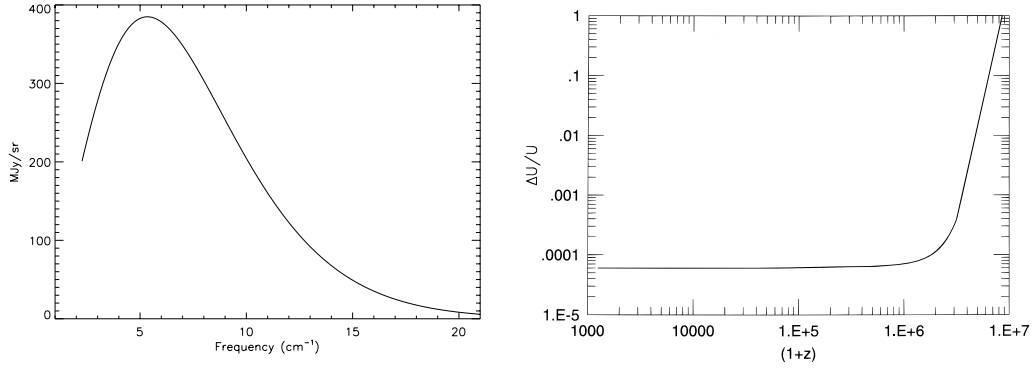


Figure 2.4: *Left panel:* Spectrum of the CMBR as measured by FIRAS. *Right panel:* Input of nonthermal energy into the CMBR compatible with the measured spectrum (both taken from Fixsen et al. 1996).

tions from a Planckian spectrum. Energy input above $z \gtrsim 10^7$ cannot be constrained using the CMBR, since double Compton scattering will thermalize arbitrarily large inputs of nonthermal energy (Sunyaev & Zel'dovich 1970, Lightman 1981, Danese & De Zotti 1982). During epochs with redshifts between $10^7 \gtrsim z \gtrsim 10^4$ non-thermal photons will reach thermal, but not chemical equilibrium with the blackbody photons via multiple Compton scattering. This equilibrium is described by a Bose-Einstein distribution with non-zero chemical potential $\mu_0 \propto \Delta U / U_{\text{CMBR}}$, where U_{CMBR} is the energy contained in the CMBR. The limits on $\Delta U / U_{\text{CMBR}}$ resulting from the observationally allowed spectral distortions in the CMBR are displayed in the right panel of Fig. 2.4 (Fixsen et al. 1996) Assuming that all the annihilation generated energy, apart from the fraction carried away by the already decoupled neutrinos, will interact and possibly distort the CMBR, we may derive limits on the fraction of antimatter annihilation at some specific redshift compatible with the observed spectrum. These limits will be presented together with my new limits obtained from BBN considerations in Sec. 6 of this work.

Limits on Antimatter from BBN Considerations. The synthesis of the light elements takes place at a temperature range of ~ 10 MeV to ~ 10 keV, corresponding to an age of the Universe of ~ 1 to $\sim 10^4$ s. The agreement of the abundances predicted by Big Bang Nucleosynthesis (BBN) and the abundances inferred from astrophysical observations is one of the big achievements of modern cosmology (see Sec. 3 for a short review and references). Since the predicted abundances are very sensitive to the exact physical conditions during that epoch, stringent constraints of new physics beyond the cosmological and particle physics standard model may be derived.

In particular, the ${}^4\text{He}$ mass fraction is mostly determined by the ratio of neutrons to protons at a temperature of ≈ 80 keV. If regions of matter and antimatter were present during that evolutionary stage, this ratio and thus the final ${}^4\text{He}$ mass fraction may be affected. Annihilation of antimatter domains during this epoch can only proceed via

neutron diffusion. Proton diffusion is greatly suppressed due to the electromagnetic interactions with the ambient plasma. If the size of the antimatter regions is of the order of the neutron diffusion length at this time, a substantial number of neutrons can diffuse out into the antimatter regions and annihilate there. These neutrons are therefore not available for ${}^4\text{He}$ synthesis and the final ${}^4\text{He}$ mass fraction is reduced. This loss of neutrons due to differential diffusion of neutrons and protons was already stressed by Steigman (1972). Combes, Fassi-Fehri & Leroy (1975) and Aly (1978) studied the nucleosynthesis process in the context of baryo-symmetric cosmologies and found that only very little annihilation is allowed prior to the BBN epoch, following Steigman's argument, but also after the BBN epoch due to disruption and photodisintegration of ${}^4\text{He}$. In these models mixing and thus annihilation was accomplished by a coalescence mechanism at the boundaries of matter and antimatter regions in a baryo-symmetric Universe.

But even much smaller amounts of antimatter of the order of 10 % or less of the baryon number in a baryo-asymmetric Universe may be excluded on these scales (Rehm & Jedamzik 1998). Most of the remainder of this work is dedicated to the interplay between antimatter domains and BBN and the reader is referred to Secs. 4, 5 and 6 for a thorough discussion.

BBN can however not only constrain the putative existence of antimatter domains, but also put limits on the existence of antimatter which came into being much later and independent of baryogenesis. Possible sources for antimatter are the decay of hypothetical heavy particles X , if hadronic decay channels are present, and the evaporation of primordial black holes (PBH). The determinant feature of both scenarios is the homogeneous and exponential — at least in the case of decaying particles — input of mesons and baryon-antibaryon pairs. Three different regimes have to be considered, appearance of these pairs prior to, during or after the epoch of BBN.

Baryon-antibaryon pairs generated by evaporating black holes were studied first by Zel'dovich, Starobinskii, Khlopov & Chechetkin (1977) and Vainer, Dryzhakova & Naselskii (1978). Pairs appearing at $T \approx 1 \text{ MeV}$ increase the neutron-to-proton ratio due to the predominant annihilation on protons, which are at this time several times more abundant than neutrons. This leads to an increase in the final ${}^4\text{He}$ mass fraction Y_p . Demanding that $Y_p \lesssim 0.4$, a limit on the relative antibaryon abundance of $n_{\bar{b}}/(n_n + n_p) < 1/20$ was derived. Black holes evaporating later were claimed to increase the deuterium abundance due to a second phase of deuterium production following the disruption of ${}^4\text{He}$ nuclei by energetic baryons and antibaryons. Two mechanisms were considered: direct deuterium originating in ${}^4\text{He}$ spallation and secondary deuterium production through energetic neutrons created in ${}^4\text{He}$ disruptions and rapidly captured by thermal protons.

A candidate for hadronically decaying particles which are predicted in supersymmetric GUTs is the gravitino, the superpartner of the graviton. A number of studies (Batusov et al. 1984, Khlopov & Linde 1984, Ellis, Nanopoulos & Sarkar 1985, Lindley 1986) have concentrated on late decaying gravitinos, where the dominant effect is the disruption of ${}^4\text{He}$ nuclei by antiprotons resulting in additional deuterium, tritium and ${}^3\text{He}$ nuclei. Owing to the fact that the observed mass fraction of ${}^4\text{He}$ is more than three

orders of magnitude higher than the mass fractions of the mass 2 and 3 nuclei, the destruction of a minute fraction of ${}^4\text{He}$ leads to a significant overproduction of these elements compared to the standard BBN scenario. Based on the first measurement of the $\bar{p}{}^4\text{He}$ reaction (Batusov et al. 1984), limits of the order of 10^{-3} on the allowed abundance of homogeneously distributed antimatter relative to matter after the completion of BBN have been derived, as was suggested earlier (Chechetkin, Khlopov, Sapozhnikov & Zel'dovich 1982b, Chechetkin, Khlopov & Sapozhnikov 1982a). A wider range of gravitino lifetimes was studied by Domínguez-Tenreiro (1987) and Halm (1987). These authors allowed for decay during and before the synthesis of the light elements which may lead to a substantial modification of the element abundances. The general trend found in these studies is — in accordance with the work discussed above — that deuterium and ${}^3\text{He}$ increase with increasing gravitino lifetime and abundance. The ${}^4\text{He}$ mass fraction is only affected for high gravitino abundances and decay times prior to BBN in an analogous way as described above for evaporating PBHs.

More generic scenarios for homogenous injection of antimatter before and during BBN were investigated subsequently by Domínguez-Tenreiro & Yepes (1987) and Yepes & Domínguez-Tenreiro (1988), motivated by the idea to reconcile a Universe dominated by baryonic dark matter with BBN. The standard BBN scenario limits the allowed range for the cosmic baryon density to a few percent of the critical density. Extensive variations of lifetime and abundance of the decaying particles were performed, which confirmed the results for deuterium, ${}^3\text{He}$ and ${}^4\text{He}$ just discussed. The patterns of ${}^7\text{Li}$ productions were found to be more complicated. The competition between several creation and destruction channels prevents a clear trend with the model parameters, as is the case for deuterium and ${}^3\text{He}$, and also ${}^4\text{He}$. Nevertheless, it was claimed that consistency with the observed abundances is achievable for the whole range of the cosmic baryon density from the standard BBN value up to the critical density.

Reno & Seckel (1988) concentrated on the effects hadrons injected during and before BBN have on the neutron-to-proton ratio. In addition to baryon-antibaryon pairs they considered meson-induced variations of the neutron-to-proton ratio. Competitive limits from mesons were only found for very short lifetimes $\tau_X \lesssim 1$ s. Only then the interaction times of the mesons are comparable to their own lifetimes.

In this thesis, I will discuss the limits on the presence of antimatter domains in the early Universe on various length scales, and for various values of the total matter-to-antimatter ratio prior to annihilation, in the context of a baryo-asymmetric Universe. Thus after annihilation is complete, the Universe will contain no antibaryon number and the baryon-to-photon ratio reflects the usual value.

Chapter 3

Big Bang Nucleosynthesis

The theory of Big Bang Nucleosynthesis (BBN) describes the formation of the light elements deuterium, ^3He , ^4He and lithium in an early evolutionary stage of the Universe. The standard version of this theory is based on four main assumptions: 1. The expansion of the Universe is described by the homogeneous and isotropic Friedmann-Robertson-Walker model. 2. The standard model of particle physics is used. 3. The lepton asymmetry of the Universe is of the same order as the baryon asymmetry so that chemical potentials of the different neutrino species in the early Universe are small relative to the temperature. 4. There are no baryon number fluctuations, in particular no regions of antimatter in the early Universe. BBN took place at an epoch between about 1 and 10^4 seconds after the initial singularity, the Big Bang. The cosmic temperature T dropped during this time from 10 MeV to about 10 keV. At that stage the energy density in ‘radiation’, i.e. in relativistic particles, exceeds the energy density of baryons by several orders of magnitude. Therefore the nuclear processes have no effect on the cosmic expansion, BBN proceeds on the ‘stage’ of the adiabatically expanding, radiation dominated Universe. The physical conditions of this ‘stage’ have however profound influence on the process of BBN. Before discussing the theory of BBN, I will therefore give a short overview of the thermal history of the Universe during the time relevant for BBN. For a more thorough discussion of both topics see e.g. Kolb & Turner (1990). Finally, I will discuss the problems of inferring the primordial abundances from observations and compare these with the ones obtained by theoretical calculations.

3.1 Thermodynamics of the Early Universe

Particle Content of the Primordial Plasma. The early Universe is filled with a mixture of elementary particles. During most of its history, the particles are in thermodynamic equilibrium. The abundances of the thermally created bosons and fermions are thus

given by their equilibrium distribution functions and their energy density is¹

$$\varepsilon_i = \left(\pi^2/30\right) g_i T^4 \times \begin{cases} 1 & \text{Bose – Einstein statistics} \\ (7/8) & \text{Fermi – Dirac statistics} \end{cases}, \quad (3.1)$$

where g_i is the number of degrees of freedom for the respective species. Equation (3.1) holds as long as the mass of a species is much smaller than the cosmic temperature T . The equilibrium number density for particles with rest mass $m > T$ is greatly suppressed, because particles and antiparticles annihilate on each other and cannot be reproduced any more from the thermal bath.

The total energy density of the early Universe is the sum of the energy densities of all of its constituents. Since the energy density of baryons is several orders of magnitude smaller than the energy density in radiation, it may safely be neglected. The contribution of the still unknown dark matter can not be larger than about ten times the energy density in baryons and is thus also negligible. The total energy density of the radiation dominated early Universe is therefore the energy density in relativistic particles

$$\begin{aligned} \varepsilon &= \sum_{i=\text{bosons}} g_i \frac{\pi^2}{30} T_i^4 + \frac{7}{8} \sum_{i=\text{fermions}} g_i \frac{\pi^2}{30} T_i^4 \\ &\equiv g_* \frac{\pi^2}{30} T^4, \end{aligned} \quad (3.2)$$

where it is understood that the sums run only over particles with $m \ll T$ and g_* is the effective number of relativistic degrees of freedom, to be discussed shortly. Thermodynamic equilibrium ceases to apply when the interaction rate of a species with the thermal bath drops below the Hubble expansion rate of the Universe. The distribution function of that species freezes out, but retains its shape until the present day. Therefore the contribution of that species to the cosmic energy density is still given by Eq. 3.1, provided the particles are still relativistic ($m \ll T$). The temperature describing the distribution function is however not necessarily the same as for the particles still in thermodynamic equilibrium. Heat generating processes may slow down the cooling of the plasma, but the decoupled species are not affected and their distribution function is described by a lower temperature. Therefore the definition of the effective relativistic degrees of freedom has to allow for different temperatures T_i of the species,

$$g_* \equiv \sum_{i=\text{bosons}} g_i \left(\frac{T_i}{T}\right)^4 + \frac{7}{8} \sum_{i=\text{fermions}} g_i \left(\frac{T_i}{T}\right)^4. \quad (3.3)$$

and the concept of a unique cosmic temperature is, strictly speaking, not applicable any more. What is usually meant by the term cosmic temperature is the photon temperature. The number density of some species, which is still coupled to the plasma, will be greatly diminished when the temperature of the cosmic plasma drops below its rest mass, and

¹Here and throughout this work I will use natural units where $\hbar = c = k = 1$, unless indicated otherwise.

it will become nonrelativistic. Therefore this species does not contribute any more to the sum in Eq. (3.2), and, due to the suppressed number density, its non relativistic energy density will not be significant compared to the total energy density of the early Universe. The evolution of the parameter g_* with temperature is shown in the left panel of Fig. 3.1. Below a temperature of about 10 MeV, the plasma consists of neutrinos, photons and electrons in thermodynamic equilibrium and $g_* = 10.75$. The neutrinos decouple from the thermal bath at about 1 MeV. Some time later, electron-positron pairs annihilate, since the cosmic temperature falls below their rest mass, and therefore drop out of Eq. 3.3 and g_* decreases. This leads to a slow down in the cooling of the Universe, which is not shared by the neutrinos. The neutrino background radiation, which is practically unmeasurable due to the extremely small neutrino interaction rates, has a temperature of 1.9 K today, whereas the photon background has a slightly higher energy density with $T \approx 2.75$ K. Due to this lower neutrino temperature the parameter $g_* = 3.36$ today, in contrast to 7.25, as would be the case for equal temperatures (cf. Eq. 3.3). The cosmic microwave background radiation (CMBR), which is experimentally verified and has been studied in great detail, is thus just the adiabatically cooled photon population, which was thermally generated in the very early Universe. The existence of the CMBR is very strong evidence for the correctness of the cosmological standard model sketched above.

Expansion of the Universe. The thermal history of the early Universe is that of an adiabatically expanding plasma consisting mostly of relativistic particles. The expansion of the Universe is parameterized by the Hubble-parameter H , which is defined as the ratio of the expansion velocity \dot{R} to the scale factor R . The time evolution of the Hubble-parameter is governed by the total energy density $\varepsilon(t)$ of the Universe and is described by the Friedmann equation,

$$H^2 \equiv \left(\frac{\dot{R}}{R} \right)^2 = \frac{8\pi G}{3} \varepsilon(t), \quad (3.4)$$

where G is the gravitational constant. At early times, the curvature term in the Friedmann equation is unimportant and has therefore been neglected in Eq. (3.4). The age of the Universe is approximately given by the inverse of the Hubble parameter, $t \approx H^{-1}$. During the radiation dominated phase ($t \lesssim 4 \times 10^{10}$ s) the total energy density $\varepsilon \propto g_* T^4$ and

$$t \approx 1 \text{ s} \left(\frac{T}{\text{MeV}} \right)^{-2}$$

during times where g_* is approximately constant.

3.2 Element Synthesis

Neutrons and protons do not appear on the cosmic stage until the quark-gluon plasma of the early Universe is confined to baryons and mesons during the QCD, or quantum

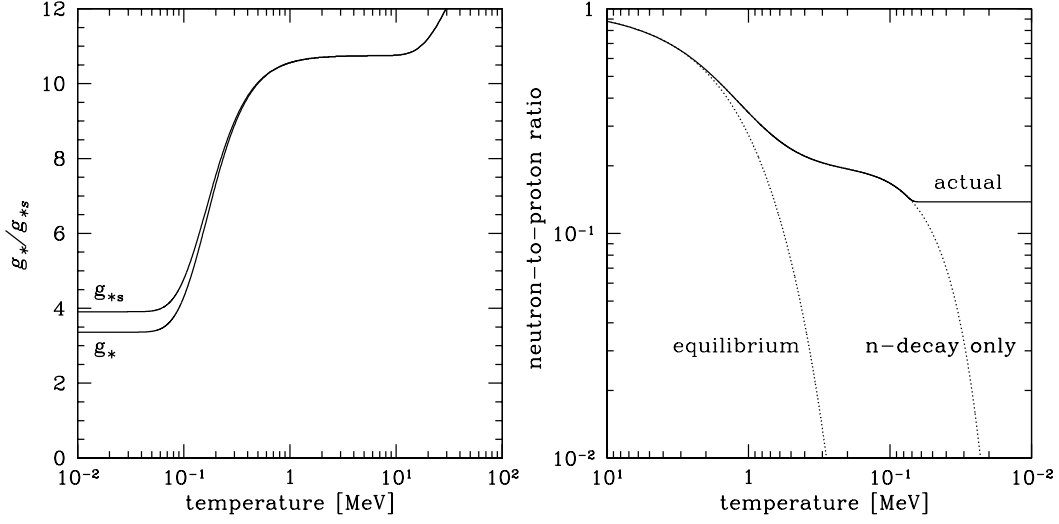


Figure 3.1: *Left panel:* Evolution of the number of effective relativistic degrees of freedom with temperature. *Right Panel:* Neutron-to-proton ratio during weak freeze out and the BBN epoch. The curve labelled ‘n-decay only’ represents the n/p ratio for the hypothetical case without build-up of nuclei. Note that the horizontal line labelled ‘actual’ includes the neutrons bound into the light nuclei.

chromodynamic, phase transition at $T \approx 100$ MeV. The weak interactions which couple neutrinos to the cosmic plasma and interconvert neutrons and protons into each other are very fast at this early stage of the cosmic evolution. Weak equilibrium between neutrons and protons is established via the reactions



and the ratio of their number densities is given by the equilibrium value,

$$\frac{n_n}{n_p} \equiv \frac{n}{p} = \exp \left[\frac{-\Delta m}{T} \right], \quad (3.6)$$

which depends only on the ratio between the difference in rest mass, $\Delta m \equiv m_n - m_p$, and on the cosmic temperature T (see the curve labelled ‘equilibrium’ in the right panel of Fig. 3.1). The epoch of weak equilibrium ends at $T \approx 1$ MeV, when the interaction rates drop below the expansion rate of the Universe and are thus not fast enough to maintain the equilibrium abundances. At this point, the neutron-to-proton ratio freezes out with its current value of $n/p \approx 1/6$, but continues to decrease further due to residual weak interactions, eventually dominated by neutron decay, as may be seen in the right panel of Fig. 3.1.

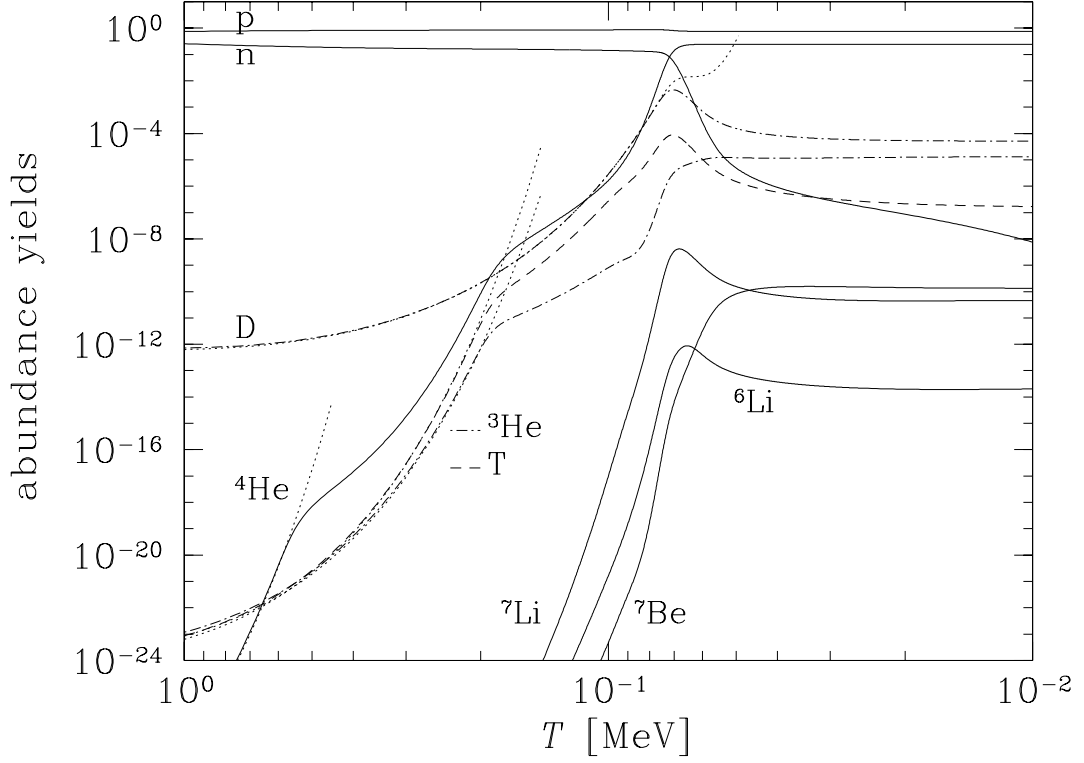


Figure 3.2: Light element abundances as predicted by a standard BBN calculation with $\eta = 3 \times 10^{-10}$. Shown are the mass fractions of n , p , and ${}^4\text{He}$, and the number densities relative to hydrogen (N_i/N_{H}) for the other elements. Also indicated are the NSE abundances for some of the light elements (dotted lines).

The nuclear reactions, which lead to the built-up of the light elements, are also very fast at early times and nuclear statistical equilibrium (NSE) between neutrons and protons and the light elements is established early on. The NSE mass fraction X_A for a nucleus with mass number A and binding energy B_A is given by

$$X_A = g_A \left[\zeta_3^{A-1} \pi^{\frac{1-A}{2}} 2^{\frac{3A-5}{2}} \right] A^{5/2} \left(\frac{T}{m_N} \right)^{\frac{3(A-1)}{2}} \eta^{A-1} X_p^Z X_n^{A-Z} \exp[B_A/T], \quad (3.7)$$

where X_n and X_p are the neutron and proton mass fractions respectively and $\zeta_3 = 1.20206$ is the Riemann zeta function of argument 3 (see e.g. Abramowitz & Stegun 1972). For a given temperature, the NSE mass fractions thus depend only on the baryon-to-photon ratio $\eta \equiv n_b/n_\gamma$, which parameterizes the baryon content of the Universe, and on the actual neutron and proton number densities. In Fig. 3.2 the NSE values for the light elements are indicated by dotted lines. Below a temperature of ≈ 1 MeV, the elements, one by one, according to their mass, drop out of NSE, mainly because the

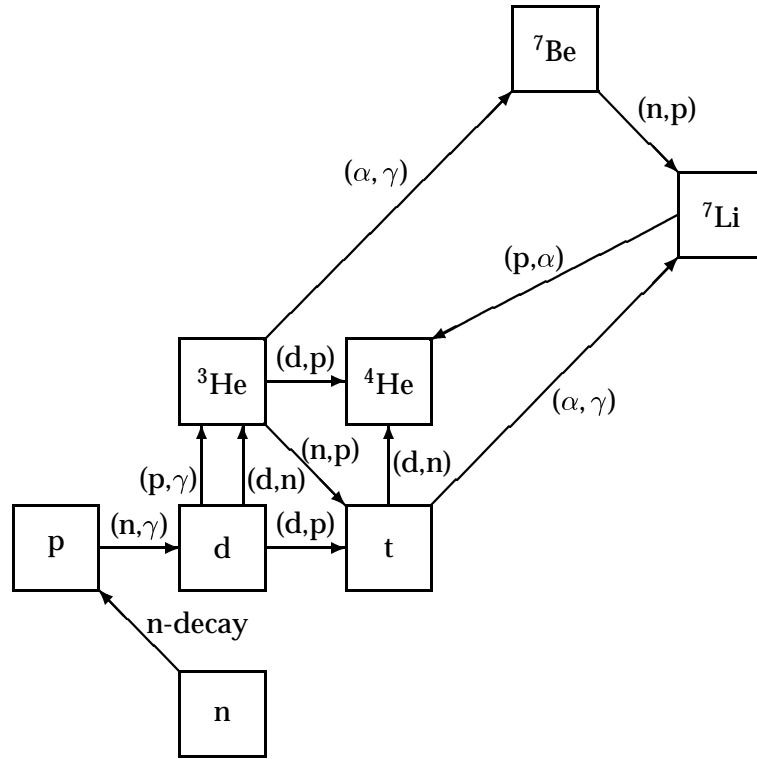


Figure 3.3: The BBN network. For reasons of clarity, only the twelve most important reactions interconverting the light elements are shown.

lighter elements, which form the heavier ones, are not abundant enough to establish the NSE values. The mass fractions of the heavier elements are thus forced to follow the ones of the lighter elements, from which they are synthesized. Only at temperature $T_{4\text{He}} \approx 80$ keV, the abundances of the lighter elements are high enough to produce ${}^4\text{He}$ of order unity. Virtually all free neutrons available at $T_{4\text{He}}$ are bound into ${}^4\text{He}$ nuclei and thus the primordial ${}^4\text{He}$ mass fraction Y_{p} may be estimated analytically,

$$Y_{\text{p}} \approx \frac{4n_n/2}{n_n + n_p} \Big|_{T_{4\text{He}}} = \frac{2(n/p)}{1 + (n/p)} \Big|_{T_{4\text{He}}} \approx 0.25. \quad (3.8)$$

Here I used that $n/p|_{T_{4\text{He}}}$ is approximately 1/7. From observations, we know that $Y_{\text{p}} \approx 0.24$, which tells us that this simple picture of BBN should not be far from the truth.

The amount of ${}^4\text{He}$ synthesized thus depends crucially on the neutron-to-proton ratio at $T_{4\text{He}}$. This number is in turn determined by the exact details of weak freeze out and by the time between weak freeze out and ${}^4\text{He}$ synthesis during which the change in the neutron-to-proton ratio is dominated by neutron decay. As was discussed above, the expansion time scale of the early Universe is governed by the number of effective relativistic degrees of freedom, g_* (see Eqs. 3.4 and 3.2). A higher value of g_* , and thus

a faster expansion, leads to a higher temperature for weak freeze out, which results in a higher freeze out value of the n/p ratio. Further, such a Universe cools down faster to $T_{4\text{He}}$, and thus less neutrons may decay. Both effects increase the amount of ${}^4\text{He}$ synthesized.

Elements heavier than ${}^4\text{He}$ are only synthesized in very small amounts, since the Coulomb barrier at the time of ${}^4\text{He}$ production is already high and no stable elements at mass 5 and 8 exist. Three body reactions, such as the triple alpha process, which bridges the gap in stellar nucleosynthesis, are not effective due to the low nuclear densities.

In order to calculate exactly the abundances of the light elements, a nuclear network describing the reactions between the light nuclei (see Fig. 3.3) has to be solved numerically on the background of the expanding Universe. The time evolution of the nucleonic densities is given by

$$\frac{\partial n_i}{\partial t} = \sum_{k,l} \langle \sigma v \rangle_{kl} n_k n_l - \sum_j \langle \sigma v \rangle_{ij} n_i n_j \quad (3.9)$$

where $\langle \sigma v \rangle_{kl}$ is the thermally averaged cross section for the respective reaction ($k + l \rightarrow i + j$) and it is understood that the sums run only over those reactions, which have the nucleus i either in the incoming or the outgoing channel.

The first detailed numerical solution of this problem was given by Wagoner, Fowler & Hoyle (1967), but the original idea of cosmological ${}^4\text{He}$ synthesis and early abundance calculations date back much earlier (Chandrasekhar & Henrich 1942, Gamow 1946, Alpher, Bethe & Gamow 1948, Hayashi 1950, Alpher, Follin Jr & Herrmann 1953, see Alpher & Herman 1988 for some interesting ‘‘Reflections on early work on ‘Big Bang’ Cosmology’’ by two of the pioneers in that field). BBN calculations used to be a game with three unknowns, g_* , the neutron half life and η . Today, the the neutron half-life and the particle content of the cosmos during the BBN era, thus the value of g_* , are reasonably well known, so there remains only one free parameter in Standard Big Bang Nucleosynthesis (SBBN), namely the neutron-to-proton ratio η . In Fig. 3.2, I show the results of a SBBN calculation for $\eta = 3 \times 10^{-10}$.

3.3 Observations

The calculated abundances have to be confronted with observations to test the theory of BBN, in particular to check for consistency of the SBBN model and to pin down the only SBBN parameter η and thus the baryonic density of the Universe. The use of BBN as a cosmological probe for new physics also requires knowledge about the true primordial abundances in order to derive meaningful constraints on the various parameters of non-standard models. The key problem is to infer the primordial abundances from observations made today, after some 10^{10} years of cosmic history and stellar processing of the elements, known as galacto-chemical evolution. The common strategy of all attempts is the observation of the least chemically evolved pristine environments to minimize the extrapolation to the primeval abundances. At the moment, the situation is somewhat unclear, since for all three elements for which firm observational data is available and

which may therefore be used as baryometers of the Universe, different groups claim different, even mutually excluding, values for the primordial abundances. The current observational evidence is summarized in Tab. 3.3 and will be discussed separately for each of the elements in the following paragraphs.

Helium-4. Nuclear fusion in stars increases the ${}^4\text{He}$ content, thus the observations concentrate on old, chemically unevolved dwarf galaxies. A large number of measurements exist for the ${}^4\text{He}$ as well as for the O and N abundances in low-metallicity² HII regions of these galaxies. An empirical relation between the oxygen and nitrogen abundances and the ${}^4\text{He}$ abundance in these systems has been found. Following Peimbert & Torres-Peimbert (1974), the primordial abundance of ${}^4\text{He}$ is inferred from an extrapolation of the observed trend to zero metallicity.

I quote the ‘low’ value for the primordial ${}^4\text{He}$ mass fraction Y_p (Ref. [1] in Tab. 3.3) obtained by Olive, Skillman & Steigman (1997). This so-called ‘old standard value’ stems from a compilation of a large number of observational data by different groups. References to the original data may be found in the cited study. More recently, Izotov & Thuan (1998b) argued for a significantly higher value (Ref. [2] in Tab. 3.3), using a different technique to analyse the observed spectral lines. This new approach, described in Izotov, Thuan & Lipovetsky (1997), uses the data of several ${}^4\text{He}$ emission lines to self-consistently determine the physical parameters of the HII regions, such as the electron density, whereas in the work by Olive et al. (1997) only one helium line and additional information from a sulphur II line was used. Both techniques have their weaknesses, as was pointed out by Olive et al. (1997) and Izotov & Thuan (1998a,b). Further, Izotov et al. (1997) stress the importance of underlying stellar absorption in some of the systems, in particular they reject the use of one specific component of the lowest-metallicity dwarf galaxy known (north-west component of I Zw 18) for which they found strong evidence for stellar absorption. A different path to the primordial ${}^4\text{He}$ mass fraction had been taken by Izotov & Thuan (1998a), who derived the ${}^4\text{He}$ mass fractions for the two most metal deficient galaxies, where stellar absorption is believed to be much weaker (south-east component of I Zw 18 and SBS 0335-052). The results are in good agreement with their extrapolated value.

Deuterium. Deuterium is the only of the light elements where one believes a primordial abundance is observed directly. Following the original suggestion by Adams (1976), deuterium lines were found in high redshift extragalactic HII clouds which lie on the line of sight to distant quasars (Quasar Absorption Systems, or QAS). These clouds supposedly underwent only minimal chemical evolution and should therefore reflect the primordial deuterium abundance. Unfortunately, the values found in different systems by different authors, or in identical systems by different authors, do not agree. Burles, Kirkman & Tytler (1999) argued that the system QSO 0014-813, in which the high value $\text{D}/\text{H} \approx 2 \times 10^{-4}$ was originally measured (Songaila, Cowie, Hogan

²In astrophysics, all elements beyond He in the periodic table are labelled metals, the metallicity of a system is just its content of elements with mass > 4 .

Table 3.1: Observationally inferred primordial light-element abundances. ‘Measured’ values and the errors are taken from the given papers in which references to the original observations may be found. The errors are systematic (1σ , unless stated otherwise) except for those with the superscript ‘stat’ (for statistical), and for the ones marked [*], where the errors given are a combination of systematic and statistic uncertainties, see text.

Abundance	Measurement	Adopted Range	Ref.
Y_p	$0.234 \pm 0.003^{\text{stat}} \pm 0.005$	0.223–0.245	[1]
	$0.244 \pm 0.002^{\text{stat}}$	0.240–0.248	[2]
$D/H \times 10^5$ (QSO)	$3.39 \pm 0.25^{\text{stat}}_{2\sigma}$	3.14–3.64	[3]
	20 ± 5	15–25	[4]
	4.4 ± 0.3	4.1–4.7	[5]
	< 6.7		[6]
	1.5		[7]
$D/H \times 10^5$ (ISM)	1.6 ± 0.2	> 1.4	[8]
$(D/H)_{\odot} \times 10^5$	2.6 ± 1.0		[9]
$(^3\text{He}/H)_{\odot} \times 10^5$	1.5 ± 0.3		[9]
$A(^7\text{Li})$	$2.09^{+0.19}_{-0.13}[*]$	1.96–2.28	[10]
$\equiv \log_{10}(^7\text{Li}/H) - 12$	$2.238 \pm 0.012 \pm 0.05^{\text{stat}}$	2.18–2.3	[11]
	$2.35 \pm 0.10[*]$	2.25–2.35	[12]
		2.35–2.75	[13]
$^6\text{Li}/^7\text{Li}$	≈ 0.05		[14]

[1] Olive et al. (1997), [2] Izotov & Thuan (1998b), [3] Burles & Tytler (1998b), [4] Webb et al. (1997b), [5] Levshakov, Kegel & Takahara (1998), [6] Kirkman et al. (1999), [7] Molaro, Bonifacio, Centurion & Vladilo (1999), [8] Dearborn, Steigman & Tosi (1996), [9] Geiss (1993), [10] Ryan, Norris & Beers (1999b), Ryan et al. (1999a), [11] Bonifacio & Molaro (1997), [12] Vauclair & Charbonnel (1998), [13] Pinsonneault, Walker, Steigman & Narayanan (1999), [14] Cayrel et al. (1999)

& Rugers 1994, Carswell, Weymann, Cooke & Webb 1994), should not be used to determine the primordial D/H value, since the features of the observed lines cannot be explained by deuterium alone and are therefore contaminated by Ly α lines redshifted to the position of the deuterium line. They conclude that only an upper limit for deuterium can be deduced from this system. However, the high value got some support by Webb et al. (1997b), who found a comparable high value at $z_{\text{abs}} = 0.7$ in the line of sight towards QSO 1718+4807 (Ref. [4] in Tab. 3.3). However, Tytler et al. (1999) showed that the fit to the data is not unique and one can fit a lower D/H for the same system, if a more sophisticated velocity distribution or a second component is assumed. Nevertheless, the range given by Tytler et al. (1999) does not exclude the high value. In two other systems, Q1937-1009 and Q1009+2656, Burles & Tytler (1998a,b) found a much lower value for D/H. In a prior investigation of the system Q1937-1009 Songaila, Wampler & Cowie (1997) reported a lower limit which is in conflict with Burles & Tytler

(1998a) due to a different way of determining the HI column density. In a series of papers, Levshakov, Kegel, and coworkers (Levshakov & Kegel 1997, Levshakov, Kegel & Mazets 1997, Levshakov, Kegel & Takahara 1999b) developed the mesoturbulent model, a new approach to model the velocity field in the absorbing clouds. Applying this model, they found a common value for D/H in the two systems showing low D/H and in the high system, QSO 1718+4807, (Levshakov et al. 1998; Ref. [5] in Tab. 3.3) using the same data sets utilized by Burles & Tytler (1998a,b) and Webb et al. (1997b). This common value is somewhat higher than the low value advertised by Tytler & Burles and considerably lower than the high value by Webb et al. (1997b), but agrees with the value reported by Songaila et al. (1997). A new upper limit, which excludes the high values, has recently been obtained by Kirkman et al. (1999) in the system QSO 0130-4021 (Ref. [6] in Tab. 3.3). Another very low determination of D/H in a further system, APM 08279+5255, has been reported by Molaro et al. (1999); Ref. [7] in Tab. 3.3. Taken at face value, it is incompatible with both the high and the low value. Levshakov, Agafonova & Kegel (1999a) reanalyzed the system and were able to model the Ly α profile using a considerably lower HI column density. This implies that the identification of the deuterium line in this system is highly model-dependent and thus cannot be confirmed or ruled out at this stage. Clearly, more high redshift quasar spectra are needed to reveal the true primordial deuterium abundance.

In addition to the QSO determinations, there is the canonical value from observations of deuterium in the solar system (Geiss 1993) which provides a lower limit on the primordial deuterium abundance. Based on the theory of galacto-chemical evolution for deuterium, an upper limit — usually about a factor of 2–3 higher (cf. Edmunds 1994) — may be inferred. The most recent analysis is that of Dearborn et al. (1996); Ref. [8] in Tab. 3.3.

Lithium-7. In a sample of old POP II stars, which span more than two orders of magnitude in metallicity, ${}^7\text{Li}$ is found to have a remarkably constant abundance. On grounds of lack of dispersion, this so-called Spite-plateau (Spite & Spite 1982) is usually interpreted as the primordial value for the ${}^7\text{Li}$ abundance. Due to the uncertainty in determining the effective temperatures of these stars, the error is dominated by systematic effects. Still larger systematic errors may be hidden by the limitations inherent in the modelling of stellar atmospheres (Kurucz 1995). We quote here the most recent determination of the plateau-value by Bonifacio & Molaro (1997); Ref. [11] in Tab. 3.3. Nevertheless, stellar models have been proposed which deplete ${}^7\text{Li}$ considerably (Pinsonneault, Deliyannis & Demarque 1992, Chaboyer & Demarque 1994). However, destruction of ${}^7\text{Li}$ is always accompanied by depletion of the much more fragile ${}^6\text{Li}$. Therefore the first tentative detections of ${}^6\text{Li}$ (Smith, Lambert & Nissen 1993, Hobbs & Thorburn 1994, 1997) and the more recent confirmation on a 95% confidence level (Cayrel et al. 1999) put tight constraints on Li depletion in these stars (Vangioni-Flam et al. 1999, Fields & Olive 1999). Current stellar models (Vauclair & Charbonnel 1995, 1998; Ref. [12] in Tab. 3.3; Pinsonneault et al. 1999; Ref. [13] in Tab. 3.3) predict only moderate depletion by rotational mixing, diffusion or stellar winds. The primordial value in these models is thus only slightly higher than the one observed at the surface of these stars. Ryan, Nor-

ris & Beers (1999b) and Ryan et al. (1999a) for the first time claim to have found evidence for a gradient of the abundances with metallicity. If this gradient turns out to be real, the primordial abundance of ${}^7\text{Li}$ should be lower than the currently advertised plateau-value (which would then, however, be a misleading term). Further, they argue that the presence of ${}^6\text{Li}$ in some plateau stars is a clear hint for non-primordial Li, produced by cosmic rays, which should be subtracted from the observed values. This effect should be taken into account independent of whether one believes in the abundance gradient or not. Ryan et al. (1999a,b) thus argue for a significantly lower value for the primordial ${}^7\text{Li}$ abundance than reported previously (Ref. [10] in Tab. 3.3).

Helium-3. Only determinations for the pre-solar ${}^3\text{He}$ abundance are available. The chemical evolution of ${}^3\text{He}$ is not yet well understood, thus an extrapolation back to the primordial abundances does not yield a reliable result. In the light of the much better understood limits derived on the basis of ${}^4\text{He}$, deuterium, and ${}^7\text{Li}$ observations, the ${}^3\text{He}$ data is usually not used to constrain η in SBBN. It is nevertheless useful to derive limits on non-standard BBN scenarios. It seems reasonable to assume that the ratio between ${}^3\text{He}$ and deuterium is an increasing function of time since deuterium is the most fragile of the light elements, so whenever ${}^3\text{He}$ is destroyed, deuterium will certainly be destroyed as well (Sigl, Jedamzik, Schramm & Berezhinsky 1995). Therefore

$$\left(\frac{{}^3\text{He}}{\text{D}}\right)_t \gtrsim \left(\frac{{}^3\text{He}}{\text{D}}\right)_{\text{pre-galactic}} \quad (3.10)$$

holds for any time t after after the end of pre-galactic nucleosynthesis. Pre-galactic nucleosynthesis includes not only BBN, but also potential re-processing of the abundances due to photodisintegration or nuclear disruption prior to the formation of the first stars. The most accurate determination of ${}^3\text{He}/\text{D}$ is thought to come from solar system observations. Geiss (1993) reanalyzed the existing data and inferred the pre-solar abundance ratios (Ref. [9] in Tab. 3.3). Using these, one finds

$$\left(\frac{{}^3\text{He}}{\text{D}}\right)_{\text{primordial}} \lesssim 1. \quad (3.11)$$

Lithium-6. Only traces of ${}^6\text{Li}$ are produced in the framework of SBBN, and until very recently the observational data was very sparse. For this reason, ${}^6\text{Li}$ was not considered to be a cosmological probe by itself, but was only used to constrain the allowed range of ${}^7\text{Li}$ depletion, as was discussed above. With the confirmation of ${}^6\text{Li}$ detections in old halo-stars, which lie on the ${}^7\text{Li}$ Spite-plateau, this has however changed (see section on ${}^7\text{Li}$ for references).

The very low binding energy of ${}^6\text{Li}$ makes its production in thermonuclear burning in stars unfavourable, thus it is believed to have its origin in some other mechanism. Spallative production of ${}^6\text{Li}$ by the action of cosmic rays on the interstellar medium has been recently studied by Vangioni-Flam et al. (1999) and Fields & Olive (1999). Both

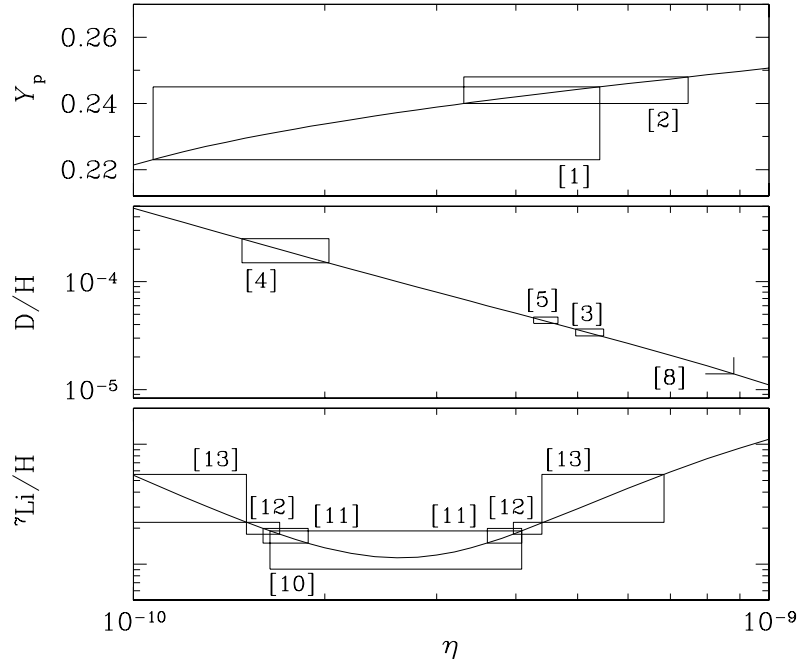


Figure 3.4: Abundances of the light elements for $10^{-9} < \eta < 10^{-10}$. Observationally inferred values are labeled as indicated in Tab. 3.3.

groups claim that they may accommodate for the relatively high ${}^6\text{Li}/{}^7\text{Li}$ ratio in low-metallicity POP II stars. In contrast, Ramaty, Scully, Lingenfelter & Kozlovsky (1999) argue that the comparable high ${}^6\text{Li}$ abundance in POP II stars may not be achieved by any existing cosmic ray scenario. Recently the ${}^6\text{Li}/{}^7\text{Li}$ ratio was also determined to be ≈ 0.05 in disk stars at much higher metallicity, but with a Spite-plateau value for the ${}^7\text{Li}$ abundance (Nissen, Lambert, Primas & Smith 1999). These authors claim that cosmic ray nucleosynthesis scenarios fail to explain both the ${}^6\text{Li}/{}^7\text{Li}$ ratio in POP II and disk stars. Therefore a pre-galactic source of ${}^6\text{Li}$ may even be desirable. Since only very few observations are available and since they are on the detection limit of current instruments, any definite conclusion regarding the origin of ${}^6\text{Li}$ seems premature at present. Furthermore, possible depletion of ${}^6\text{Li}$ in stars is currently not well understood. Despite these reservations, it is still tempting to use this new data to derive a tentative upper bound on the primordial ${}^6\text{Li}$ abundance of about ${}^6\text{Li}/\text{H} \sim 7 \times 10^{-12}$, which may be used to constrain some non-standard BBN scenarios, which greatly overproduce ${}^6\text{Li}$ relative to ${}^7\text{Li}$ (Jedamzik 1999). Given improvements in the observations, ${}^6\text{Li}$ may at some point even enter the circle of deuterium, ${}^4\text{He}$ and ${}^7\text{Li}$ as a baryometer of the Universe (Nollet, Lemoine & Schramm 1997).

3.4 Discussion

We are now in the position to compare the theoretical predictions with the abundances derived from observations. As I discussed in the previous section, the observational situation is somehow unclear. With the advent of the deuterium observations in the presumably unevolved high-redshift clouds, some saw BBN entering the ‘high-precision era’ (Schramm & Turner 1998). In light of a deuterium dichotomy, the discordant results for the ^4He mass fraction reported, and our limited understanding of the ^7Li data, this seems slightly premature. Nevertheless, there is little doubt that the basic picture of cosmological production in SBBN, or in some variant of SBBN, of all deuterium and the overwhelming part of the ^4He seen in the Universe is correct.

In Fig. 3.4, I have compiled the limits on the baryon-to-photon ratio η derived from the observationally inferred values for the primordial abundances of the light elements. The various limits are indicated with their respective labels defined in Tab. 3.3. The theoretical predictions shown were obtained with the same code used in the remainder of this work. Uncertainties in the nuclear reaction rates are not shown in the figure. In the case of ^4He and deuterium, the relevant cross sections are rather well known and the error in the predicted abundances is of the order of a few percent. The reactions leading to the built-up of ^7Li are not so well determined, corresponding to a 50 % uncertainty for the predicted ^7Li abundance. Taking this into account, two consistency regions may be identified in Fig. 3.4: (a) $\eta \approx 1.8 \times 10^{-10}$ (low ^4He , Ref. [1]; high deuterium Ref. [4]; and either of the ^7Li determinations) and (b) $\eta \approx 5 \times 10^{-10}$ (high ^4He , Ref. [2] and low deuterium; Refs. [3] or [5]; and one of the depletion models for ^7Li , Refs. [12] or [13]).

At the moment, the majority of people working in the field of BBN probably believe that the low deuterium value represents the primordial abundance. This is due to the high quality of the spectra presented for that case and due to the higher number of quasars found, which show this value. If it really turns out to be the correct value, then SBBN predicts a high value for Y_p , and $^7\text{Li}/\text{H}$ should be $\approx 3 \times 10^{-10}$. Such a high ^7Li abundance would however not only require considerable depletion but is also incompatible with the most recent low ^7Li determination by Ryan et al. (1999a).

The precise value of the BBN parameter η will thus remain an open question until we understand better the evolution of the abundances over the past 12 or so billion years of cosmic history.

The contribution of baryons to the critical density of the Universe Ω_b may be written in terms of η ,

$$\Omega_b \equiv \frac{\rho_b}{\rho_{\text{crit}}} = 3.68 \times 10^{-3} \left(\frac{T_\gamma}{2.73\text{K}} \right)^3 \left(\frac{\eta}{10^{-10}} \right) \left(\frac{H_0}{100 \text{ km s}^{-1} \text{ Mpc}^{-1}} \right)^{-2}, \quad (3.12)$$

where H_0 is the value of the Hubble parameter today and T_γ the temperature of the cosmic microwave background radiation measured today. The two values for η given above imply a baryon density of $\Omega_b h_{100}^2 \approx 6.6 \times 10^{-3}$ and $\Omega_b h_{100}^2 \approx 1.8 \times 10^{-2}$, respectively. Here the value of the Hubble parameter has been parameterized by $h_{100} \equiv H_0 / (100 \text{ km s}^{-1} \text{ Mpc}^{-1})$.

This range exceeds the luminous matter in the Universe by a factor of a few ($\Omega_{\text{lum}} \approx 0.002$, Persic & Salucci 1992), but also falls short of the dynamically inferred value for the total matter content of the Universe, Ω_0 , which is expected to be larger than $\Omega_0 \gtrsim 0.3$, based on galaxy-cluster mass determinations, measurements of peculiar velocities and gravitational lensing (Dekel 1994, Bahcall, Lubin & Dorman 1995, Dekel, Burstein & White 1997, Willick, Strauss, Dekel & Kolatt 1997, Falco, Kochanek & Muñoz 1998). BBN thus yields strong evidence for both baryonic *and* nonbaryonic dark matter in the Universe.

BBN is probably the earliest physical process in the history of the Universe which is understood in great quantitative detail. Due to its sensitivity to the physical conditions of the early Universe, BBN is a powerful tool to constrain cosmological and particle physics parameters. BBN considerations led, for example, to the prediction of three neutrino families before the measurement of the decay width of the weak gauge boson actually determined that number experimentally. All non-standard cosmological or particle physics scenarios which affect the n/p ratio at the BBN epoch should produce the same, observationally deduced amount of primordial ${}^4\text{He}$ as the standard scenario. Excellent and comprehensive reviews on such non-standard BBN scenarios exist and the interested reader is referred there (Malaney & Mathews 1993, Sarkar 1996). One example of a non-standard extension of both the particle physics and cosmological standard model is the putative presence of small-scale antimatter regions in the early Universe and the impact these regions might have on BBN (Rehm & Jedamzik 1998), which will be discussed in detail in this work.

Chapter 4

Annihilation of Antimatter Domains in the Early Universe

Notwithstanding the big success of Standard Big Bang Nucleosynthesis (SBBN) as one of the three cornerstones of modern cosmology, deviations from the cosmological and particle physics standard model which may influence BBN have been widely discussed in the literature. One of the key assumptions in SBBN is the homogeneity of the early Universe. Scenarios relaxing this assumption (Wagoner 1973, Gisler, Harrison & Rees 1974, Epstein & Petrosian 1975) have been studied only a few years after the first detailed SBBN calculations were available (Wagoner et al. 1967). Motivation for this early work came from the then reported spatial variation in the observed ${}^4\text{He}$ abundance. After it was realized that a first order quantumchromodynamic phase transition could produce the kind of inhomogeneities which would affect BBN, inhomogeneous BBN received a lot of attention. A number of approaches were driven by the desire to reconcile a Universe with critical mass in baryons with BBN (Applegate, Hogan & Scherrer 1987, Kurki-Suonio et al. 1988, Mathews, Alcock & Fuller 1990), which was however later shown to be excluded (Sato & Terasawa 1991, Jedamzik, Fuller & Mathews 1994). The deuterium dichotomy has more recently stimulated new interest in large-scale inhomogeneous models (Jedamzik & Fuller 1995, Webb et al. 1997a, Dolgov & Pagel 1999), which might explain the varying deuterium abundances observed in high-redshift Lyman limit systems. A common feature of most of these studies is the dissipation of pre-existing baryon-to-photon inhomogeneities in the early Universe at epochs below $T \lesssim 100$ MeV. These inhomogeneities should have been created at epochs where significant departures from local thermal or chemical equilibrium occurred, such as at the quantumchromodynamic (QCD) or electroweak (EW) phase transition, or during an inflationary epoch.

A number of models describing these symmetry breaking events predict not only positive-definite fluctuations in the baryon number, but also fluctuations of opposite sign (see e.g. Comelli, Pietroni & Riotto 1994, Giovannini & Shaposhnikov 1998a,b; for a review see Dolgov 1996). In this case, regions containing predominantly matter or predominantly antimatter may emerge. These kind of initial conditions have been

studied by Rehm & Jedamzik (1998), but have otherwise to my knowledge not received much prior attention apart from studies in the context of baryo-symmetric cosmologies (Steigman 1972, Combes et al. 1975, Steigman 1976, Aly 1978).

In this work, I consider a Universe consisting of matter and antimatter domains of various sizes, which are assumed to have initially identical baryon, or antibaryon, number densities and thus identical (anti-)baryon-to-photon ratios η . Such regions may exist in pressure equilibrium with each other at uniform cosmic temperature.

As long as the transport of baryon number over the boundaries from one region into the other is not effective, matter and antimatter is kept in separate regions. The photon and lepton densities are homogeneous and the temperature is the same throughout the Universe. Inhomogeneities in the total baryonic density, which is defined as the baryon plus antibaryon density at position r , $|n_b^{\text{tot}}(r)| = n_b(r) + n_{\bar{b}}(r)$, may arise only when baryon diffusion becomes effective and the baryons which travel over the boundary of the matter region annihilate in the antimatter region, and vice versa. Subsequently, the baryon and antibaryon densities close to the boundary decrease, leading to a decrease in the (anti-)baryon pressure in the annihilation region. This baryonic¹ underpressure is then compensated for by a slight adiabatic compression of the region and thus an increase of the radiation pressure, as to re-establish pressure equilibrium between the region and its environment. Heat diffusive processes tend to work towards re-establishing constant $|n_b^{\text{tot}}(r)|$ and, in particular, constant baryonic pressure.

In this chapter I will set the stage for the study of this scenario and shortly describe the relevant heat and baryon number transporting processes and their importance for the problem, mostly following Jedamzik & Fuller (1994). Further, I will discuss the annihilation process and the cross sections, before finally the secondary particles arising in the annihilations and their importance will be studied.

4.1 Setting the Stage

In the model under consideration, the Universe may be envisioned at early times as a distribution of matter with embedded domains of antimatter, as I schematically show in Fig. 4.1. Initially, the densities of matter $n_b(r|r > r_A)$ in the matter region and antimatter $n_{\bar{b}}(r|r < r_A)$ in the antimatter domains with radius r_A are assumed to be equal throughout the Universe. The average net baryon density is given by

$$\bar{n}^{\text{net}} \equiv \bar{n}_{\text{net}} \bar{n}_\gamma = n_b(r|r > r_A)(1 - f_{\bar{b}}) - n_{\bar{b}}(r|r < r_A)f_{\bar{b}}, \quad (4.1)$$

where the filling factor $f_{\bar{b}}$ is defined as the fraction of the volume of the Universe filled with antimatter. Here and in the following a bar over some quantity denotes the horizon average of that quantity. Since baryo-symmetric models will not leave baryon number after the completion of annihilation, models with an excess of baryon number will be considered, i.e. $f_{\bar{b}} < 0.5$. Further, I define the antimatter-to-matter ratio

$$R_A \equiv N_b/N_{\bar{b}} \quad (4.2)$$

¹For simplicity, I will use the terms ‘baryon’ or ‘baryonic’ in this section for both baryons and antibaryons.

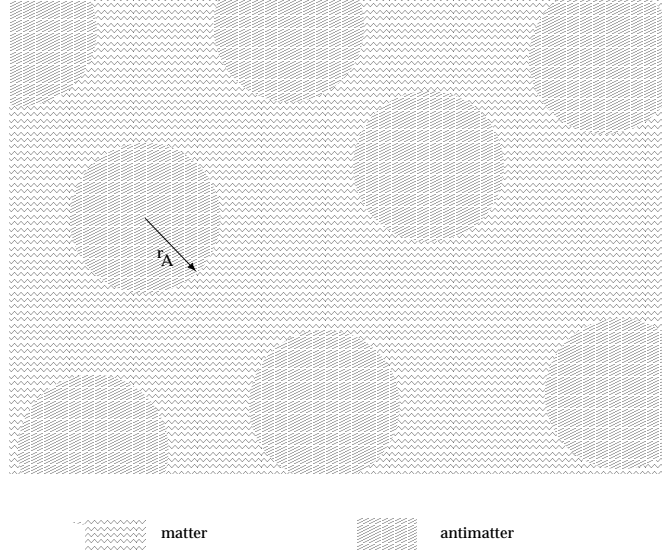


Figure 4.1: Sketch of the assumed initial conditions: Antimatter domains are embedded in a background of matter.

as the ratio of antibaryon number $N_{\bar{b}} = \int_V n_{\bar{b}}(r) d^3r$ to baryon number $N_b = \int_V n_b(r) d^3r$.

The densities $n_i(r, t)$ of the various baryonic particles, i.e. the nucleons and the light nuclei and their antiparticles, are affected by three mechanisms, namely diffusion and hydrodynamic processes, annihilation, and nuclear reactions (in this context, weak decays, such as $n \rightarrow p$, will be called nuclear reactions as well). Diffusion and hydrodynamic processes may only alter the spatial distribution of the various species, whereas annihilation and nuclear reactions may modify the abundances. Written in symbolic form, I get for the time evolution of the number density of nucleus i

$$\frac{\partial n_i}{\partial t} = \left. \frac{\partial n_i}{\partial t} \right|_{\text{diff/hydro}} + \left. \frac{\partial n_i}{\partial t} \right|_{\text{ann}} + \left. \frac{\partial n_i}{\partial t} \right|_{\text{nuc}}. \quad (4.3)$$

The last term, describing the nuclear reactions, was already discussed in Sec. 3.2; the other two terms describing diffusion and hydrodynamic processes and nuclear annihilation will be discussed in the two following sections.

It is convenient to express the length scales in the problem in comoving units. The length of, e.g., an antimatter region at some cosmic time t , or equivalently temperature T , may be related to the length it had at a fixed temperature T_0 , which I choose to be 100 GeV. The physical size $l(T)$ of that region in terms of the comoving size $l_{100} \equiv l(100 \text{ GeV})$ is thus given by

$$l(T) = l_{100} \left(\frac{R(T)}{R_{100}} \right), \quad (4.4)$$

where $R(T)$ is the cosmic scale factor at an epoch with temperature T , and I define $R_{100} \equiv R(100 \text{ GeV}) = 1$. The time evolution of the scale factor may be derived from the conservation of entropy, $S \propto g_{*s} T^3 R^3 = \text{const.}$ Thus the scale factor evolves as $R \propto g_{*s}^{-1/3} T^{-1}$, where g_{*s} is the number of relativistic degrees of freedom contributing to the entropy density of the Universe. The parameter g_{*s} is defined analogously to the number of relativistic degrees of freedom contributing to the energy density of the Universe g_* (cf. Eq. 3.3),

$$g_{*s} = \sum_{i=\text{bosons}} g_i \left(\frac{T_i}{T}\right)^3 + \frac{7}{8} \sum_{i=\text{fermions}} g_i \left(\frac{T_i}{T}\right)^3. \quad (4.5)$$

During most of the history of the Universe, $g_{*s} = \text{const.}$ and thus $R \propto T^{-1}$. This is not the case during particle annihilation (see Fig. 3.1) or phase transitions, such as the QCD phase transition at $T \approx 100 \text{ MeV}$ when g_{*s} drops from ≈ 50 to 19.5 due to the confinement of free quarks and gluons into hadrons. At the electroweak phase transition (EWPT, $T \approx 100 \text{ GeV}$), $g_{*s} \approx 100$. For definiteness, I will assume that $g_{*s}(100 \text{ GeV}) = 100$, which allows one, with the help of Eq. (4.4) and using the conservation of entropy, to calculate the physical length l as a function of the comoving length at 100 GeV, l_{100} . The comoving scale l_{100} thus corresponds, for example, to a physical length at a temperature of 1 MeV of $l(1 \text{ MeV}) = l_{100} \times 10^5 \sqrt[3]{\frac{10.75}{100}}$. Equivalently, the net baryon number density at an epoch with scale factor $R(T)$ may be calculated from the average net number density $\bar{n}_{100}^{\text{net}}(T)$ at $T = 100 \text{ GeV}$ by $n^{\text{net}}(T) = \bar{n}_{100}^{\text{net}}/R^3$.

4.2 Diffusive and Hydrodynamic Processes

4.2.1 Pressure Equilibrium

Fluctuations in the baryon-to-entropy ratio on scales below the horizon at a specific epoch of the evolution of the Universe will quickly come into pressure equilibrium. Their further evolution is determined by baryon diffusion and heat transport between the fluctuations, typically on much longer time scales. Prior to e^\pm annihilation, the photon mean free path is extremely short, thus photons are not effective heat transporters at that time. In the temperature range of interest for this work ($T \lesssim 10 \text{ MeV}$), neutrinos are not effective heat transporters either, as will be discussed below. Thus low baryon density regions may exist in pressure equilibrium with high density surroundings. Pressure equilibrium will be attained by adiabatic expansion of the high density surroundings and thus compression of the low density regions. This equilibrium state is stabilized by radiation pressure, leading to a slightly higher temperature inside the low density region, see Fig. 4.2. Any fluctuations which have come into pressure equilibrium will be termed as ‘isobaric’ fluctuations.

At late times, and for fluctuations where the photon mean free path after e^\pm annihilation becomes large compared to the spatial scale of the fluctuations, temperature gradients between the fluctuations cannot be maintained any more and the assumption

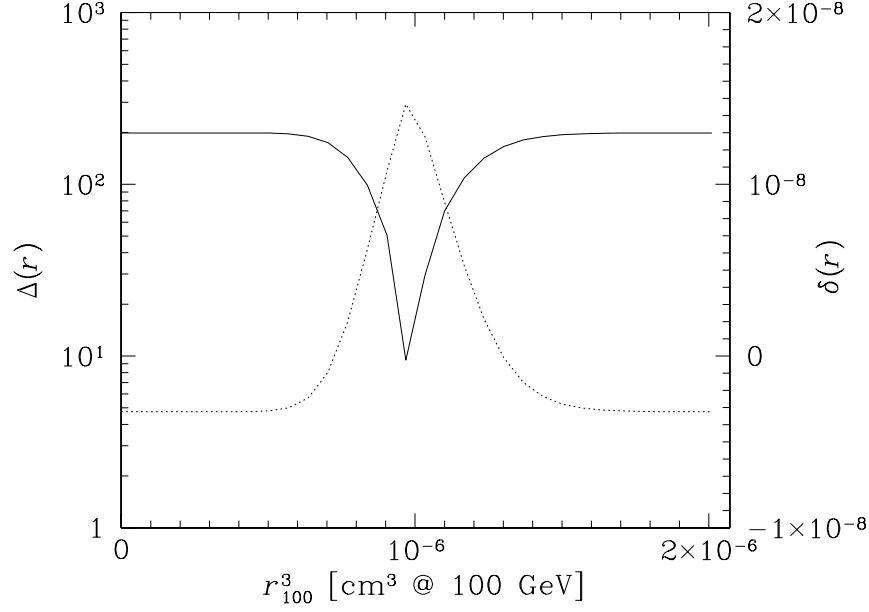


Figure 4.2: Snapshot of an isobaric density fluctuation. The full line represents the total baryonic overdensity $\Delta(r)$, the dotted line the deviation from the average cosmic temperature $\delta(r)$.

of pressure equilibrium breaks down. In this regime the density inhomogeneities are dissipated by hydrodynamic expansion of the cosmic fluid (see Sec. 4.2.3).

I define the number overdensity distribution $\Delta_i(r)$ for each baryonic species by the ratio of its actual number density at coordinate r to the average net baryon number density \bar{n}^{net}

$$\Delta_i(r) = \frac{n_i(r)}{\bar{n}^{\text{net}}}, \quad (4.6)$$

and the total baryonic overdensity distribution $\Delta(r)$ as

$$\Delta(r) = \sum_{\substack{i=\text{nucleons,} \\ \text{antinucleons}}} \Delta_i. \quad (4.7)$$

Initial (anti-)baryonic overdensities will be denoted by Δ_i^0 and the initial total baryon overdensity by Δ^0 .

The energy density in relativistic particles, $\varepsilon_{\text{rel}}(r)$ (see Eq. 3.2), at coordinate r is defined in terms of the horizon average of this quantity, $\bar{\varepsilon}_{\text{rel}}(r)$, by

$$\varepsilon_{\text{rel}}(r) = \bar{\varepsilon}_{\text{rel}}(1 + 4\delta(r)). \quad (4.8)$$

In this expression $4\delta(r)$ is then the deviation of the energy density from its average value at position r . In the limit where $\delta(r) \ll 1$ and during epochs where g_* may be

approximated as constant in time, I find that

$$\delta(r) \approx \frac{T(r) - \bar{T}}{\bar{T}}, \quad (4.9)$$

so that in this limit $\delta(r)$ is just the deviation from the cosmic average temperature at coordinate r .

If I assume that baryons contribute perfect gas pressure $P_b = n_b T$ and relativistic particles contribute pressure $P_{\text{rel}} = \frac{1}{3} \bar{\epsilon}_{\text{rel}}$, the demand for pressure equilibrium between the high and low density regions implies

$$\frac{1}{3} \bar{\epsilon}_{\text{rel}} (1 + 4\delta(r)) + \bar{n}^{\text{net}} \Delta(r) \bar{T} (1 + \delta(r)) \approx \frac{1}{3} \bar{\epsilon}_{\text{rel}} + |\bar{n}| \bar{T}, \quad (4.10)$$

with the average total baryonic number density $|\bar{n}| = \bar{n}_b + \bar{n}_{\bar{b}}$. In the limit where $\delta \ll 1$ and with the average baryonic pressure $\bar{P}_b = |\bar{n}_b| \bar{T}$ this expression reduces to

$$\delta(r) \approx -\frac{1}{4} \left(\frac{(\bar{n} - n^{\text{net}} \Delta(r)) \bar{T}}{\frac{1}{3} \bar{\epsilon}_{\text{rel}}} \right) \approx -\frac{1}{4} \left(\frac{\bar{P}_b - P_b(r)}{\bar{P}_{\text{rel}}} \right) \Delta(r). \quad (4.11)$$

4.2.2 Baryon Diffusion

The diffusion of baryons with diffusion constant D_b is described by

$$\frac{\partial n}{\partial t} = D_b \nabla^2 n, \quad (4.12)$$

which can be written in comoving radial coordinates and using the variables Δ_i instead of the densities n_i as follows (Jedamzik & Fuller 1994)

$$\frac{\partial \Delta_i(T, r_{100})}{\partial t} = \frac{1}{r_{100}^2} \frac{\partial}{\partial r_{100}} \left(\frac{D_i}{R^2} r_{100}^2 \frac{\partial}{\partial r_{100}} \Delta_i(T, r_{100}) \right). \quad (4.13)$$

The diffusion constant D_{ik} for baryons due to scattering on some species k with cross section σ_{ik} and number density n_k is approximately given by the product of thermal baryon velocity v_i and baryon mean free path l_i of the particle under consideration,

$$D_{ik} \approx \frac{1}{3} v_i l_i = \frac{1}{3} v_i \frac{1}{\sigma_{ik} n_k}. \quad (4.14)$$

Some relevant diffusion constants and their cosmological importance are compiled in Tab. 4.1. The effective baryon diffusion constant of nucleus i in the plasma due to scattering on the different species k is given by

$$\frac{1}{D_i} = \sum_k \frac{1}{D_{ik}}. \quad (4.15)$$

The diffusion length of a species is defined as the rms distance travelled during time t . Written in comoving coordinates, one finds (Applegate et al. 1987)

$$d_{100}(t) = \left[6 \int_0^t R^{-2} D(t') dt' \right]^{1/2}. \quad (4.16)$$

Table 4.1: Some relevant diffusion constants and their cosmological relevance.

Diffusion constant	cosmological importance	Ref.
$D_{ne} \approx (9.1 \times 10^2 \text{ m}^2 \text{ s}^{-1})(T/\text{MeV})^{1/2}(n_e/\text{MeV}^3)^{-1}$ $n_e = n_{e^+} + n_{e^-}$	$T > 100 \text{ keV}$	[1]
$D_{np} \approx 2.65 \times 10^{-3} \text{ m}^2 \text{ s}^{-1} R^3 (T/\text{MeV})^{1/2} (\Delta_p \Omega_b h^2)^{-1}$	$T < 100 \text{ keV}$	[2]
$D_{pe} \approx 1.1 \times 10^4 \log \delta \text{ m}^2 \text{ s}^{-1} (n_e/\text{MeV}^3)^{-1} (T/\text{MeV})^{3/2}$ $\delta = \lambda_{\text{Debye}}/\lambda_{\text{thermal}}$	$1 \text{ MeV} < T < 40 \text{ keV}$ and $T < 0.1 \text{ keV}$	[2]
$D_{e\gamma} \approx (0.2 \text{ m}^2 \text{ s}^{-1})(T/\text{MeV})^{-5/2}$	$30 \text{ keV} > T > 0.1 \text{ keV}$ (proton diffusion)	[2]
$D_{\gamma e} \approx (3.4 \times 10^{-2} \text{ m}^2 \text{ s}^{-1})(n_e/\text{MeV}^3)^{-1}$	$T < 30 \text{ keV}$ (heat diffusion)	[2]
References: [1] Applegate et al. (1987); [2] Banerjee & Chitre (1991)		
$\sigma_{ne} \approx 8.0 \times 10^{-35} \text{ m}^2$	$\sigma_{np} \approx 2.0 \times 10^{-27} \text{ m}^2$	
$\sigma_{pe} \approx 2.6 \times 10^{-29} (T/\text{MeV})^{-2} \log \delta \text{ m}^2$	$\sigma_{e\gamma} = \sigma_T \approx 6.7 \times 10^{-29} \text{ m}^2$	

Neutron Diffusion. At high temperatures, only neutrons can diffuse effectively, since the mean free path of the charged protons is very short due to their electromagnetic interactions with the ambient electrons and positrons. At early times, $T \gtrsim 100 \text{ keV}$, when e^\pm pairs are still abundant, neutron diffusion is limited by magnetic moment scattering on electrons and positrons as long as the local baryon-to-photon ratio is lower than $\eta \lesssim 3 \times 10^{-8}$, corresponding to an overdensity $\Delta \lesssim 100$ for a canonic value of $\bar{\eta} \approx 3 \times 10^{-10}$. At lower temperatures and/or higher densities, nuclear scattering on protons becomes important and is the dominant mechanism to limit the diffusion constant as may be seen in Fig. 4.3.

As long as the temperature is higher than $T \gtrsim 1 \text{ MeV}$, neutrons and protons are constantly interconverted by the fast weak interactions. Nucleons only diffuse during the time they spend as neutrons, and the weak reactions keep the neutron-to-proton ratio at its equilibrium value, $n_n/n_p = \exp[-\Delta m/T]$. Provided that the size of the antimatter region is smaller than the neutron diffusion length at these temperatures, baryon number can diffuse out of the matter into the antimatter regions, since the missing neutrons will be reproduced and can again diffuse. Between weak freeze out and ${}^4\text{He}$ synthesis at $T \approx 80 \text{ keV}$, $n \leftrightarrow p$ conversions are not effective any more, therefore only the fraction of matter made up of neutrons and antineutrons can diffuse and subsequently annihilate.

Proton and Light Nuclei Diffusion. Proton diffusion is limited by Coulomb scattering off electrons and positrons from the time of weak freeze out down to a temperature $T \approx 40 \text{ keV}$. Applegate et al. (1987) noted that for temperatures of the order or higher than the electron rest mass, the usual radiation drag formula is not valid. Protons move

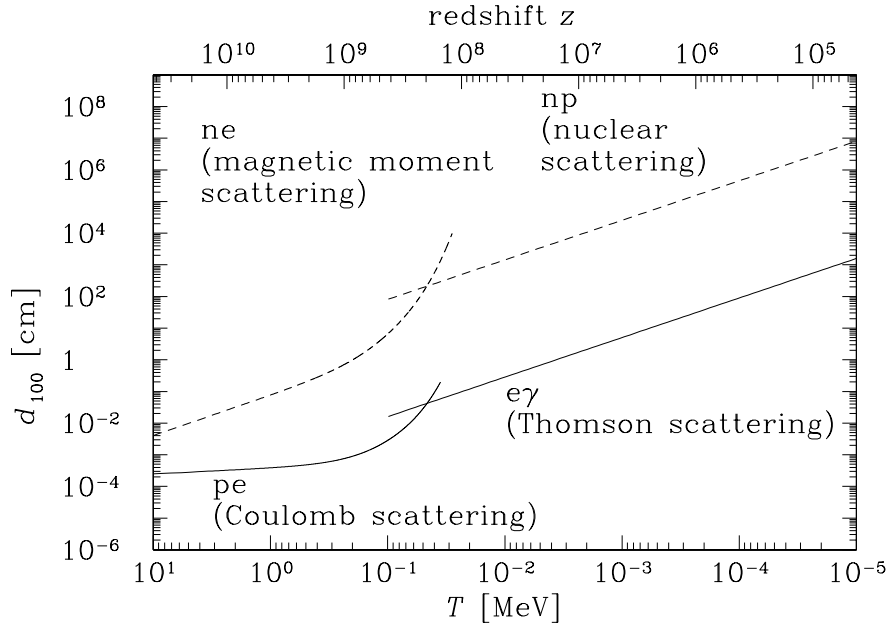


Figure 4.3: Diffusion lengths d_{100} of neutrons (dashed lines) and protons (full lines) in the early Universe, measured on the comoving scale fixed at $T = 100 \text{ GeV}$.

as independent particles through the plasma, since the Debye screening length is much shorter than a typical interparticle spacing. Therefore electric fields in the plasma over this distance cannot be maintained. The Coulomb cross section for the light nuclei is proportional to the square of the nuclear charge Z_i^2 and the thermal velocity to $\sqrt{1/A_i}$, where A_i is the mass number of the nucleus under consideration. This leads to a suppression factor of the diffusivity of nuclei relative to that for protons of $(1/Z_i^2 \sqrt{A_i})$.

When the pair density decreases at temperatures lower than $T \approx 40 \text{ keV}$, protons cease to diffuse as individual particles. Instead a proton-electron system diffuses together in order to establish electric charge neutrality and consequently the larger electron photon cross section dominates the proton diffusion constant. The proton and electron diffusion lengths are displayed in Fig. 4.3 for the temperature range of interest.

4.2.3 Heat Diffusion and Hydrodynamic Expansion

Heat transport between the high and low density regions, in particular regions with high and low baryonic pressure and concomitant high and low radiation pressure, can be accomplished by diffusing or free streaming neutrinos or photons. I will be interested in the evolution of inhomogeneities generated by annihilation below temperatures of $T \lesssim 20 \text{ MeV}$ on length scales corresponding to the baryon diffusion length

at the respective epoch and thus only phenomena relevant on these scales will be discussed below. For a more detailed description, the interested reader is again referred to Jedamzik & Fuller (1994).

Neutrino Heat Conduction. The neutrino mean free path is given by

$$l_{100}^\nu = \beta G_F^{-2} T^{-5} R^{-1} \approx 8 \times 10^{11} \text{ cm} \left(\frac{T}{\text{MeV}} \right)^{-5} (N_l + 3N_q)^{-1} R^{-1}, \quad (4.17)$$

where G_F is the Fermi constant, and N_l is the number of relativistic weakly interacting leptons at temperature T . These will include e^\pm , μ^\pm , τ^\pm , ν_e , $\bar{\nu}_e$, ν_μ , $\bar{\nu}_\mu$, ν_τ , and $\bar{\nu}_\tau$, whenever their masses satisfy $m_l < T$. Below a temperature of 20 MeV, $N_l = 8$ since only e^\pm and the neutrinos themselves are still relativistic. Similarly N_q is the number of relativistic free quark flavours at temperature T and may include u , d , s , c , b , and t . Thus $N_q = 0$ for $T \lesssim 100$ MeV due to the confinement of quarks into hadrons at the QCD phase transition. The dimensionless quantity β depends on the flavours and on the exact values of the weak couplings of the neutrinos. Jedamzik & Fuller (1994) have shown that neutrino heat conduction may play a role in the dissipation of large amplitude baryon inhomogeneities on small length scales. Of course, dissipation only occurs when the baryon inhomogeneities are accompanied by temperature inhomogeneities. The initial conditions envisioned here, constant $|n_b(r)|$ and thus constant temperature, are not of this type. Only when significant annihilation occurs, temperature inhomogeneities may develop. Only annihilations occurring close to or after weak freeze out are relevant for the light element abundances. At such late times the neutrino mean free path is much larger than the typical size of the fluctuations in $|n_b(r)|$.

Neutrino heat conduction is however most effective when the neutrino mean free path is of the order of the size of a density fluctuation. The scale for the density fluctuations is set by the neutron diffusion length

$$d_{100}^n \approx 10^4 \text{ cm} \left(\frac{T}{\text{MeV}} \right)^{-9/4} R^{-1}, \quad (4.18)$$

which is always considerably smaller than the neutrino diffusion length at low temperatures. Therefore, neutrinos are not efficient heat transporters at this evolutionary stage of the early Universe, since the weak interactions are not effective any more in transferring energy from the neutrinos to the plasma.

Photon Heat Conduction. After neutrino decoupling and before e^\pm annihilation heat transport is not effective because the mean free path of the heat transporting photons is very short. During the time of e^\pm annihilation, the photon mean free path

$$l_{100}^{\gamma e} \approx \frac{R^{-1}}{\sigma_T n_{e^\pm}} \quad (4.19)$$

increases enormously since it is inversely proportional to the pair number density, $n_{e^\pm} = n_{e^+} + n_{e^-}$. After the completion of e^\pm annihilation at temperature $T \approx 30$ keV, the

electron number density is given by the sum of the charged nuclei times their electric charge. The increased photon mean free path may then affect the dissipation of fluctuations in the baryon-to-entropy ratio (Alcock et al. 1990). Since the photons, in contrast to the neutrinos, remain tightly coupled to the cosmic fluid until the recombination epoch, temperature fluctuations and thus pressure equilibrium cannot be maintained any more.

One may distinguish two limits: dissipation due to diffusive photon heat transport and dissipation due to hydrodynamic expansion, according to whether the photon mean free path is smaller or larger than the region of the fluctuations. Borrowing terminology from radiation transport studies, Jedamzik & Fuller (1994) labeled these by the ‘optically thick’ and ‘optically thin’ limit, respectively. In the optically thick limit, heat transport is described by the diffusion equation for photons, which is identical to Eq. (4.13), but with $\Delta_i(r)$ replaced by the temperature fluctuations $\delta(r)$. The diffusion constant is now given approximately by

$$D_\gamma \approx \frac{g_t}{g_*} l_{\gamma e} \quad (4.20)$$

with g_t the statistical weight of the heat transporting particles ($g_t = 2$ for photons) and g_* is the statistical weight of the relativistic particles still coupled to the plasma ($g_* = g_t$ after e^\pm annihilation, since the neutrinos are decoupled).

The time to double the size of an entropy fluctuation by photon heat advection may be estimated to be

$$\tau_\gamma^{-1} \approx \frac{1}{5 \times 10^5 \text{ s}} \left(\frac{l_{100}}{\text{cm}} \right)^{-2} \left(\frac{T}{10 \text{ keV}} \right)^{-1} \left(\frac{2\Delta_p + 3\Delta_{4\text{He}}}{\Delta_p + 2\Delta_{4\text{He}}} \right). \quad (4.21)$$

In the opposite limit, when the photons are free streaming on the scale of the density fluctuations, the temperature will be the same in the high and low density regions and hydrodynamic expansion will effectively damp the density fluctuations. The high density regions will expand towards the low density regions and thereby transport material towards the annihilation region. The motion of the charged particles, protons and light elements, is impeded by the Thomson drag force, which acts on the electrons dragged along by the charged nuclei (Peebles 1971). Balance between pressure forces and the Thomson drag force yields a terminal velocity $v = dr_{100}/dt$,

$$v \approx \frac{3}{4\sigma_T \varepsilon_\gamma n_e} \frac{1}{R^2} \frac{dP}{dr_{100}}, \quad (4.22)$$

where dP/dr_{100} is the radial pressure gradient, r_{100} the radial coordinate as measured on the comoving scale, ε_γ the energy density in photons, and $n_e = n_{e^-} - n_{e^+}$ the net electron density. One finds for the pressure exerted by baryons and electrons below $T \approx 30 \text{ keV}$

$$P \approx \bar{T} n^{\text{net}} \left(\sum_i \Delta_i + \left(n_{\text{pair}}^*{}^2 + \left(\sum_i Z_i \Delta_i \right)^2 \right)^{\frac{1}{2}} - n_{\text{pair}}^* \right), \quad (4.23)$$

with the sum running over all nuclei i with nuclear charge Z_i . Note that expression 4.23 quickly reduces to the pressure exerted by an ideal gas when the reduced e^\pm pair density $n_{\text{pair}}^* = n_{\text{pair}}/n^{\text{net}}$ becomes negligible compared to $\sum_i Z_i \Delta_i$.

The time scale to double the size of a fluctuation by hydrodynamic expansion can be obtained from a characteristic fluid velocity and a characteristic fluctuation length l_{100}^{ann} . This time scale is roughly $\tau_h \approx l_{100}^{\text{ann}}/v$. After complete e^\pm -annihilation one finds

$$\tau_h^{-1} \approx \frac{1}{2.4 \times 10^5 \text{ s}} \left(\frac{l_{100}}{\text{cm}} \right)^{-2} \left(\frac{T}{10 \text{ keV}} \right)^{-1} \left(\frac{2\Delta_p + 3\Delta_{\text{He}}}{\Delta_p + 2\Delta_{\text{He}}} \right), \quad (4.24)$$

with the notation as before. This hydrodynamic expansion time scale is similar to the fluctuation dissipation time scale due to diffusive photon heat transport in Eq. (4.21). It is important to note that the damping time scales for diffusive photon heat flow and hydrodynamic expansion are independent of fluctuation amplitude.

4.3 Matter-Antimatter Annihilation

4.3.1 Annihilation Cross Sections

In order to investigate the influence of antimatter on BBN in more detail, the annihilation process and the relevant cross sections have to be discussed. The dominant process in nucleon-antinucleon interaction is direct annihilation into pions,

$$\left. \begin{array}{l} p + \bar{p} \\ p + \bar{n} \\ n + \bar{n} \\ n + \bar{p} \end{array} \right\} \rightarrow \pi^0, \pi^+, \pi^-, (\gamma, \nu\bar{\nu}). \quad (4.25)$$

Electromagnetic annihilation ($p + \bar{p} \rightarrow \gamma + \gamma$) is suppressed by a factor of $(m_e/m_p)^2 \approx 3 \times 10^{-7}$. Annihilation via the bound state of protonium is also possible, but the cross section is smaller by $(m_e/m_p)^{3/2} \approx 10^{-5}$ compared to direct annihilation.

The charged pions either decay with a lifetime of $\tau_{\pi^\pm} = 2.6 \times 10^{-8}$ s directly into leptons

$$\pi^+ \rightarrow \mu^+ + \nu_\mu \quad (4.26)$$

$$\left. \begin{array}{l} \mu^+ + \nu_\mu \\ \end{array} \right\} \rightarrow e^+ + \nu_e + \bar{\nu}_\mu \quad (4.27)$$

$$\pi^- \rightarrow \mu^- + \bar{\nu}_\mu$$

$$\left. \begin{array}{l} \mu^- + \bar{\nu}_\mu \\ \phantom{\mu^- + \bar{\nu}_\mu} \end{array} \right\} \rightarrow e^- + \bar{\nu}_e + \nu_\mu,$$

or may be transformed into π^0 via strong charge-exchange

$$\begin{array}{l} \pi^+ + n \rightarrow p + \pi^0 \\ \pi^- + p \rightarrow n + \pi^0 \end{array} \quad (4.28)$$

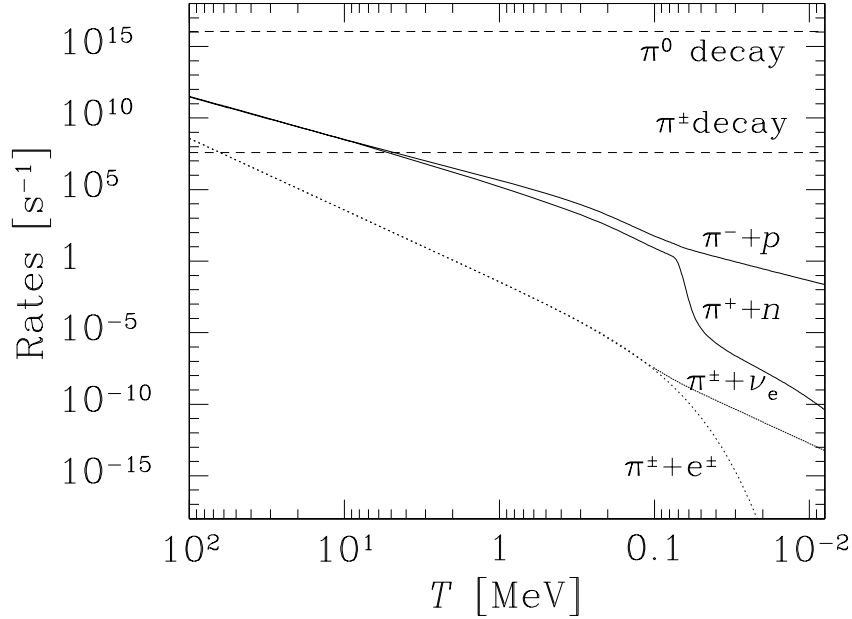
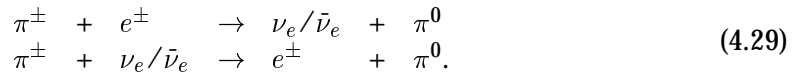


Figure 4.4: Interaction rates for pions with leptons (dotted lines) and nucleons (full lines). For comparison, the pion decay rates are also shown (dashed lines).

or weak interactions



The neutral pions subsequently decay into photons with $\tau_{\pi^0} = 8.4 \times 10^{-17}$ s. The rates for the three channels, pion decay and strong and weak interactions are shown in Fig. 4.4. Below a temperature of a few MeV, decay dominates the loss of charged pions. Nevertheless, some pions may charge-exchange on nucleons; possible consequences thereof will be discussed below. Weak interactions with the ambient leptons do not significantly contribute to the pion interaction rates in the temperature range of interest here ($T \lesssim 20$ MeV). Neutral pions never have a chance to interact with either leptons or nucleons, due to their short lifetime.

Annihilation of antinucleons on light nuclei produces a wealth of secondary particles,



In Tabs. 4.2 and 4.3 the branching ratios for the various annihilation channels and the probabilities to produce the respective secondary nuclei are given (Balestra et al. 1988).

Annihilations well before weak freeze out, $T_{\text{ann}} \gg 1$ MeV are not of much interest for this work, since they have no effect on the light element abundances. At temperatures below the recombination epoch, $T_{\text{ann}} \lesssim 10^{-7}$ MeV, the presence of significant

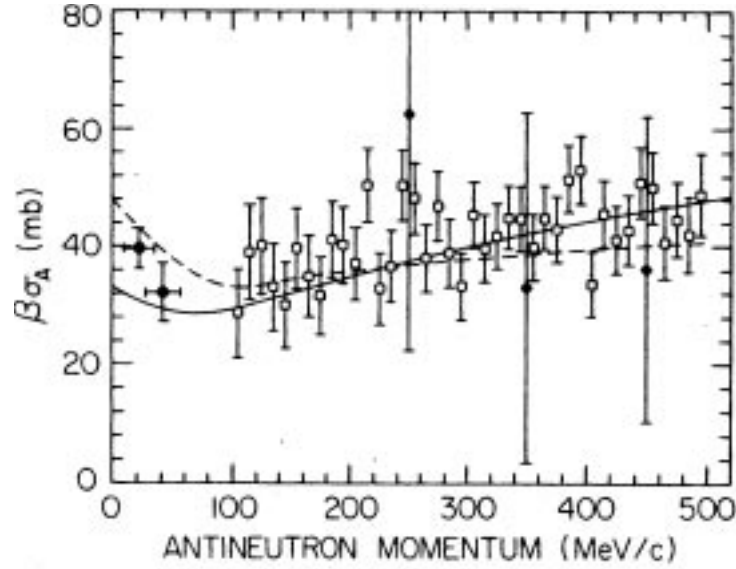


Figure 4.5: $\bar{n}p$ annihilation reaction rate $\beta\sigma_{\text{ann}}$ versus incident antineutron momentum measured in the lab frame. Solid circles are from Mutchler et al. (1988), open circles from Armstrong et al. (1987), and solid diamonds from Gunderson, Learned, Mapp & Reeder (1981). Plot taken from Mutchler et al. (1988).

amounts of antimatter is excluded by CMBR considerations (see Sec. 2). Therefore the annihilation cross sections for thermal nucleons with kinetic energies between a few MeV and about 10^{-7} MeV are needed. Experimental data are available only down to an incident momentum of about 30–40 MeV, corresponding to kinetic energies of about 1 MeV. Therefore, I have to use theoretical calculations for the cross sections in the relevant energy range. At such low energies, the Coulomb forces between charged particles become important, thus systems with Coulomb interactions like $\bar{p}p$ and $\bar{p}N$, and without, like $n\bar{n}$, $\bar{n}p$, and $\bar{n}N$, have to be treated separately. The low energy annihilation cross section σ_{ann} for neutral systems is given approximately by (Shapiro 1958, Car-

Table 4.2: Branching ratios and their respective errors for annihilation of the $\bar{p}^4\text{He}$ system as given in Balestra et al. (1988).

$\bar{p}^4\text{He}$	{	$^3\text{He} + \pi$	$r_b = .21 \pm .009$	* }	.22 \lesssim r_b \lesssim .29
		$\text{T} + \pi$	$r_b = .43 \pm .032$		
		$3n + \pi$	$.01 \lesssim r_b \lesssim .09$		
		$p + 2n + \pi$	$r_b \approx .24$		
		$\text{D} + n + \pi$	$.07 \lesssim r_b \lesssim .19$		
		$\text{D} + p + \pi$			
		$2p + n + \pi$	$r_b = .11 \pm .002$	*	

bonell, Protasov & Zenoni 1997)

$$\begin{aligned}\sigma_{\text{ann}} &\approx \frac{\pi}{q^2} (1 - \exp[2 \operatorname{Im}(a_s)q]) \\ &\approx 4\pi \left(\frac{\operatorname{Im}(-a_s)}{q} - 2 \operatorname{Im}^2(-a_s) \right).\end{aligned}\quad (4.31)$$

The first two terms in the expansion of the cross section in the centre of mass momentum q are entirely defined by the imaginary part of the scattering amplitude a_s . For very low energies, this cross section is inversely proportional to the centre of mass momentum q , so the product of cross section and relative velocity $\sigma\beta$ is approximately constant ($\beta = v/c$). Experimental values of $\sigma v = 40 \pm 3 \text{ mb } c$ and $32 \pm 5 \text{ mb } c$ (Mutchler et al. 1988, see Fig. 4.5) were obtained at centre of mass momenta of 22 MeV/ c and 43 MeV/ c , respectively. From these results, the complex part of the scattering length may be determined. In the calculations, I used a constant value of $\sigma v = 40 \text{ mb } c$ for annihilation in systems with at least one neutral particle.

In systems with Coulomb interactions, such as the $\bar{p}p$ or the \bar{p} -nucleus system, the $1/q$ behaviour of the low-energy annihilation cross section is drastically modified. Indeed, the charged particle low energy annihilation cross section is found to be proportional to $1/q^2$ and therefore the reaction rate $\sigma\beta$ is divergent at zero energy. Again, experimental data below about 1 MeV kinetic energy are not available. Carbonell & Protasov (1993) found an analytic expression for the S-wave contribution to σq^2 in antiproton-nucleus annihilation,

$$q^2 \sigma_{\text{ann}}^{\text{sc}}(\text{S-wave}) = \frac{8\pi^2}{1 - \exp(2\pi\eta)} \frac{\operatorname{Im}(-a_{\text{sc}}/B)}{|1 + iq\eta w(\eta)a_{\text{sc}}|^2}, \quad (4.32)$$

where a_{sc} is the scattering length in presence of Coulomb forces and $\eta = -1/qB$ the dimensionless Coulomb parameter. The Bohr radius $B = 1/(Z\mu)$ is given by the reduced mass μ of the system and the charge Z of the nucleus under consideration. $w(x) = c_0^2(x) - 2ixh(x)$ is an auxiliary function with $qBw(\eta) \rightarrow 2\pi$ when $q \rightarrow 0$, and c_0^2 and h are two functions used in Coulomb scattering theory,

$$c_0^2(x) = \frac{2\pi x}{\exp(2\pi x) - 1} \quad \text{and} \quad h(x) = \frac{1}{2} [\Psi(-ix) + \Psi(ix)] - \frac{1}{2} \ln(x^2)$$

with Ψ being the digamma function (see e.g. Abramowitz & Stegun 1972). It is necessary to take the P-wave contribution into account as well, for which a similar expression

Table 4.3: Probabilities to create the different nuclei in $\bar{p}^4\text{He}$ annihilations, derived from the branching ratios given in Tab. 4.2

P_n	P_p	P_D	P_T	$P_{^3\text{He}}$
0.51	0.28	0.13	0.43	0.21

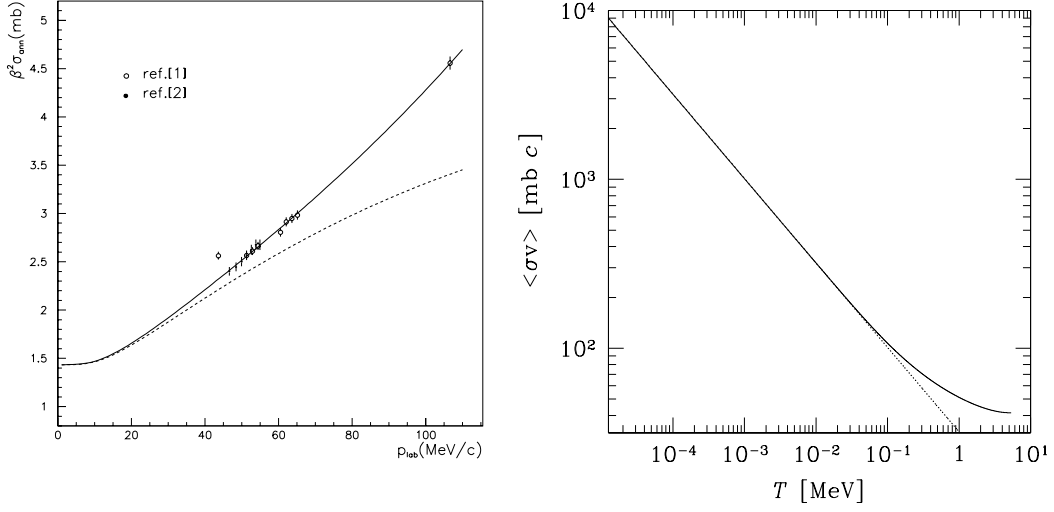


Figure 4.6: *Left panel:* $\bar{p}p$ annihilation cross section in mb times the square of the relative velocity in units of c . The full line represents the total annihilation cross section (S- and P-wave), whereas the dashed line shows the S-wave contribution only (taken from Carbonell et al. 1997). The data points given were obtained by [1] Bertin et al. (1996) and [2] Corradini (1997). *Right panel:* $\bar{p}p$ annihilation rate for a thermal plasma at temperature T . Below 10^{-1} MeV the total annihilation rate (full line) is well approximated by Eq. (4.34) (dotted line).

holds (Carbonell & Protasov 1996),

$$q^2 \sigma_{\text{ann}}^{\text{sc}}(\text{P-wave}) = 24\pi^2 \frac{1 + 1/\eta^2}{1 - \exp(2\pi\eta)} \frac{\text{Im}(-A_{\text{sc}}/B^3)}{|1 - qw(\eta)(1 + 1/\eta^2)\text{Im}A_{\text{sc}}/B^3|^2}. \quad (4.33)$$

Here, the scattering volume A_{sc} has to be used instead of the scattering length. These expressions describe the experimental data for $\bar{p}p$ annihilation up to a centre of mass energy of 100 MeV. In the left panel of Fig. 4.6, which was taken from Carbonell et al.

Table 4.4: Scattering lengths and volumes for charged particle annihilation systems.

system	$\text{Im}(a_{\text{sc}})$	$\text{Im}(A_{\text{sc}})$	Ref.
neutral	-0.83 ± 0.07 fm		[1]
$\bar{p}p$	-0.71 ± 0.05 fm	-0.71 ± 0.05 fm ³	[2]
$\bar{p}D$	-0.44 fm	-3.18 fm ³	[3]
$\bar{p}^3\text{He}$	-0.4 fm	-3.1 fm ³	[3]
$\bar{p}^4\text{He}$	-0.4 fm	-4.4 fm ³	[3]
References:	[1] Mutchler et al. (1988), [2] Carbonell et al. (1997), [3] C. Protasov, private communication		

(1997), $\beta^2\sigma$ is shown for momenta in the range from 0 to 100 MeV/ c together with some experimental results which are well reproduced. In the right panel I show σv , calculated from Eqs. (4.32) and (4.33). For thermal energies corresponding to temperatures below $\approx 10^{-1}$ MeV, which are relevant for $\bar{p}p$ annihilation in this work,

$$\sigma v \approx 32 \text{ mb}c \sqrt{\frac{\text{MeV}}{T}}, \quad (4.34)$$

as indicated by the dotted line in the right panel of Fig. 4.6. At energies above about 1 MeV, $\sigma_{\text{ann}}v_b$ for systems with and without Coulomb interaction is approximately equal.

In Tab. 4.4, I collect the (imaginary parts of the) relevant scattering lengths and volumes used in this work to calculate the reaction rates.

4.3.2 Secondaries in Nucleon-Nucleon Annihilations

It is of interest if annihilation-generated photons and pions, or their decay products, may alter the abundance yields, either through their effect on weak freeze out or by, for example, photodisintegration or charge exchange reactions. In a single annihilation event, about 5–6 pions with momenta ranging from tens to hundreds of MeV are produced. Due to charge conservation one gets exactly equal numbers of π^- and π^+ in $\bar{n}n$ and $\bar{p}p$ annihilations. In $\bar{n}p$ (or $\bar{p}n$) annihilations the π^+ (π^-) outnumber the π^- (π^+) by 1. The charged pions may perturb the n/p -ratio via the charge exchange reactions (Eq. 4.28) provided they do not decay before. Charged mesons quickly thermalize in the primordial plasma. Reno & Seckel (1988) calculated the thermalisation time scale for charged particles due to Coulomb scattering off a relativistic e^\pm gas

$$\tau_{\pi e^\pm}^{\text{stop}} \approx 10^{-14} \text{ s} \left(\frac{E_\pi}{1 \text{ GeV}} \right) \left(\frac{T}{1 \text{ MeV}} \right)^{-2}, \quad (4.35)$$

where E_π is the initial energy of the pions and $E_\pi = \mathcal{O}(100 \text{ MeV})$. Since this time is much shorter than a typical hadronic interaction time (see below), pions always thermalize before interacting. We therefore need the charge-exchange cross sections (see Eq. 4.28) for thermal pions interacting with thermal nucleons. The cross sections are approximately equal for both reactions (Reno & Seckel 1988),

$$\langle \sigma_{n\pi^+} \beta \rangle = 1.7 \text{ mb}, \quad (4.36)$$

$$\langle \sigma_{p\pi^-} \beta \rangle = 1.5 \text{ mb} \times \bar{C}(\gamma). \quad (4.37)$$

The $p\pi^-$ cross section is enhanced by a Coulomb factor $\bar{C}(\gamma)$, which is approximately given by

$$\bar{C}(\gamma) \approx 1 + \frac{\gamma}{\sqrt{\pi}} + \frac{\gamma^2}{6}, \quad (4.38)$$

with $\gamma = 2\pi\alpha\sqrt{\mu/2T}$. Inserting the reduced mass μ of the system and the fine structure constant α one gets $\gamma = 0.359/\sqrt{T/\text{MeV}}$. The expression for $\bar{C}(\gamma)$ is accurate to about

20 % for $\gamma < 2$, corresponding to $T > 0.03$ MeV. The maximal Coulomb enhancement is thus ≈ 3 .

A typical survival time $\tau_{\text{cex}}^{-1} = \langle \sigma v \rangle n_b$ for pions against charge exchange reactions is therefore

$$\tau_{\text{cex}} \approx 2 \times 10^{-6} \text{ s} \left(\frac{\eta_{\text{local}}}{4 \times 10^{-10}} \right)^{-1} \left(\frac{T}{\text{MeV}} \right)^{-3}. \quad (4.39)$$

This time should be compared to the lifetime of charged pions, $\tau_{\pi^\pm} \approx 2.6 \times 10^{-8}$ s, yielding

$$\frac{\tau_{\text{cex}}}{\tau_{\pi^\pm}} \approx 0.01 \left(\frac{\eta_{\text{local}}}{4 \times 10^{-10}} \right)^{-1} \left(\frac{T}{\text{MeV}} \right)^{-3}. \quad (4.40)$$

At temperatures $T \approx 1$ MeV, pions will only have a significant effect on the n/p ratio if the local baryon-to-photon ratio η_{local} is much larger than the net baryon-to-photon ratio ($\approx 4 \times 10^{-10}$). Due to their electromagnetic interactions with the abundant electrons and positrons, pions may only travel through the plasma via diffusion. The diffusion constant is of the same order as for the protons, therefore prior to pair annihilation charged pions are confined to the region of their creation, i.e. the annihilation region. Inside the annihilation region the baryonic densities, and thus the local baryon-to-photon ratio, are considerably lower than the average value $\bar{\eta}$, see Sec. 5.2. For this reason, I do not expect the pions to have a significant effect on the light element abundances. Nevertheless, pion production and pion induced charge exchange reactions are included in the numerical treatment. Eq. (4.40) also shows that charge exchange reactions at much lower temperatures will have negligible effect.

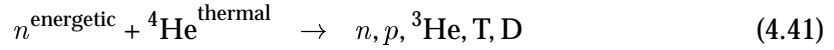
The leptonic secondaries μ^\pm , e^\pm and ν do not modify the details of weak freeze out, unless the number of annihilations per photon is extremely large. As long as this number is not approaching unity, annihilation generated ν_e 's have negligible effect on the n/p -ratio, since their number density is orders of magnitude smaller than the thermal ν_e 's, which govern the weak equilibrium. The same holds for electrons and positrons produced in μ -decay which are quickly thermalized by electromagnetic interactions.

Annihilation-generated γ -rays cascade on the background photons (and on pairs before e^\pm annihilation) via pair production and inverse Compton scattering on a time scale rapid compared to the time scale for photodisintegration of nuclei (Lindley 1980, Ellis et al. 1992, Protheroe, Stanev & Berezhinsky 1995). After e^\pm annihilation, the cascade only terminates when individual photons do not have enough energy to further pair-produce on background photons. For temperatures $T \gtrsim 5$ keV, the energy of γ -rays below the threshold for e^\pm -production does not suffice for the photodisintegration of nuclei. For annihilations occurring below 5 keV the situation changes, as will be discussed in the next section.

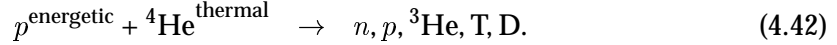
4.3.3 Secondaries in Nucleon-Nucleus Annihilations

Annihilations occurring after the onset of nucleosynthesis, $T \lesssim 100$ keV, will proceed not only via nucleon-antinucleon interactions, but also via annihilation on the now synthe-

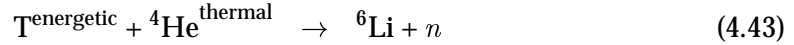
sized nuclei and antinuclei. In these processes, the element abundances may be substantially modified, compared to the results of the usual SBBN scenario. Since all antinuclei will eventually be annihilated and their relative abundances are thus not of interest, I will concentrate on the effects of annihilations on nuclei. Annihilation of a \bar{p} on a ${}^4\text{He}$ nucleus results in the production of a variety of secondary particles, among them electromagnetically interacting particles such as e^\pm and photons, energetic nucleons and deuterium, tritium, and ${}^3\text{He}$ nuclei with the relative probabilities given in Tab. 4.2. The energetic nuclei may alter the abundances of the light elements in two ways, if they are fast enough to escape from the annihilation region before being annihilated themselves. Firstly, they simply add to the respective abundances. This effect may be important for the deuterium, tritium, and ${}^3\text{He}$ nuclei, but is negligible for protons due to their high initial abundance. The neutrons decay anyway. The reduction of the ${}^4\text{He}$ abundance by a factor of about $(\sigma_{\bar{p}{}^4\text{He}}/\sigma_{\bar{p}p})(n_{{}^4\text{He}}/n_p)n_{\bar{p}}$ is only significant for large antimatter fractions. The second mechanism is that the energetic nuclei and nucleons created in the annihilation will be able to cause a second era of nucleosynthesis. In contrast to the BBN era, where nuclear reactions occur between nuclei in thermal equilibrium with each other, I now have to deal with a scenario where high energy particles are injected into a thermal bath of nucleons at much lower energy. The secondary neutrons and protons can spallate ${}^4\text{He}$ nuclei via



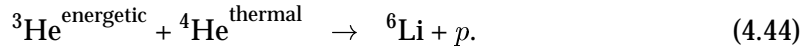
and



But, as I will discuss below, this is only a very small effect. Energetic tritium and ${}^3\text{He}$ will however turn out to have a very strong effect on the ${}^6\text{Li}$ abundance via the reactions



and



These reactions are possible until the kinetic energy of the particles n , p , tritium and ${}^3\text{He}$ drops below the threshold of about 20 MeV for ${}^4\text{He}$ spallation or about 4 MeV for ${}^6\text{Li}$ creation respectively. Energy loss proceeds via elastic nuclear scatterings in the case of n or plasmon excitations and Coulomb scattering on the ambient electrons in case of the charged particles.

Thermalisation of Energetic Charged Nuclei and Neutrons

All the secondary nuclei are mainly produced in the annihilation region. If they stayed there, they would inevitably be annihilated by the still abundant \bar{p} 's. On average, these particles gain a few tens of MeV kinetic energy in the annihilation (Balestra et al. 1988).

The distance covered until the kinetic energy of particles has decreased to the thermal energy of the plasma defines the stopping length

$$l^{\text{stop}} = \int_0^{l^{\text{stop}}} dx = \int_{E_0}^{E_{\text{thermal}}} \frac{dx}{dE} dE. \quad (4.45)$$

Provided l^{stop} is larger than the size of the annihilation region l^{ann} (Eq. 5.12), the particles survive and add either to the primary abundances synthesized during the BBN epoch or might initiate nuclear reactions if their kinetic energy is still large enough. Let us first calculate the stopping length for charged particles. The dominant energy loss mechanisms for charged particles in a plasma with kinetic energy below 1 GeV are plasmon excitations and Coulomb scatterings. The energy loss per distance (see e.g. Jackson 1975, Dimopoulos, Esmailzadeh, Hall & Starkmann 1988) is

$$\frac{dE}{dx} = \frac{Z^2 \alpha}{v^2} \omega_p^2 \ln \left(\frac{\Lambda v}{\omega_p b_{\text{min}}} \right) \quad (4.46)$$

where Z is the electric charge of the particle, $\omega_p^2 = 4\pi n_e \alpha / m_e$ the plasma frequency, α the fine structure constant, $\Lambda = \mathcal{O}(1)$ a numerical constant and

$$b_{\text{min}} = \max \left(\frac{1}{\gamma m v}, \frac{\alpha}{\gamma m v^2} \right).$$

The Lorentz factor $\gamma = 1$, since the kinetic energy E_0 of the nucleons is well below their rest mass m_N , therefore $E = m_N v^2 / 2$ and Eq. (4.45) reads

$$l^{\text{stop}} = \int_{E_0}^{E_{\text{thermal}}} \frac{2E}{m_N Z^2 \alpha} \omega_p^{-2} \ln^{-1} \left(\frac{\Lambda v}{\omega_p b_{\text{min}}} \right) dE. \quad (4.47)$$

If I neglect the energy dependence in the logarithm and the decrease in the electron density during the time needed to thermalize the energetic nuclei, the integration is straightforward and yields

$$l^{\text{stop}} = \frac{1}{3} \frac{(E_0^2 - E_{\text{thermal}}^2)}{m_N Z^2 \alpha} \omega_p^{-2} \ln^{-1} \left(\frac{\Lambda v}{\omega_p b_{\text{min}}} \right). \quad (4.48)$$

I have added an additional factor of 1/3 to account for all three dimensions, since the secondary particles emerge from the annihilation isotropically. It is convenient to express the stopping length in comoving units $L_{100}^{\text{stop}} = l^{\text{stop}} / R$. As was discussed in the previous section, the relevant temperature range for this process is $T < 1$ keV. Thus the thermal energy of the ambient nucleons is much smaller than the kinetic energy of the nucleons produced in the annihilations and may be neglected in Eq. (4.48). Parameterizing $n_e \approx \eta_{\text{local}} n_\gamma = (\eta_{\text{local}} / \eta) (2 / \pi^2) \eta T^3$, I get

$$L_{\text{stop},100} \approx 10^3 \text{ cm} \left(\frac{10^{-3} \text{ MeV}}{T} \right)^2 \left(\frac{E_0}{50 \text{ MeV}} \right)^2 \left(\frac{4 \times 10^{-10}}{\eta_{\text{local}}} \right) Z^{-2} \times \quad (4.49)$$

$$\begin{aligned} & \times \ln \left(4.53 \times 10^9 \left(\frac{E_0}{50 \text{ MeV}} \right) \left(\frac{T}{10^{-3} \text{ MeV}} \right)^{-3/2} \right)^{-1} \\ & \approx 55 \text{ cm} \left(\frac{10^{-3} \text{ MeV}}{T} \right)^2 \left(\frac{E_0}{50 \text{ MeV}} \right)^2 \left(\frac{4 \times 10^{-10}}{\eta_{\text{local}}} \right) Z^{-2}. \end{aligned}$$

The stopping length for charged particles can thus be significantly larger than the radius of the annihilation region $l_{100}^{\text{ann}} \approx 0.1 \text{ cm}$, corresponding to annihilation at a temperature of $T \approx 10^{-3} \text{ MeV}$ (see Eq. 5.12). Therefore a substantial amount of the charged secondaries may escape from the annihilation region.

In an analogous manner I may calculate the stopping time

$$\tau_{\text{stop}} = \int_0^{E_{\text{thermal}}} \frac{1}{v(x)} \frac{dx}{dE} dE \quad (4.50)$$

needed to slow down a particle to the thermal energy of the plasma. Evaluation of the integral yields for charged particles

$$\tau_{\text{stop}}^p \approx 3.25 \text{ s} \left(\frac{10^{-3} \text{ MeV}}{T} \right)^3 \left(\frac{E_0^{3/2} - E_{\text{thermal}}^{3/2}}{(50 \text{ MeV})^{3/2}} \right) \left(\frac{4 \times 10^{-10}}{\eta_{\text{local}}} \right) Z^{-2}. \quad (4.51)$$

Neutrons lose their energy through nuclear scatterings. In contrast to the charged particle interactions discussed above, the deflection angle in a nuclear scattering event may be large, so the stopping length calculated following Eq. (4.45) is not the distance which the neutrons moved away from the annihilation region. Rather, the distance covered by the neutrons is described by a random walk. The stopping time is nevertheless described by Eq. (4.50), since the energy loss does not depend on the direction of the motion. The energy loss per distance for neutrons may be estimated via

$$\frac{dE}{dx} = (-\ln f) E \sigma_{np} n_p, \quad (4.52)$$

where f is the fractional energy loss in each scattering event. If I assume a simple power law for the cross section $\sigma_{np} \approx 10^3 \text{ mb} (E/10 \text{ MeV})^{1.15}$ (cf. Fig. 1 in Meyer 1972) and an energy loss of 80 % in each scattering event, integration of Eq. (4.50) using Eq. (4.52) gives

$$\tau_{\text{stop}}^n = 1.56 \times 10^2 \text{ s} \left(\frac{10^{-3} \text{ MeV}}{T} \right)^3 \left(\frac{4 \times 10^{-10}}{\eta_{\text{local}}} \right) \left(\frac{E_0^{0.65} - E_{\text{thr}}^{0.65}}{(10 \text{ MeV})^{0.65}} \right). \quad (4.53)$$

^4He Spallation by Energetic Neutrons and Protons

Every $\bar{p}^4\text{He}$ annihilation produces about 0.3 energetic protons and 0.5 energetic neutrons. These particles may destroy additional ^4He nuclei until their kinetic energy drops below the threshold for ^4He spallation at 23 MeV. The time scale for spallation is

$$\tau_{\text{sp}} = \frac{1}{\langle \sigma_{\text{sp}} v \rangle n_{^4\text{He}}}. \quad (4.54)$$

The cross section for $p+{}^4\text{He} \rightarrow \text{T}, {}^3\text{He}$ is $\sigma_{\text{T},3} \approx 100 \text{ mb}$ in the energy range from 200 MeV down to threshold (Meyer 1972). At energies under consideration, the Coulomb barrier is always negligible. Since the ${}^4\text{He}$ nucleus is its own mirror nucleus, each $p+{}^4\text{He}$ reaction can be related to a mirror reaction $n+{}^4\text{He}$ by simply reversing the roles of the p and π^+ and of the n and π^- among the final products. Hence the cross sections for $n+{}^4\text{He}$ and $p+{}^4\text{He}$ reactions are approximately equal due to the charge symmetry of the strong interaction. The ${}^4\text{He}$ density can be expressed via the primordial ${}^4\text{He}$ mass fraction Y_p ,

$$n_{{}^4\text{He}} \approx (Y_p/4)\eta_{\text{local}}n_\gamma = (Y_p/4)(\eta_{\text{local}}/4 \times 10^{-10})(2/\pi^2)4 \times 10^{-10}T^3. \quad (4.55)$$

The spallation time for $n+{}^4\text{He}$ and $p+{}^4\text{He}$

$$\tau_{\text{sp}} \approx 1.5 \times 10^3 \text{ s} \left(\frac{100 \text{ mb}}{\sigma_{\text{T},3}} \right) \sqrt{\frac{50 \text{ MeV}}{E_0}} \left(\frac{0.25}{Y_p} \right) \left(\frac{10^{-3} \text{ MeV}}{T} \right)^3 \quad (4.56)$$

may now be compared to the stopping time for protons,

$$\frac{\tau_{\text{sp}}}{\tau_{\text{stop}}^p} = 650 \left(\frac{E_0}{50 \text{ MeV}} \right)^{-2} \left(\frac{0.25}{Y_p} \right). \quad (4.57)$$

τ_{stop}^p has been calculated following Eq. (4.51), but with the threshold energy as lower limit of the integration. For a typical kinetic energy $E_p \approx 50 \text{ MeV}$ only about 1.5×10^{-3} off all energetic protons may spallate a ${}^4\text{He}$ nucleus. Thus the amount of tertiary tritium and ${}^3\text{He}$ from $p+{}^4\text{He}$ spallation can safely be neglected. The stopping time for neutrons (Eq. 4.53) is also smaller than the spallation time,

$$\frac{\tau_{\text{sp}}}{\tau_{\text{stop}}^n} \approx 3.5 \left(\frac{50 \text{ MeV}}{E_0} \right)^{1.15} \left(\frac{0.25}{Y_p} \right) \left(\frac{\eta_{\text{local}}}{4 \times 10^{-10}} \right), \quad (4.58)$$

thus about 30% of the energetic neutrons will produce additional tritium or ${}^3\text{He}$. The probability to get a neutron in $\bar{p}+{}^4\text{He}$ annihilation is about 50 %, so I get tertiary tritium or ${}^3\text{He}$ from a tenth of the destroyed ${}^4\text{He}$ nuclei. This is not significant compared to the secondary tritium and ${}^3\text{He}$ nuclei produced in $\bar{p}+{}^4\text{He}$ annihilations with a probability of about 60 % and will therefore be neglected in the numerical treatment.

Production of ${}^6\text{Li}$ by Energetic Tritium and ${}^3\text{He}$ Nuclei

Energetic secondary tritium or ${}^3\text{He}$ nuclei with kinetic energy E_3 may produce ${}^6\text{Li}$ via the reactions Eq. (4.43) and Eq. (4.44). The differential probability for either of these reactions is given by

$$dP_{{}^6\text{Li}} = n_{{}^4\text{He}}\sigma_{{}^6\text{Li}}(E_3)dE \left(\frac{dx}{dE} \right)_{\text{Coulomb}}. \quad (4.59)$$

In an annihilation event, tritium and ${}^3\text{He}$ are not produced with a unique energy, but have an energy distribution. To take this into account, I have to weight the differential probability with the energy distribution function $f(E_3)$ before integrating over all

energies above the threshold E_{thr} to get the total probability

$$\langle P_{6\text{Li}} \rangle = \sum_{\text{T}, ^3\text{He}} \int_0^\infty dE_3 f(E_3) \int_{E_{\text{thr}}}^{E_3} dE n_{4\text{He}} \sigma_{6\text{Li}}(E) \left(\frac{dx}{dE} \right)_{\text{Coulomb}}. \quad (4.60)$$

Since the energy distribution of secondary nuclei produced in $\bar{p}^4\text{He}$ is only available as binned data (Balestra et al. 1988), the first integral is replaced by a sum. Balestra et al. (1988) show only 86 events with tritium identified in the final state compared to 297 events with ^3He . The high energy tail in the tritium distribution given is completely absent. But the particles in the high energy tail are responsible for ^6Li production. Since the overall features of the two distributions are very similar, I used the ^3He distribution, where the high energy tail is present, for both nuclei. The energy loss due to Coulomb and plasma interactions is calculated following Eq. (4.46). Using a value of $\sigma_{6\text{Li}}(E_3) \approx 35 \text{ mb}$ and the threshold energies $E_{\text{thr}} = 4.03 \text{ MeV}$ ($^3\text{He} + ^4\text{He} \rightarrow ^6\text{Li}$) and $E_{\text{thr}} = 4.80 \text{ MeV}$ ($\text{T} + ^4\text{He} \rightarrow ^6\text{Li}$), I finally get

$$\begin{aligned} \langle P_{6\text{Li}} \rangle &= \sum_{\text{T}, ^3\text{He}} \frac{\sum_i N_{3,i}}{N_3^{\text{tot}}} \int_{E_{\text{thr}}}^{E_3} dE n_{4\text{He}} \sigma_{6\text{Li}}(E_3) \left(\frac{dx}{dE} \right)_{\text{Coulomb}} \\ &= 1.09 \times 10^{-7} Z^{-2} \frac{\sum_i N_{3,i}}{N_3^{\text{tot}}} \left(\left(\frac{E_{3,i}}{\text{MeV}} \right)^2 - \left(\frac{E_{\text{thr}}}{\text{MeV}} \right)^2 \right). \end{aligned} \quad (4.61)$$

Evaluating the sum leads to the probabilities for an energetic tritium or a ^3He to produce a ^6Li nucleus

$$\langle P_{\text{T}^4\text{He} \rightarrow \text{n}^6\text{Li}} \rangle \approx 2 \times 10^{-6} \quad (4.62)$$

and

$$\langle P_{^3\text{He}^4\text{He} \rightarrow \text{p}^6\text{Li}} \rangle \approx 5 \times 10^{-7}. \quad (4.63)$$

The number of ^6Li nuclei produced per antiproton annihilation is thus

$$N_{6\text{Li}} \approx (P_{\text{T}} P_{\text{T}^4\text{He} \rightarrow \text{n}^6\text{Li}} + P_{^3\text{He}} P_{^3\text{He}^4\text{He} \rightarrow \text{p}^6\text{Li}}) \left(\frac{\sigma_{\bar{p}^4\text{He}}}{\sigma_{\bar{p}p}} \right) \left(\frac{n_{4\text{He}}}{n_p} \right) \approx 1.8 \times 10^{-8} \left(\frac{Y_p}{0.25} \right), \quad (4.64)$$

where P_{T} and $P_{^3\text{He}}$ are the probabilities to get tritium or ^3He in a $\bar{p}^4\text{He}$ annihilation (see Tab. 4.3). A simple estimate for the total additional $^6\text{Li}/\text{H}$ abundance, $\Delta_{6\text{Li}}$, is thus

$$\Delta_{6\text{Li}} \approx \Delta_{4\text{He}}^{\text{ann}} N_{6\text{Li}}. \quad (4.65)$$

The decrease in $^4\text{He}/p$ due to annihilation, $\Delta_{4\text{He}}^{\text{ann}}$, is roughly given by the antimatter to proton ratio after the BBN epoch, which can be approximately written in terms of the antimatter fraction R^{after} at that time, $(n_{\bar{p}}/n_p)^{\text{after}} \approx R^{\text{after}}/(1 - R^{\text{after}})$. Putting in the numerical values and using $R^{\text{after}}/(1 - R^{\text{after}}) \approx R^{\text{after}}$ for $R^{\text{after}} \ll 1$, I find

$$\Delta_{6\text{Li}} \approx 1.8 \times 10^{-9} \left(\frac{R^{\text{after}}}{0.1} \right) \left(\frac{Y_p}{0.25} \right). \quad (4.66)$$

This is many orders of magnitude higher than the standard BBN value, $n_{6\text{Li}}/n_p = \mathcal{O}(10^{-13})$ and will therefore provide very stringent limits in some areas of the parameter space, as will be discussed in Sec. 5.

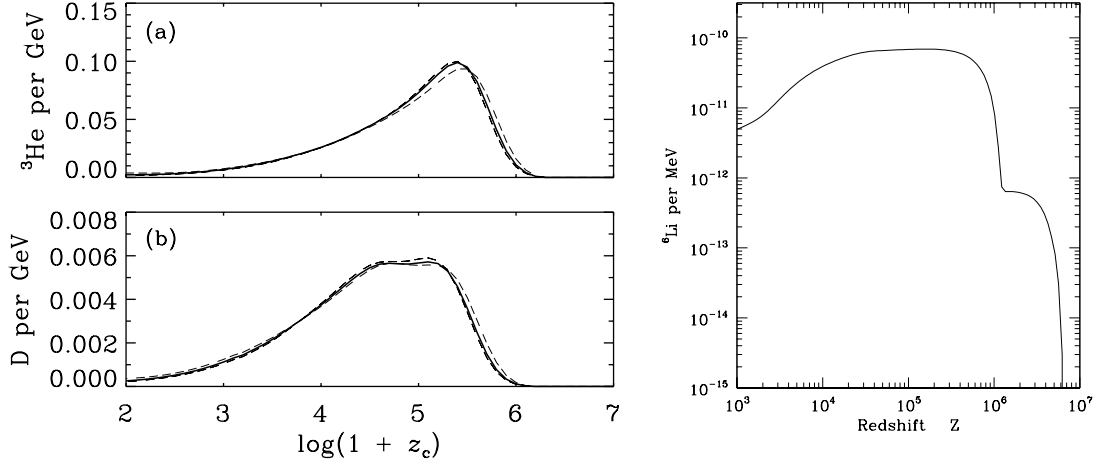


Figure 4.7: *Left panel:* Number of ${}^3\text{He}$ and deuterium produced by ${}^4\text{He}$ photodisintegration per GeV of non-thermal electromagnetic energy injected at redshift z_c . Results are shown for three combinations of the Hubble parameter H_0 and the baryonic contribution to the critical density Ω_b , $H_0 = 40/\Omega_b = 0.125$ (dotted curves), $70/0.025$ (full curves), and $100/0.01$ (dashed curves). Taken from Protheroe et al. (1995). *Right panel:* Total number of ${}^6\text{Li}$ nuclei produced per MeV of energy in energetic electromagnetically interacting particles injected at an epoch with redshift z . Taken from Jedamzik (1999).

Photodisintegration

In each annihilation process about 50% of the energy is released in electromagnetically interacting particles. If the size of the antimatter regions is such that matter-antimatter annihilation takes place at temperatures below the pair annihilation, $T \lesssim 30$ keV, the injected particles initiate an electromagnetic cascade via photon-photon pair production

$$\gamma + \gamma_{\text{bg}} \rightarrow e^+ + e^-$$

and inverse Compton scattering

$$e + \gamma_{\text{bg}} \rightarrow e' + \gamma'$$

on background photons until the energies of the gamma rays drop below the pair production threshold. The resulting photon spectrum, which is fairly independent of the details of the injection mechanism, may photodisintegrate ${}^4\text{He}$ nuclei and thus modify the element abundances (Lindley 1980, Aharonian, Kirillov-Ugryumov & Varadanian 1985, Berezhinskii, Bulanov, Dogiel & Ptuskin 1990, Kawasaki & Moroi 1995, Protheroe et al. 1995, Jedamzik 1999). Since the characteristic interaction rates are initially much higher than the expansion of the Universe, one may assume that this zero generation cascade spectrum is formed instantly. The maximum energy in the spectrum is

$$E_C(z) = 4.7 \times 10^4 (1 + z)^{-1} \text{ GeV} \quad (4.67)$$

for redshifts above $z = 10^3$. Photodisintegration of ${}^4\text{He}$ may only be efficient, if $E_C(z)$ exceeds the threshold of $E_{{}^4\text{He}} \approx 20$ MeV. Cascade nucleosynthesis is therefore only important for redshifts $z \lesssim 2 \times 10^6$, corresponding to annihilation at temperatures below $T \lesssim 5 \times 10^{-4}$ MeV. Since the cascade spectrum is independent of the energy distribution of the injected particles, the number of ${}^3\text{He}$ and deuterium nuclei produced may be expressed as a function of the total energy injected in form of electromagnetically interacting particles (see left panel of Fig. 4.7, which I borrowed from Protheroe et al. 1995).

A further effect has recently been described by Jedamzik (1999). Energetic ${}^3\text{He}$ and tritium nuclei created in the photodisintegration of ${}^4\text{He}$ may lead to the formation of ${}^6\text{Li}$, in an analogous manner as was discussed above for energetic secondary nuclei originating in the initial annihilation process. In the right panel of Fig. 4.7, which is taken from Jedamzik (1999) the number of ${}^6\text{Li}$ nuclei produced per MeV nonthermal electromagnetic energy injected is shown. Over a wide range of redshifts, $2 \times 10^4 \lesssim z \lesssim 4 \times 10^5$, the number of ${}^6\text{Li}$ nuclei produced is of the same order as for production via secondary tritium and ${}^3\text{He}$, cf. Eq. (4.64). Since about 1 GeV electromagnetic energy is injected per annihilation event, the two numbers may be compared directly. Limits on the presence of antimatter from this effect may generally be stronger than the limits from ${}^3\text{He}$ and tritium photoproduction, as I will show in Sec. 5.

Chapter 5

BBN with Antimatter

After having laid down the foundations of the physics of the dissipation of matter-antimatter regions in the early Universe, and of the theory of the synthesis of the light elements, I will now proceed and bring the two together. In Sec. 5.1, I start by stating the initial conditions used for the simulations. Some aspects of the annihilation region will be discussed in the Sec. 5.2. In the remainder of this chapter, I will describe the impact which matter-antimatter regions in the early Universe may have on the light element abundances. Three different limiting cases will be distinguished, according to the segregation scale of matter and antimatter, or equivalently, the approximate matter-antimatter annihilation time. In Sec. 5.3, annihilations well before weak freeze out, i.e. well before the n/p -ratio departs from its equilibrium value, will be discussed. Annihilations after weak freeze out, but before the synthesis of ${}^4\text{He}$ at a temperature of $T_{4\text{He}} \approx 80 \text{ keV}$ will be investigated in Sec. 5.4, before I scrutinize in Sec. 5.5 the influence of annihilations during the era between the completion of nucleosynthesis and recombination of electrons and protons at $z \approx 10^3$, corresponding to $T \approx 0.2 \text{ eV}$. In Sec. 5.6, I summarize the results by showing the detailed abundance yields for the primordial elements for the parameter region under consideration in this work.

Some of the results presented in this chapter were already published by the author in Rehm & Jedamzik (1998).

5.1 Initial Conditions

The initial conditions common to all scenarios investigated in this work were discussed in Sec. 4.1, but to interpret the results of the numerical simulations it is in order to summarize them at this point.

Initially, the Universe is taken to consist of a distribution of matter and antimatter regions with the baryonic density n_b in the matter region equal to the antibaryonic density $n_{\bar{b}}$ in the antimatter region (cf. Fig. 4.1). This distribution is approximated by a set of spherical shells filled with either matter or antimatter. The antimatter is concentrated in the inner shells, extending from the origin to r_A^{100} . Due to the assumption of equal densities, the fraction of antimatter present in the early Universe is controlled by the volume

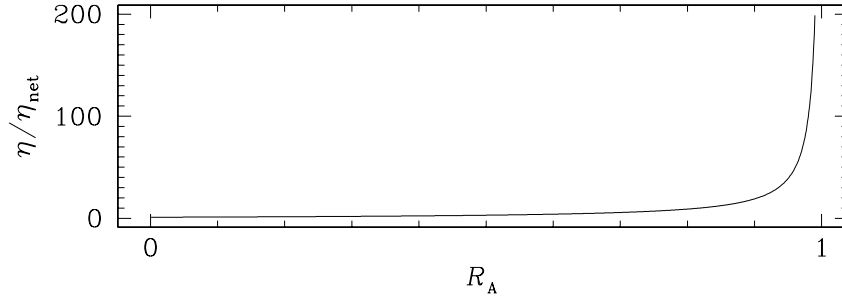


Figure 5.1: η/η_{net} as a function of the antimatter-to-matter ratio R_A

fraction $f_{\bar{b}}$ occupied by the antimatter region. The initial (anti-)baryon-to-photon ratio η in the respective region is thus fixed at $\eta = \eta_{\text{net}} R_A / (1 - R_A)$, as soon as the average net baryon-to-photon ratio $\eta_{\text{net}} = \bar{n}_{\text{net}}/n_\gamma$ (cf. Eq. 4.1) and the antimatter-to-matter ratio R_A are chosen. This is displayed in Fig. 5.1. In all simulations η_{net} was kept at a constant value of $\eta_{\text{net}} = 3.4 \times 10^{-10}$.

5.2 The Annihilation Region

Annihilation of matter and antimatter is only possible if matter and antimatter regions are mixed. The mixing process, i.e. the transport of baryons and antibaryons over the matter-antimatter boundary, may only be accomplished by diffusion. Before the actual annihilation takes place, baryons and antibaryons may diffuse a short distance into the respective anti-region. These small regions around the boundary, where the annihilations mainly take place, constitute the annihilation region. In order to annihilate the whole antimatter region, matter and antimatter has however to be transported towards the boundary, over a distance large compared to the annihilation region. This transport process proceeds via baryon diffusion, as long as the early Universe is in pressure equilibrium. At some point, however, baryonic density gradients in the Universe may not be maintained any more, since the photon mean free path increases strongly and thus the assumption of pressure equilibrium, which is supported by temperature gradients opposing the baryonic density gradients, breaks down. Thus the regions far away from the annihilation region, which are at average cosmic density, quickly expand towards the annihilation region, in which the density is decreased due to the annihilations. For this reason, the dominant transport process at late times is hydrodynamic expansion towards the low density annihilation region. The length scales of the two processes, transport to and diffusion within the annihilation region, are very different and thus difficult to treat numerically. In this section I will argue why spatial resolution of the annihilation region is not crucial for the problem at hand. In order to do so, the annihilation region has to be studied in some detail.

In case of annihilation via neutrons, i.e. $T_{\text{ann}} \gtrsim T_{4\text{He}} \approx 80 \text{ keV}$, diffusion within the annihilation region is — according to the local baryon-to-photon ratio η_{ann} — dom-

inated either by magnetic moment scattering on electrons and positrons ($\eta_{\text{ann}} \lesssim 10^{-8}$), or by nuclear scattering on protons ($\eta_{\text{ann}} \gtrsim 10^{-8}$). In both cases, the typical scattering time for neutrons is much smaller than the annihilation time,

$$\begin{aligned} \frac{\tau_{ne\pm}}{\tau_{\text{ann}}} &= \frac{(\sigma_{ne} v_b n_{e\pm})^{-1}}{(\sigma_{\text{ann}} v_b n_b^{\text{ann}})^{-1}} \\ &\approx \frac{(8 \times 10^{-4} \text{ mb } \sqrt{T/m_N})^{-1}}{(40 \text{ mb } \eta_{\text{ann}})^{-1}} \approx 6 \times 10^{-4} \left(\frac{T}{\text{MeV}} \right)^{-1/2} \left(\frac{\eta_{\text{ann}}}{4 \times 10^{-10}} \right) \end{aligned} \quad (5.1)$$

and

$$\begin{aligned} \frac{\tau_{np}}{\tau_{\text{ann}}} &= \frac{(\sigma_{np} v_b n_p)^{-1}}{(\sigma_{\text{ann}} v_b n_b^{\text{ann}})^{-1}} \\ &\approx \frac{(2 \times 10^4 \text{ mb } \sqrt{T/m_N})^{-1}}{(40 \text{ mb})^{-1}} \approx 6 \times 10^{-2} \left(\frac{T}{\text{MeV}} \right)^{-1/2}. \end{aligned} \quad (5.2)$$

Here v_b is a typical baryon thermal velocity, n_b^{ann} the antibaryon density in the annihilation region, and m_N the nucleon rest mass. Neutron scattering is thus always more probable than annihilation. The relevant cross sections are $\sigma_{ne} \approx 8 \times 10^{-4} \text{ mb}$, $\sigma_{np} \approx 2 \times 10^4 \text{ mb}$, and $\sigma_{\text{ann}} v_b \approx 40 \text{ mb } c$ (see Sec. 4.3.1). Note that Eqs. (5.1, 5.2) assume an electron density roughly equal to the photon density, $n_{e\pm} \approx n_\gamma$, which is appropriate at early times before e^\pm annihilation, when neutron diffusion is important. In the numerical computations, however, I follow the exact densities of the species.

Annihilation via protons happens only in the keV era, where proton diffusion is limited by Thomson scattering of the electrons in the ‘electron-proton system’ off the ambient photons. Even though transport of the protons may now be controlled by hydrodynamic expansion, the movement of the particles over the boundary and inside the annihilation region is still described by diffusion. If I compare the Thomson interaction time (cf. Tab. 4.1) with the annihilation time for protons (see Eq. 4.34),

$$\begin{aligned} \frac{\tau_{e\gamma}}{\tau_{\text{ann}}} &= \frac{(\sigma_{e\gamma} v_b n_\gamma)^{-1}}{(\sigma_{\text{ann}} v_b n_b^{\text{ann}})^{-1}} \\ &\approx \frac{(6.7 \times 10^2 \text{ mb } \sqrt{T/m_N})^{-1}}{(32 \text{ mb } \sqrt{\text{MeV}/T} \eta_{\text{ann}})^{-1}} \approx 6 \times 10^{-7} \left(\frac{T}{\text{keV}} \right)^{-1} \left(\frac{\eta_{\text{ann}}}{4 \times 10^{-10}} \right), \end{aligned} \quad (5.3)$$

I find that the scattering time scale is again much shorter than the annihilation time scale. In both cases, the width of the annihilation region l^{ann} is thus given by the distance $d(\tau_{\text{ann}})$ nucleons can diffuse into the respective anti-region during their typical lifetime against annihilation τ_{ann} ,

$$l^{\text{ann}} \approx 2 d(\tau_{\text{ann}}) \approx 2 \left(\int_0^{\tau_{\text{ann}}} 6D(t) dt \right)^{1/2} \approx 2 \sqrt{6D\tau_{\text{ann}}}. \quad (5.4)$$

I have included a factor of 2 to allow for diffusion of matter into the antimatter region as well as of antimatter into the matter region. The diffusion constant D can be taken to be constant over the lifetime against annihilation, such that the integral can be evaluated immediately. In order to calculate τ_{ann} , I need to estimate the density in the annihilation region. I assume that a steady state between diffusion of baryon number into the annihilation region and the annihilation of this baryon number is established. The concept of a steady state is only appropriate for times somewhat shorter than the Hubble time, since the densities and diffusion constants vary with the expansion of the Universe. A typical baryonic density gradient some distance away from the annihilation region will however always be of the order of $\Delta n_b / d_b(\tau_{\text{Hubble}})$, with $d_b(\tau_{\text{Hubble}})$ the diffusion length scale over one Hubble time. The difference in baryon density is given by $\Delta n_b = \tilde{n}_b - n_b^{\text{ann}}$, with \tilde{n}_b the baryon density far away from the annihilation region and n_b^{ann} the baryon density within the annihilation region. The baryon density in the annihilation region will typically be much smaller than \tilde{n}_b ; therefore I replace Δn_b by \tilde{n}_b . This leads me to approximate the baryon number flux F_b into the annihilation region by

$$F_b = D \nabla n_b A \approx D \frac{\Delta n_b}{d_b(\tau_{\text{Hubble}})} A \approx D \frac{\tilde{n}_b}{d_b(\tau_{\text{Hubble}})} A. \quad (5.5)$$

The number of annihilations in a volume with surface A and width l^{ann} should then be equal to the flux of baryons into the volume,

$$\sigma_{\text{ann}} v_b n_b^{\text{ann}} n_b^{\text{ann}} A l^{\text{ann}} = D \frac{\tilde{n}_b}{d_b(\tau_{\text{Hubble}})} A. \quad (5.6)$$

As long as the diffusion length is considerably smaller than the width of the antimatter region, \tilde{n}_b is equal to the initial matter density, $\tilde{n}_b = \bar{n}^{\text{net}} \Delta^0$, where Δ^0 is the initial baryon overdensity (cf. Sec. 4.2.1) and \bar{n}^{net} the initial average net baryon density (see Eq. 4.1). I may now compute the baryon density in the annihilation region. Inserting the annihilation length l^{ann} , Eq. (5.4), into Eq. (5.6) and using $\tau_{\text{ann}} = (\sigma_{\text{ann}} v_b n_b^{\text{ann}})^{-1}$ yields

$$\sigma_{\text{ann}} v_b n_b^{\text{ann}} n_b^{\text{ann}} 2A \sqrt{\frac{6D}{\sigma_{\text{ann}} v_b n_b^{\text{ann}}}} = D \frac{\bar{n}^{\text{net}} \Delta^0}{\sqrt{D} \tau_{\text{Hubble}}} A. \quad (5.7)$$

The baryon and antibaryon density within the annihilation region should be of the same magnitude, thus I finally obtain for the baryon density in the annihilation region

$$n_b^{\text{ann}} = \left(\frac{(\bar{n}^{\text{net}} \Delta^0)^2}{6 \sigma_{\text{ann}} v_b \tau_{\text{Hubble}}} \right)^{1/3}. \quad (5.8)$$

This may be written in terms of the local baryon overdensity Δ^{ann} in the annihilation region as

$$\Delta^{\text{ann}} \equiv \frac{n_b^{\text{ann}}}{\bar{n}^{\text{net}}} = 2.4 \times 10^{-3} (\Delta^0)^{2/3} \left(\frac{\sigma_{\text{ann}} v_b}{40 \text{ mb } c} \right)^{-1/3} \left(\frac{\text{MeV}}{T} \right)^{1/3} \left(\frac{\eta}{4 \times 10^{-10}} \right). \quad (5.9)$$

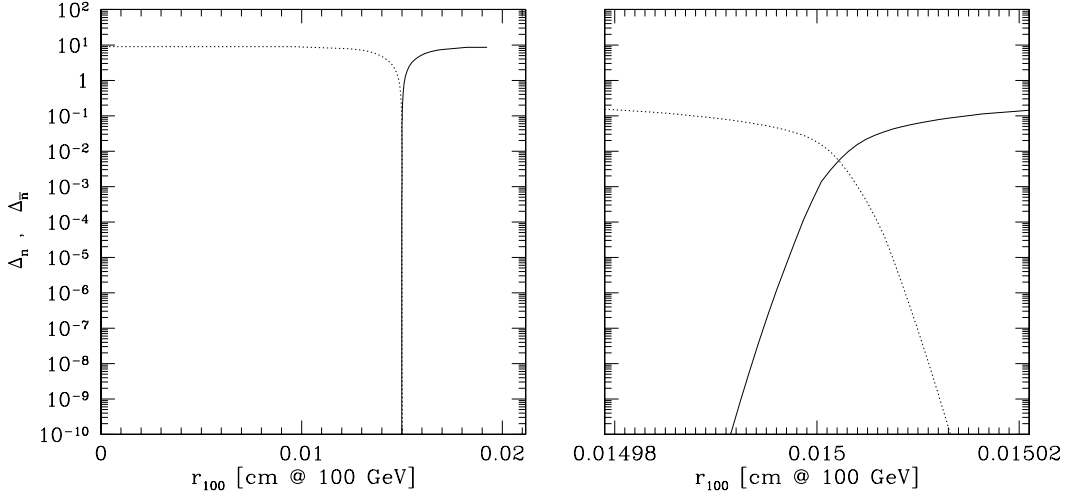


Figure 5.2: *Left panel:* Snapshot of the neutron (full line) and the antineutron (dotted line) overdensity, Δ_n and $\Delta_{\bar{n}}$ at a temperature of $T \approx 10$ MeV. This distribution was obtained with a high resolution simulation; the antimatter parameters were $R_A = 0.9$ and $r_A^{100} = 1.5 \times 10^{-2}$ cm. *Right panel:* Zoom into the annihilation region. See text for discussion.

Interestingly, the overdensity in the annihilation region Δ^{ann} is independent of the diffusion constant. I may now calculate the width of the annihilation region in comoving units (see Sec. 4.1),

$$l_{100}^{\text{ann}} = \frac{2}{R} \left(\frac{6D}{\sigma_{\text{ann}} v_b \bar{n}_{\text{net}} \Delta^{\text{ann}}} \right)^{1/2}. \quad (5.10)$$

Using the relevant diffusion constants (see Tab. 4.1) and annihilation cross sections (Sec. 4.3.1) and further assuming $\eta_{\text{net}} = 4 \times 10^{-10}$, I obtain

$$l_{100}^{\text{ann}} = 2 \times 10^{-4} \text{ cm } (\Delta^0)^{-1/3} \left(\frac{T}{\text{MeV}} \right)^{-19/12} \quad (5.11)$$

for annihilation via neutron diffusion and

$$l_{100}^{\text{ann}} = 1.3 \times 10^{-1} \text{ cm } (\Delta^0)^{-1/3} \left(\frac{T}{\text{keV}} \right)^{-17/12} \quad (5.12)$$

for annihilation via proton diffusion. I have numerically verified Eq. (5.11) for a scenario with antimatter regions of size $r_A^{100} = 1.5 \times 10^{-2}$ cm and an initial overdensity $\Delta^0 \approx 10$, corresponding to a matter-antimatter ratio of $R_A = 0.9$. In order to check the validity of the assumption of a steady state, I had to let the code evolve at least over the period of one Hubble time. The two snapshots of the neutron and antineutron overdensity, Δ_n and $\Delta_{\bar{n}}$ were obtained in a simulation which was started at $T \approx 20$ MeV, and evolved

down to $T \approx 10$ MeV. The left panel shows the whole simulation volume, while the right panel is a zoom into the annihilation region of the same simulation. The resolution is fine enough to describe (anti-)neutron diffusion *within the annihilation region*. I find an overdensity in the central region of $\Delta^{\text{ann}} \approx \text{a few } 10^{-3}$ which may be compared to the above estimate, $\Delta^{\text{ann}} \approx 3 \times 10^{-3}$. The width of the annihilation region is $l_{100}^{\text{ann}} \approx 10^{-6}$ cm, following Eq. (5.11).

Since the two relevant processes — transport of particles through their own region towards the annihilation region and diffusion within the anti-region — proceed on length scales which differ by orders of magnitude, it is very time-consuming to run simulations with the resolution necessary to adequately describe both processes. The numerical results presented in this work were obtained at a resolution which properly resolves the transport processes over the distance of order of the domain size, but does not resolve the diffusion within the annihilation region. This should however affect the results little, since the exact composition of the annihilation region is not decisive for the final abundances.

In case of annihilation before ${}^4\text{He}$ synthesis, the exact annihilation time is crucial for my results, as will become clear in Sec. 5.4. Protons hardly play a role in case of early annihilation due to their very short diffusion length. The protons which are originally present in the annihilation region are quickly annihilated. Additional protons may not be transported into the annihilation region and their density profile remains frozen in. The annihilation region is thus populated by neutrons and antineutrons only, and further annihilation may only proceed via neutrons and antineutrons. All particles which reach the annihilation region will inevitably be annihilated on a very short time scale compared to the transport time. Thus the time scale for annihilation of all antimatter is set by the transport of neutrons and antineutrons towards the annihilation region, hence over considerably longer distances than the annihilation region, which are properly resolved.

In case of annihilation after the disappearance of free neutrons at a temperature of $T_{4\text{He}} \approx 80$ keV, the dominant channels are $\bar{p}p$ and $\bar{p}{}^4\text{He}$. The ratio of annihilations on either ${}^4\text{He}$ or on protons is important, since this ratio determines how many secondary nuclei, which arise in ${}^4\text{He}$ disruption, are produced for a given antimatter fraction. This ratio depends again on the transport of the nuclei over the whole matter region into the annihilation region. The transport time scale may either be set by charged particle diffusion or by hydrodynamic expansion. For both processes, resolution of the whole simulation volume is important, but since again all nuclei which reach the annihilation region are inevitably annihilated, the spatial distribution of the nuclei within the annihilation region should be of negligible importance.

The effect of not resolving the annihilation region is that matter and antimatter may travel further into the respective anti-region than is physically correct. But since in both cases discussed above the number of annihilations on a specific nucleus at a specific time is set by the transport processes, this lack of resolution should not be relevant. The relative independence of the results on the exact structure of the annihilation region is also evident by resolution studies given in the appendix.

Energetic secondary nuclei arising in the ${}^4\text{He}$ disruption process may only escape

from the annihilation region and thus influence the final abundance yields if their stopping length is much larger than the annihilation region. The correct treatment of this effect is therefore independent of whether or not diffusion within the annihilation region is resolved.

5.3 Annihilations Well Before Weak Freeze Out

Annihilation of antimatter before, or during, the BBN era may be an astonishingly quiescent process. For local net antibaryon-to-photon ratios not vastly exceeding the net cosmic average baryon-to-photon ratio, which are studied in this work, the entropy release associated with annihilation is only a minute fraction of the entropy in the photon-pair plasma. Heating of the plasma is therefore unimportant. In the absence of turbulent fluid motions and convective processes, mixing of matter and antimatter should mainly proceed via (anti-)baryon diffusion.

Diffusion of neutral baryons is governed by magnetic moment scattering on electrons and positrons and, for large densities, by nuclear scattering. Compared to the electrically charged protons, neutrons move most easily through the plasma (see Sec. 4.2.2). Neutrons and protons are however constantly interconverted with a rate of $\Gamma_{\text{weak}} \approx G_{\text{Fermi}}^2 T^5$. As long as $T \gtrsim 1$ MeV, the weak interactions are faster than the expansion of the Universe and the n/p ratio is kept at its equilibrium value of $n/p = \exp[-\Delta m/T]$. At early times, baryons may thus diffuse during the time they spend as neutrons.

Annihilation begins at very early times, as soon as matter and antimatter regions form, but only becomes substantial when baryon diffusion is effective, i.e. when the neutron diffusion length gets of the order of the the typical size of the domains. At times well before weak freeze out, when $T \gg 1$ MeV, neutrons and antineutrons diffuse from the matter into the antimatter region, or vice versa, and annihilate there either on (anti-)neutrons or (anti-)protons. Since the cross sections for both reactions are of similar magnitude, the annihilation rates are approximately given by the relative abundances of antineutrons and antiprotons. Nevertheless, annihilation proceeds mainly via (anti-)neutrons, since these particles may either diffuse out into the respective anti-region and be annihilated there, or may be annihilated in their own region by antiparticles which have diffused into that region. For protons and antiprotons on the other hand, only the second channel is possible, due to their very short diffusion length at that time. This preferential annihilation via neutrons leads to a reduction of the n/p ratio. Deviations from the equilibrium value are however quickly erased, as long as the weak interactions are effective. Since the weak interactions are very temperature dependent, re-establishing the equilibrium value is not possible any more if the annihilation happens close to weak freeze out.

This is illustrated in Fig. 5.3, where the neutron-to-proton ratio is shown as a function of temperature for some scenarios with annihilations prior to weak freeze out. In the upper three panels the antimatter fraction is low, $R_A = 0.05$, and the domain sizes $r_A^{100} = 0.0018, 0.018, \text{ and } 0.18$ cm, respectively. For such a small antimatter-to-matter ratio, the perturbation of the neutron-to-proton ratio is only weak. Moreover, for early

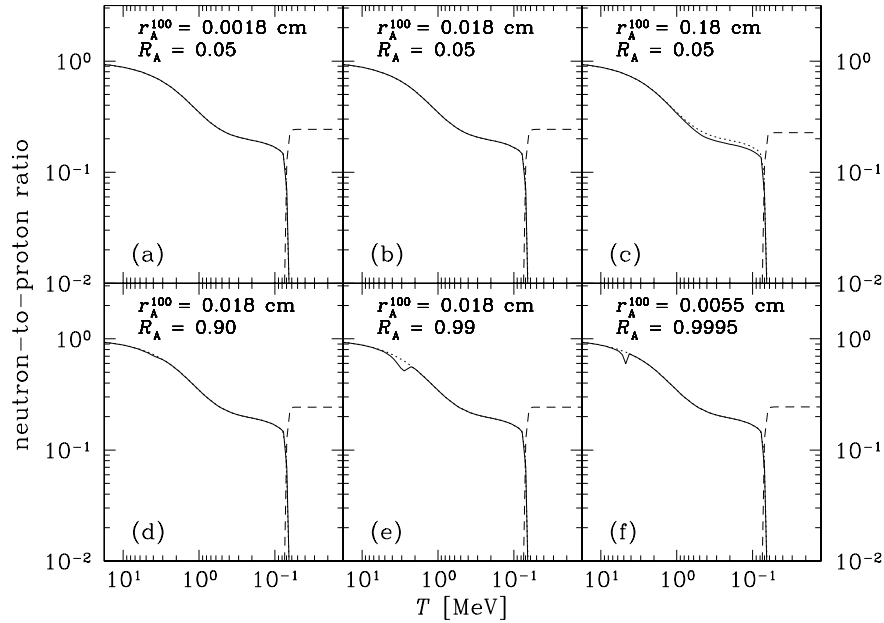


Figure 5.3: The neutron-to-proton ratio (solid line) and the ${}^4\text{He}$ mass fraction (dashed line) as a function of temperature for different sizes of the antimatter domains, r_A^{100} , and different values of the matter-to-antimatter ratio, R_A , as indicated in each panel. For comparison, the dotted line shows the unperturbed neutron-to-proton ratio in a Universe without antimatter.

annihilation corresponding to small r_A^{100} , the n/p ratio is nearly instantaneously reset to its equilibrium value which leads to an unchanged ${}^4\text{He}$ mass fraction (dashed line in Fig. 5.3). For comparison, the SBBN neutron-to-proton ratio is plotted also as a dotted line. In the first two cases, panel (a) and (b), $r_A^{100} = 0.0018$ cm and 0.018 cm, the two lines are indistinguishable from each other. Only when $r_A^{100} \gtrsim 0.1$ cm (panel c), the neutron-to-proton ratio deviates from the SBBN value. Here, annihilation proceeds very close to weak freeze out and thus the weak interactions are not fast enough any more to wash out the annihilation generated perturbation of the n/p ratio. This example represents a borderline case, since the modified n/p ratio will have an effect on the ${}^4\text{He}$ abundance yield, as I will discuss in the next section.

In the lower three panels, I show the results for considerably higher antimatter-to-matter ratios. For $R_A = 0.9$, $r_A^{100} = 0.018$ cm (panel d), the effect of the annihilations is hardly seen; the weak interactions are so fast that nearly no deviation from weak equilibrium occurs if antimatter is distributed on such small scales. The neutron-to-proton ratio may significantly depart from the equilibrium value during the annihilation period only for very high antimatter fractions close to unity. This is shown in panel (e) where $R_A = 0.99$ and $r_A^{100} = 0.018$ cm. But the weak interactions are still able to reset n/p to the equilibrium value subsequent to the complete annihilation of antimatter. An-

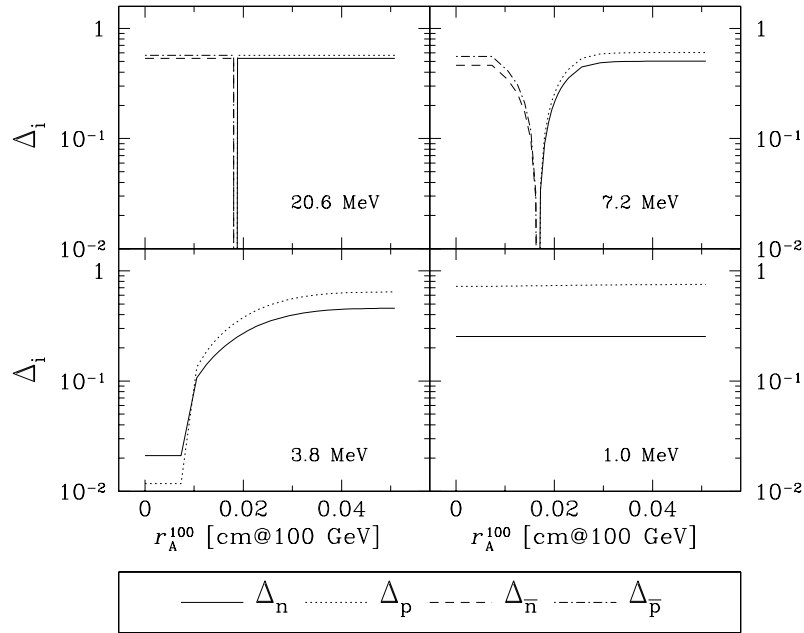


Figure 5.4: Snapshots of the (anti-)neutron and (anti-)proton density Δ_i (as indicated in the legend) for $R_A = 0.05$ and $r_A^{100} = 0.018$ cm, taken at the cosmic temperatures stated in each panel. See text for detailed discussion.

other example of this type is shown in panel (f), where $R_A = 0.9995$ and $r_A^{100} = 0.0055$ cm. Here too, the weak equilibrium is re-established. In all three cases the ${}^4\text{He}$ mass fraction is thus identical to the SBBN value.

In Fig. 5.4, I show the annihilation process in more detail by presenting four snapshots of the (anti-)neutron and (anti-)proton overdensity at the temperatures indicated in each of the four panels. The size of the antimatter domain is taken to be $r_A^{100} = 0.018$ cm and $R_A = 0.05$, as in panel (b) of Fig. 5.3. The first snapshot is taken at 20 MeV and represents the initial conditions. Neutron diffusion is not yet effective and thus baryons and antibaryons are confined to their respective regions. At $T \approx 7$ MeV neutrons already diffuse effectively and annihilation proceeds. Even though proton diffusion is inhibited by Coulomb scattering, the (anti-)proton density shows the same shape as the (anti-)neutron density, since the fast weak interactions keep the neutron-to-proton ratio at its equilibrium value everywhere. Annihilation is complete at $T \approx 4$ MeV, but the neutron and proton density is still inhomogeneous, since the former antimatter region is not yet completely filled with matter. Finally, at $T \approx 1$ MeV, neutrons and protons are distributed homogeneously throughout the Universe and their abundance ratio is given by its equilibrium value. The synthesis of the light elements, which will take place subsequently, proceeds as in a Universe which never possessed any antimatter regions. The light element abundances are thus not affected by antimatter which annihilates at sufficiently high temperatures, $T \lesssim 3 - 5$ MeV, depending somewhat on the

antimatter fraction (cf. also Figs. 5.10 – 5.12).

Nevertheless, when annihilation occurs close to weak freeze out, some residual effects of the perturbation of the n/p ratio remain (cf. panel (c) in Fig. 5.3). The exact value of the n/p ratio at $T_{4\text{He}} \approx 80$ keV is very important for the amount of ${}^4\text{He}$ synthesized in the early Universe, as I discussed in some detail in Sec. 3. It is thus of importance to determine in which scenarios annihilation of antimatter results in a deviation of the n/p ratio from the SBBN value at that time. The domain length scale at which annihilation starts to have an effect on the n/p ratio, and thus on the element abundances, depends on the antimatter fraction in a particular scenario. High antimatter fractions close to unity imply a high baryonic density, given the chosen initial conditions (see Fig. 5.1), and thus nuclear scattering starts to play a role. This affects the neutron diffusion length and delays annihilation somewhat. For antimatter fractions $R_A \approx 10^{-4}$, the antimatter domains may be as large as $r_A^{100} \approx 8 \times 10^{-2}$ cm without having an effect on the light element nucleosynthesis yields, whereas for values close to $R_A \approx 1$, BBN is already affected for $r_A^{100} \lesssim 2 \times 10^{-2}$ cm. The exact values for r_A^{100} where residual perturbations of the n/p ratio occur can be read off from Figs. 5.10 – 5.12 for a wide range of antimatter fractions.

Note also that due to the fact that the (anti-)neutrons, which diffuse out of the respective region, will be reproduced by the weak interactions, any amount of antimatter contained in regions smaller than $r_A^{100} \lesssim 10^{-2}$ cm may be annihilated at temperatures higher than $T_{4\text{He}}$ — even if it exceeds the neutron abundance at the time of annihilation — since there will never be a shortage of particles which are able to diffuse. This is in contrast to scenarios which have antimatter distributed on longer length scales, as I will show below.

5.4 Annihilations Between Weak Freeze Out and ${}^4\text{He}$ Synthesis

After weak freeze out, the weak interactions are dominated by neutron decay, and only few residual neutron-proton interconversions via the reactions $e^- + p \rightarrow n + \nu_e$ and $e^+ + n \rightarrow p + \bar{\nu}_e$ occur. Neutrons and antineutrons, which have diffused out of their own region and are annihilated in the respective anti-region, or have been annihilated in their own region by incoming antiparticles, may not be reproduced any more. Proton diffusion is still inhibited, and thus annihilation proceeds in this regime again mainly via (anti-)neutrons. This phenomenon of differential diffusion of (anti-)neutrons and (anti-)protons was first described by Steigman (1972, 1976) in the context of Omnès' model for a baryo-symmetric Universe. Differential diffusion is also essential to all studies of inhomogeneous BBN scenarios, regardless of the presence of antimatter, since it may lead to the formation of regions with different values for the neutron-to-proton ratio. The synthesis of the light elements proceeds differently in neutron rich or proton rich regions as compared to the standard scenario and thus the abundance yields may be modified (see e.g. Applegate et al. 1987, Fuller, Mathews & Alcock 1988, Jedamzik et al. 1994).

In the model under consideration in this work, differential diffusion of the charged

and neutral baryons may lead to a significant decrease in the neutron-to-proton ratio in the primordial plasma. Since the amount of ^4He synthesized crucially depends on the neutron-to-proton ratio at $T_{4\text{He}} \approx 80 \text{ keV}$, the decrease in free neutrons directly leads to a decrease in the final ^4He abundance (Rehm & Jedamzik 1998). The primordial mass fraction of ^4He in a scenario with early annihilation may be estimated analytically to be (see Eq. 3.8)

$$Y_p \approx \frac{2(n/p)}{1 + (n/p)} \Big|_{T_{4\text{He}}}.$$

If I assume that annihilation happens instantaneously, the neutron-to-proton ratio is modified as

$$\frac{n}{p} \Big|_{T_{4\text{He}}} \approx \left(\frac{(n_0/n_b) \exp[-\Delta t_1/\tau_n] - x R_A}{(p_0/n_b) - (1-x)R_A} \right) \exp[-\Delta t_2/\tau_n], \quad (5.13)$$

where x is the fraction of antibaryons annihilating on neutrons, n_0 and p_0 are the (pre-annihilation) neutron and proton densities at $T \approx 0.2 \text{ MeV}$, and n_b is the actual baryonic density in the matter region. Neutron decay is described by the two exponentials, where Δt_1 is the time between the moment after which the neutron fraction is (apart from annihilations) only affected by neutron decay ($T \approx 0.2 \text{ MeV}$) and the annihilation, while Δt_2 is the time remaining until neutrons are incorporated into ^4He at $T_{4\text{He}} \approx 80 \text{ keV}$. Thus the two limiting cases between which this estimate should hold are identified by $\Delta t_1 \approx 0 \text{ s}$, $\Delta t_2 \approx 130 \text{ s}$ (annihilation at $T \approx 0.2 \text{ MeV}$) and $\Delta t_1 \approx 130 \text{ s}$, $\Delta t_2 \approx 0 \text{ s}$ (annihilation at $T \approx 80 \text{ keV}$), respectively. The fraction $x \approx 1$, since there are practically no protons present in the annihilation region and thus most antineutrons annihilate on neutrons. The increase in the proton density due to neutron decay has been neglected.

As is apparent from Eq. (5.13), that the n/p ratio at $T_{4\text{He}}$ not only depends on the antimatter fraction R_A , but also on the time when annihilations take place. The reason for this behaviour is that the number of neutrons annihilated is roughly independent of the annihilation time, but for early annihilation this number is subtracted from a larger initial number than in case of later annihilation. This effect may be seen in the upper row of panels in Fig. 5.5, where I show the time evolution of the neutron-to-proton ratio for scenarios with annihilations occurring during and after the epoch of weak freeze out, but before the free neutrons are incorporated into ^4He . The antimatter fraction R_A is kept at a fixed value of $R_A = 0.1$. In panel (a), the length scale is chosen such that annihilation occurs relatively close to weak freeze out, $r_A^{100} = 0.55 \text{ cm}$, corresponding to $T_{\text{ann}} \approx 0.8 \text{ MeV}$. If r_A^{100} increases further and annihilation sets in at the beginning of the neutron decay dominated regime (panel b; $r_A^{100} \approx 1.5 \text{ cm}$, $T_{\text{ann}} \approx 250 \text{ keV}$), the final, post-annihilation n/p ratio is more strongly decreased, even though R_A is unchanged. Using the above estimate, I get $Y_p^{\text{est}} = 0.12$ for case (b), in excellent agreement with $Y_p \approx 0.13$ obtained in the numerical simulation, which is also shown in the figure as a dashed line. For $r_A^{100} = 5.5 \text{ cm}$, annihilation and substantial ^4He synthesis nearly coincide at $T_{\text{ann}} \approx 80 \text{ keV}$ (panel c). This constitutes the other limiting case, for which the effect on the n/p ratio and thus the ^4He decrease is maximal. The analytic estimate in this case is $Y_p^{\text{est}} \approx 0.09$ which matches the numerical result of $Y_p \approx 0.1$ equally well.

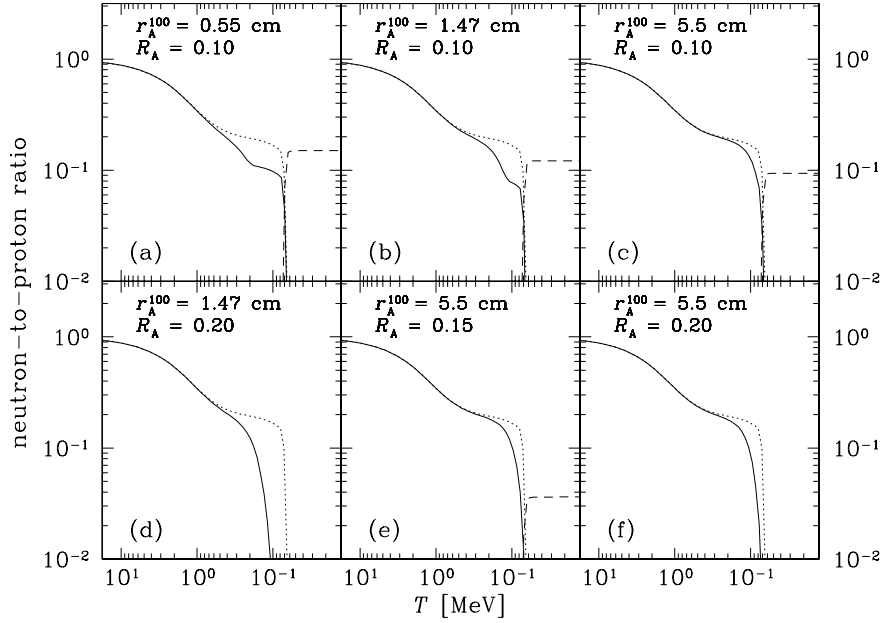


Figure 5.5: The neutron-to-proton ratio (solid line) and the ${}^4\text{He}$ mass fraction (dashed line) as a function of temperature for different sizes of the antimatter domains, r_A^{100} , and different values of the matter-to-antimatter ratio, R_A , which are indicated in each panel. For comparison, the dotted line shows the unperturbed neutron-to-proton ratio in a Universe without antimatter.

The above estimate Eq. (5.13) also predicts that it is possible to completely avoid ${}^4\text{He}$ and light element formation, namely if $n/p|_{T_{4\text{He}}} = 0$. (For antimatter fractions which yield negative results for n/p , Eq. (5.13) is obviously not applicable.) Thus there is no lower limit to the production of ${}^4\text{He}$. This is to my knowledge the only baryo-asymmetric scenario in which the production of ${}^4\text{He}$ and other nuclei may be totally suppressed (Rehm & Jedamzik 1998). Following Eq. (5.13), I find that in case of annihilation around $T \approx 0.2$ MeV an antimatter fraction of $R_A \approx 0.2$ annihilates all neutrons, while in case of annihilation close to ${}^4\text{He}$ synthesis, $R_A \approx 0.15$ should be sufficient. The corresponding numerical simulations for a no-nucleosynthesis Universe are shown in the lower three panels of Fig. 5.5. The estimate agrees well with the computed results for one of the two limiting cases (panel (d), annihilation at $T \approx 250$ keV). If one looks at the detailed results for this case, which are displayed in Fig. 5.6, it is apparent that indeed only a minute mass fraction of ${}^4\text{He}$ is synthesized. For the other limiting case (panel (e), I find a reduction of the ${}^4\text{He}$ yield by about a factor of 10 while Eq. (5.13) predicts $n/p \approx 0$ and thus no ${}^4\text{He}$ for $R_A \approx 0.15$. Given the accuracy of the analytic estimate for the other examples, this is still in good accordance. Only for $R_A \gtrsim 0.20$, the ${}^4\text{He}$ production will be totally suppressed (panel (f), cf. also Fig. 5.12).

The dominant effect of antimatter domains annihilating prior to $T_{4\text{He}}$ is thus a re-

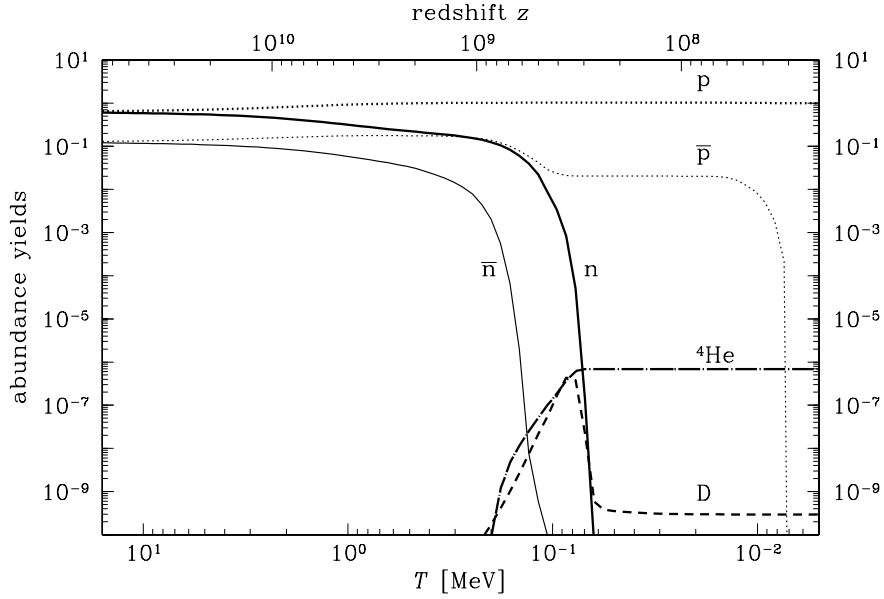


Figure 5.6: Abundance yields as a function of temperature for $R_A = 0.2$, $r_A^{100} = 1.47$ cm (cf. panel (d) in Fig. 5.5). Shown are the n (\bar{n}), p (\bar{p}), and ${}^4\text{He}$ mass fractions, and the number density of deuterium relative to hydrogen. Substantial nucleosynthesis cannot take place due to the near complete annihilation of all free neutrons prior to $T_{4\text{He}}$.

duction of the primordially synthesized ${}^4\text{He}$ mass fraction. Complete annihilation of all antibaryons (for $R_A \lesssim n/p$) is only possible if the antimatter domain size is smaller than the neutron diffusion length at a temperature somewhat larger than $T_{4\text{He}}$, since the diffusion of neutrons takes a finite amount of time. Further, neutrons have to diffuse not only over the antimatter region, but over the whole simulation volume, which is considerably larger for small antimatter fractions, $r_{100}^{\text{cell}} = r_A^{100}(R_A/(1 + R_A))$, see Appendix. In my numerical simulations, I find that for $r_A^{100} \lesssim 6$ cm annihilation will be complete at $T_{4\text{He}}$, while the neutron diffusion length at $T_{4\text{He}}$ is approximately $l_n^{100}(80 \text{ keV}) \approx 20$ cm, about a factor of three larger.

The abundances of the other light primordial elements, deuterium, ${}^3\text{He}$, and ${}^7\text{Li}$, are also affected by antimatter annihilation at $T \lesssim T_{4\text{He}}$, as may be seen in Fig. 5.7. In the figure, I show the evolution of the nuclear densities for the scenario displayed in panel (a) of Fig. 5.5 in more detail. Compared to the SBBN results (see Fig. 3.2), the abundance yields are reduced on a similar level as is the case for ${}^4\text{He}$. But since the observational uncertainties for the other primordial elements are much larger than for ${}^4\text{He}$, the decrease in the abundances is only relevant in models where the ${}^4\text{He}$ mass fraction is already unacceptably low. For a wide range of the parameters R_A and r_A^{100} , the detailed abundance yields are presented in Fig. 5.10 – Fig. 5.12 later in this chapter.

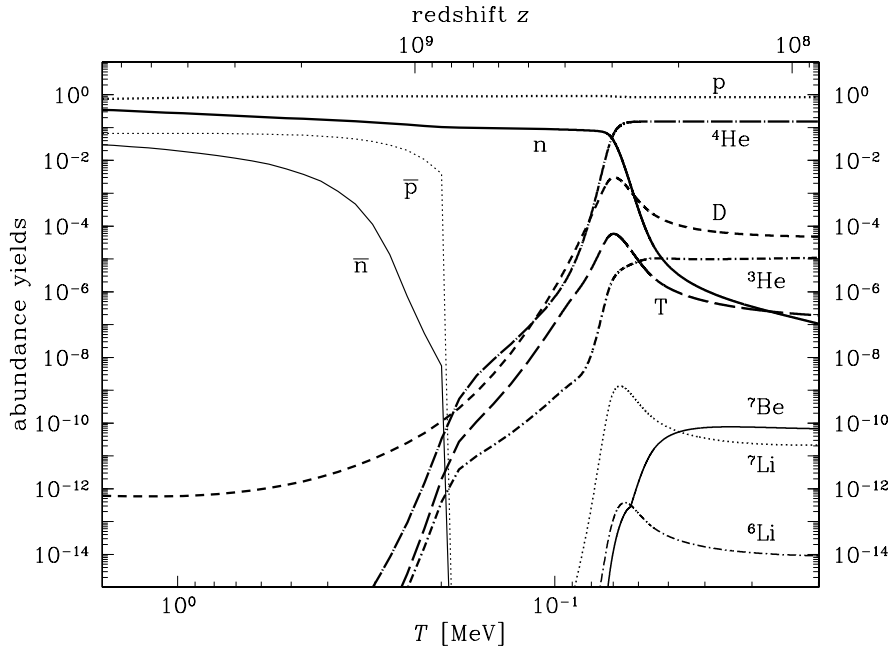


Figure 5.7: Abundance yields as a function of temperature for $R_A = 0.1$, $r_A^{100} = 0.55$ cm (cf. panel (a) in Fig. 5.5). Shown are the $n(\bar{n})$, $p(\bar{p})$, and ${}^4\text{He}$ mass fractions, and the number densities relative to hydrogen for the other elements.

5.5 Late Time Annihilation

Antimatter which is distributed on length scales larger than about $r_A^{100} \gtrsim 6$ cm may not annihilate via neutron diffusion, as I discussed in the previous section. The proton diffusion length at $T_{4\text{He}}$ is approximately 4×10^{-2} cm, nearly three orders of magnitude smaller than the neutron diffusion length. After the incorporation of all free neutrons into ${}^4\text{He}$, further mixing of matter and antimatter regions and thus annihilation is not possible until proton transport over a distance of $r_A^{100} \gtrsim 6$ cm is effective. The proton diffusion length does not grow to this value until the temperature drops down to a few keV. But at this low temperature, the photon mean free path has already increased enormously and thus baryonic density gradients in the primordial fluid may not be supported any more by opposing temperature gradients, as was discussed earlier. Thus the regions far away from the annihilation region, which are roughly at cosmic average density, quickly expand towards the baryon depleted and thus low-density annihilation region and thereby transport matter and antimatter towards the boundary. The annihilation time is thus controlled by the hydrodynamic expansion time scale at late times. Only the actual mixing, i.e. the transport over the boundary, is still described by baryon diffusion (see Sec. 4.2). The detailed studies which I have undertaken in this work allow one to gauge the annihilation epoch depending on the distance scale, as is displayed in

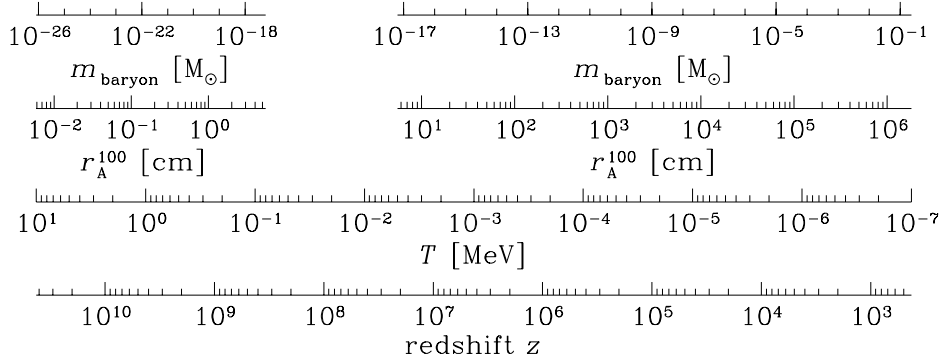


Figure 5.8: Spatial dimension of the antimatter regions and corresponding annihilation temperature for an antimatter fraction of $R_A = 0.1$. Also given is the baryonic mass in units of the solar mass M_\odot contained in the antimatter region and the annihilation redshift. Note that annihilation is stalled in the temperature range $T_{4\text{He}} \gtrsim T \gtrsim 5 \text{ keV}$, as is explained in the text.

Fig. 5.8. The annihilation process is stalled during the era where no mixing is possible, i.e. after the disappearance of free neutrons and before hydrodynamic expansion sets in ($80 \text{ keV} \lesssim T_{\text{ann}} \lesssim 3 \text{ keV}$), as is apparent in the figure. Antimatter domains with sizes $r_A^{100} = \mathcal{O}(\text{cm})$, corresponding to the boundary between early and late annihilation, will annihilate partly via neutron diffusion at $T > T_{4\text{He}}$ and partly via protons at $T = \mathcal{O}(\text{keV})$. The correspondence between length scale and annihilation temperature as well as the corresponding baryonic mass in Fig. 5.8 was obtained for $R_A = 0.10$, but remains approximately valid for other values of R_A on length scales $r_A^{100} \gtrsim 6 \text{ cm}$, as long as R_A is not close to unity, i.e. $R_A \lesssim 0.50$. In this case, the initial baryonic density does not differ by more than a factor of two from the net baryonic density (see Fig. 5.1).

The picture changes, however, for antimatter fractions on small length scales which exceed the neutron fraction. Even if the size of the antimatter region is smaller than the neutron diffusion length d_n^{100} at $T_{4\text{He}}$, annihilation may now not be completed due to the lack of neutrons, and thus antiprotons in domains of size comparable or even smaller than $d_n^{100}(T_{4\text{He}})$ may survive. These regions will then be annihilated as soon as proton transport on these scales is effective. This may happen at temperatures higher than a few keV, thus the gap in the annihilation temperature may disappear in such a scenario. Nevertheless, this class of models is in contradiction to the observations, since all neutrons will have been annihilated prior to $T_{4\text{He}}$ and no nucleosynthesis may take place. Apart from proton-antiproton annihilation at $T_{\text{ann}} < T_{4\text{He}}$, the situation is very similar to the no-nucleosynthesis models discussed at the end of the previous section.

If on the other hand the size of the antimatter region exceeds the neutron diffusion length at the BBN epoch when all available neutrons and antineutrons are built into ${}^4\text{He}$ and ${}^4\bar{\text{He}}$ nuclei ($r_A^{100} \gtrsim 6 \text{ cm}$), substantial annihilation via neutron diffusion is

not possible, regardless of the actual antimatter fraction R_A in a particular scenario. In models with segregation of matter and antimatter on such length scales, production of elements and anti-elements occurs in their respective domains.

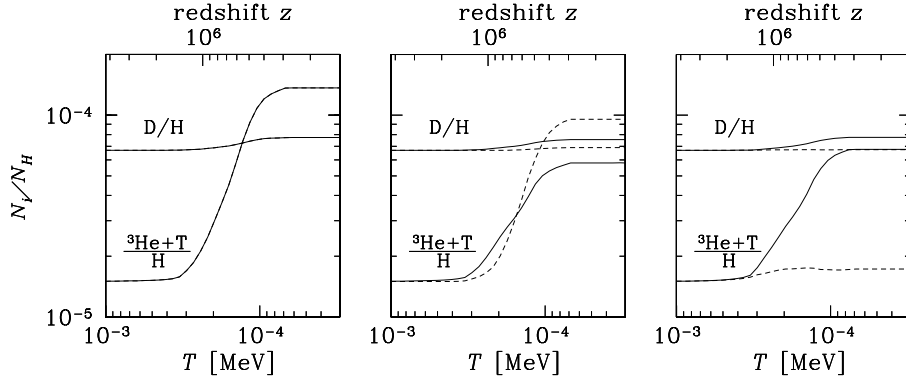
During the course of late time annihilation not only nucleon-nucleon, but also nucleon-nucleus annihilations may take place. The elemental abundances produced at the BBN epoch may now be substantially modified not only by direct annihilations, but also due to the effects of the secondary nuclei produced in nucleon-nucleus annihilations and due to photodisintegration of ${}^4\text{He}$ by energetic photons arising in the annihilation process (see Sec. 4.3.3). Any $\bar{p}{}^4\text{He}$ annihilation results in the production of energetic deuterium, tritium and ${}^3\text{He}$ nuclei with the relative probabilities given in Tab. 4.3, as well as protons and neutrons. Since annihilation of antimatter in a scenario where antimatter is distributed in well-defined domains is mainly confined to the region close to the matter-antimatter boundary, one might assume that secondary nuclei which are produced inside the annihilation region are also annihilated. But this is not necessarily the case. The secondary nuclei gain a kinetic energy of the order of a few tens of MeV in the ${}^4\text{He}$ disruption process (Balestra et al. 1988). The fraction which may survive the annihilation, depends on the distance the nuclei may travel away from the boundary before they are thermalized, see Eq. (4.50). Thus my results may deviate from scenarios with homogeneous injection of antimatter, which I briefly reviewed in Sec. 2.3. Batusov et al. (1984) used the first determination of the branching ratio $\bar{p}{}^4\text{He} \rightarrow \text{T}, {}^3\text{He}$ to put a limit of $R_A \lesssim 10^{-3}$ on the antimatter fraction which may be homogeneously injected after BBN took place. Since that time, the branching ratio has been re-measured and turned out to be a factor of 2.7 larger than the one used by Batusov et al. (1984), which tightens the bound on the antimatter fraction, $R_A \lesssim 3 \times 10^{-4}$. Further, in that work an overly restrictive limit of ${}^3\text{He}/\text{H} \lesssim 2 \times 10^{-5}$ was assumed. Using this outdated bound on ${}^3\text{He}/\text{H}$, I find weaker limits than Batusov et al. (1984), if antimatter is distributed in regions smaller than $r_A^{100} \lesssim 4 \times 10^2$ cm and thus annihilates at temperatures above $T_{\text{ann}} \gtrsim 10^{-4}$ MeV (see Fig. 5.10). This is due to the fact that some of the secondary nuclei will thermalize within the annihilation region and will thus be annihilated. For annihilations occurring at lower temperatures, the stopping length of the secondary nuclei increases beyond the annihilation region and a substantial part may escape from the annihilation region and thus survive annihilation. Since the increase of the stopping length of the energetic nuclei with cosmic time is faster than the growth of the domain size with the Hubble expansion (cf. Eq. 4.50), at some point practically all energetic nuclei (apart from the ones travelling into the antimatter region) survive and my limit should converge to the one found for the homogeneous case. This is, however, not true if photodisintegration is also taken into account.

Photodisintegration of ${}^4\text{He}$ kicks in at a temperature below $T \lesssim 4 \times 10^{-4}$ MeV and produces mainly energetic ${}^3\text{He}$ and tritium nuclei, the deuterium yields are down by factor of ten compared to the mass 3 yields (Protheroe et al. 1995). The photodisintegration yield for ${}^3\text{He}$ is peaked at a temperature of $T \approx 7 \times 10^{-5}$ MeV and becomes negligible below $T \approx 10^{-7}$ MeV, cf. Fig. 4.7. This behaviour is also reflected in the ${}^3\text{He}$ yields shown in Fig. 5.10. The peak at $r_A^{100} \approx 2 \times 10^3$ cm, corresponding to $T_{\text{ann}} \approx 10^{-4}$ is apparent, while for very late annihilation the limit eventually converges to the one

given by Batusov et al. (1984), if the correct branching ratio is used.

The importance of the energetic ${}^3\text{He}$ nuclei resulting from direct annihilation as well as from photodisintegration is twofold; they do not only directly increase the ${}^3\text{He}$ abundance, but may also lead to ${}^6\text{Li}$ production, as was recently pointed out by Jedamzik (1999), see also Sec. 4.3.3. In order to gauge the relative importance of the two effects which yield energetic ${}^3\text{He}$ nuclei, namely direct annihilation on ${}^4\text{He}$ and photodisintegration of ${}^4\text{He}$, I show in Fig. 5.9 results for simulations with $R_A = 10^{-3}$ and $r_A^{100} = 5.5 \times 10^2$ cm, in which annihilation occurs close to the photodisintegration peak ($T_{\text{ann}} \approx 5 \times 10^{-5}$ MeV). Shown are the abundance yields for deuterium and ${}^3\text{He}$ (upper row) and for ${}^6\text{Li}$ (lower row). In panels (a) and (d) all effects, photodisintegration as well as direct annihilation and escape from the annihilation region, are included. In the middle column of panels, (b) and (e), only one of the mechanisms is active at a time. The solid line shows the results for the production of deuterium, ${}^3\text{He}$, and ${}^6\text{Li}$ when only direct annihilation is taken into account, while the dashed line only considers ${}^4\text{He}$ photodisintegration induced production of these elements. I find that the photodisintegration yields for ${}^3\text{He}$ are stronger by nearly a factor of 2 compared to direct annihilation yields. This is not surprising, given the peak photodisintegration yield of about 0.1 ${}^3\text{He}$ nuclei per annihilation and the probability of direct ${}^3\text{He}$ production in a $\bar{p}{}^4\text{He}$ annihilation weighted by the relative abundance of ${}^4\text{He}$ to protons; $P_{3\text{He}+\text{T}}({}^4\text{He}/p) \approx 0.05$. For the production of ${}^6\text{Li}$ from energetic ${}^3\text{He}$ and tritium nuclei the results are similar, since the yields for ${}^6\text{Li}$ production via energetic nuclei generated by photodisintegration of ${}^4\text{He}$ and annihilation of ${}^4\text{He}$ are similar over a wide range of redshifts, $2 \times 10^4 \lesssim z \lesssim 4 \times 10^5$, cf. Sec. 4.3.3. The remaining two panels, (c) and (f), demonstrate the importance of the escape of the energetic secondaries from the annihilation region. The dashed line shows the results of a simulation where all annihilation products are confined to the annihilation region, while the solid line corresponds to a simulation where the secondary nuclei were distributed homogeneously throughout the simulation volume.

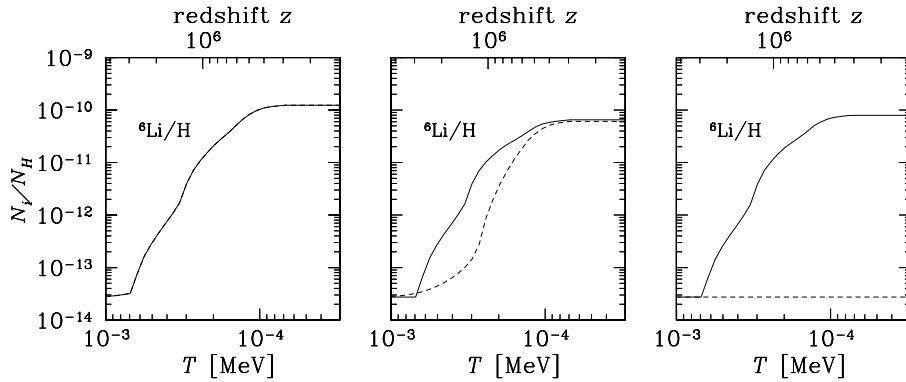
Note that all photodisintegration yields have been calculated using the generic γ -ray spectrum given by Protheroe et al. (1995). This is only correct as long as the energy of the injected photons, $E_\gamma \approx 200$ MeV (Steigman 1976), is smaller than the maximum energy in the spectrum, $E_C(z) \approx 4.7 \times 10^7 (1+z)^{-1}$ MeV, i.e. for $z \gtrsim 2 \times 10^5$, corresponding to $T_{\text{ann}} \gtrsim 4.5 \times 10^{-5}$. The results on scales larger than $r_A^{100} \gtrsim 10^3$ cm thus have to be interpreted with some care. In order to be able to give conservative limits, I have done simulations where photodisintegration was ignored which gave weaker limits by a factor of a few (see Fig. 6.1). Photodisintegration of deuterium, tritium and ${}^3\text{He}$ was not taken into account in any of my simulations. Due to the smaller binding energy as compared to ${}^4\text{He}$, photodisintegration of the lighter nuclei is effective at higher temperatures, $T_{\gamma D} \approx 5$ keV, $T_{\gamma {}^3\text{He}} \approx T_{\gamma T} \approx 2$ keV. If photodisintegration of ${}^4\text{He}$ takes place subsequently, the effect will however be quickly washed out. Thus photodisintegration of deuterium, tritium and ${}^3\text{He}$ may only be important if annihilation takes place below a temperature $T \approx 5$ keV, but is complete prior to the onset of ${}^4\text{He}$ photodisintegration at $T \approx 0.4$ keV. Direct production of deuterium, tritium and ${}^3\text{He}$ via annihilations on ${}^3\text{He}$ in this temperature range will, however, be stronger than the photodisintegration yields. The photodestruction factor for, e.g. deuterium, may be roughly estimated from



(a) Abundance yields for D/H and $(T+{}^3\text{He})/\text{H}$ obtained in a simulation where all relevant effects (photodisintegration, production of secondary nuclei in $\bar{p}{}^4\text{He}$ annihilation, escape of energetic nuclei from the annihilation region) are included.

(b) Abundance yields with only photodisintegration (dashed line) or only annihilation and escape (solid line) taken into account.

(c) Abundance yields with only annihilation taken into account. Secondaries either remain confined to the annihilation region (dashed line), or are homogeneously distributed throughout the simulation volume (solid line).



(d) Same as (a), but for ${}^6\text{Li}/\text{H}$.

(e) Same as (b), but for ${}^6\text{Li}/\text{H}$.

(f) Same as (c), but for ${}^6\text{Li}/\text{H}$.

Figure 5.9: Abundance yields for deuterium and ${}^3\text{He} + \text{T}$ (upper row), and ${}^6\text{Li}$ (lower row) obtained in consideration of the physical effects indicated in the respective sub-figure captions. The antimatter fraction in the simulations shown here is $R_A = 10^{-3}$ and the length scale $r_A^{100} = 5.5 \times 10^2$ cm.

the upper left panel of Fig. 4.7. The yields given in the figure are the *photoproduction* yields for ${}^3\text{He}$, or equivalently the *photodestruction* yields for ${}^4\text{He}$. Since the cross section for the competing process, i.e. Bethe-Heitler pair production on protons, does only slowly vary with temperature, these yields may be used at the relevant temperature range, $5\text{ keV} \lesssim T_{\text{ann}} \lesssim 0.4\text{ keV}$, but have to be scaled by the target abundances. Thus one expects a fraction of about $0.1({}^4\text{He}/\text{D}) \approx 10^{-4}$ deuterium nuclei per GeV electromagnetic energy injected to be photodisintegrated. Direct annihilation will however produce about $0.2({}^4\text{He}/p) \approx 10^{-2}$ deuterium nuclei per annihilation. Even though a fraction of those will thermalize within the annihilation region, it is well justified to neglect this effect. Spallation of ${}^4\text{He}$ via energetic neutrons should also be of minor importance, as was discussed in Sec. 4.3.3.

5.6 Modified Abundances

Concluding this chapter, I will present detailed results for the abundances of the light elements modified by the presence of matter-antimatter domains in the early Universe. The various physical processes which affect the abundances were discussed elsewhere in this work and will thus not be described again at this point. I performed a thorough scan of the two dimensional parameter plane spanned by the domain size r_{A}^{100} and the antimatter fraction R_{A} . The following figures show the results for small (Fig. 5.10), intermediate (Fig. 5.11) and high (Fig. 5.12) antimatter fractions. The fractional contribution of baryons to the critical density of the Universe, Ω_{b} , was kept at a constant value of $\Omega_{\text{b}} = 0.0125h_{100}^{-2}$, where h_{100} parameterizes the value of the Hubble parameter H_0 today, $h_{100} = H_0/(100\text{ km s}^{-1}\text{ Mpc}^{-1})$. The corresponding value of the SBBN parameter is $\eta = 3.4 \times 10^{-10}$.

Let us first consider a Universe which contains a small amount of antimatter of the order of a 10^{-3} to 10^{-2} of the cosmic baryon number (Fig. 5.10). If the length scales of the antimatter regions are such that annihilation takes place after weak freeze out, but is complete prior to the incorporation of neutrons into ${}^4\text{He}$ nuclei at $T_{4\text{He}} \approx 80\text{ keV}$, the main effect is the reduction of the neutron-to-proton ratio, and thus of the amount of ${}^4\text{He}$ synthesized (see top left panel of Fig. 5.10). This is a generic feature of all models with annihilations during that epoch, but will be even more pronounced for higher antimatter fractions. In this regime, i.e. for $r_{\text{A}}^{100} \lesssim 6\text{ cm}$, the other elements are less affected, the variations are below the observational uncertainties for these elements as may be seen in the other panels of Fig. 5.10. Going back to Fig. 3.4, one sees that this fact could improve the agreement between the currently favoured ‘low’ value for the primordial deuterium abundance (Refs. [3,5])¹ and the long standing ‘low’ ${}^4\text{He}$ determinations (Ref. [1]), as was pointed out by Rehm & Jedamzik (1998). Since both deuterium and ${}^7\text{Li}$ are only slightly affected, no relief can however be provided for the tension between the ${}^7\text{Li}$ measurements of Ref. [11] and the ‘low’ deuterium value, even if some lithium depletion is taken into account (Ref. [12]).

¹References are given to the observationally inferred light element abundances as compiled in Tab. 3.3, page 31

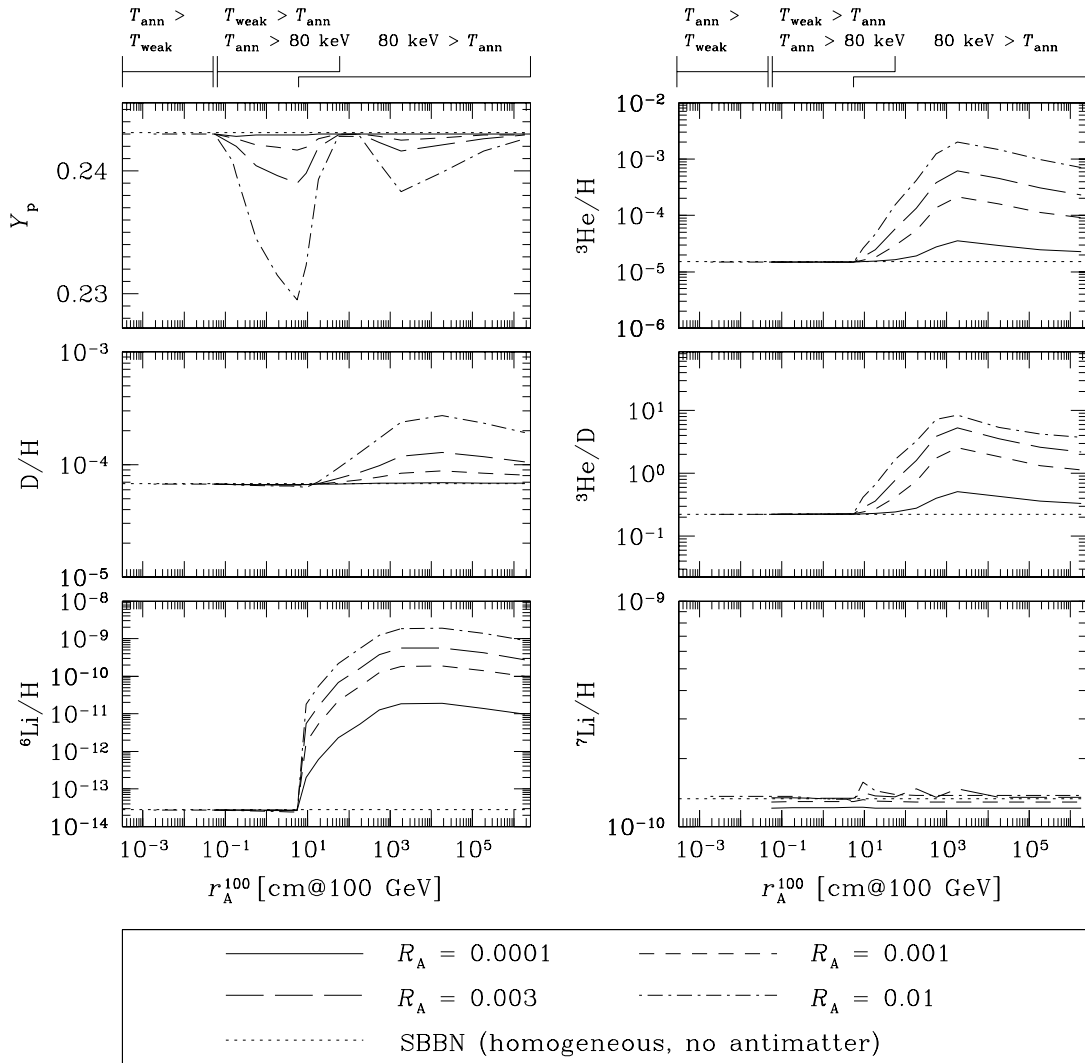


Figure 5.10: Results of BBN calculations in a Universe with antimatter domains. Shown are the ^4He mass fraction, the abundances of D, ^3He , ^6Li and ^7Li relative to hydrogen and the ratio of ^3He over D for several low values of R_A (see legend).

The picture is inverted, however, for annihilation at lower temperatures. If annihilation is complete by the end of ^4He synthesis at $T_{4\text{He}} \approx 80 \text{ keV}$, the ^4He mass fraction will virtually not be affected for small antimatter fractions, $R_A \lesssim 10^{-3}$. But since we are now in the regime of late time annihilation, energetic deuterium and mass three nuclei may be produced via direct annihilation and photodisintegration, which subsequently leads to ^6Li formation. If I apply the constraint $^3\text{He}/\text{D} < 1$, an antimatter fraction of

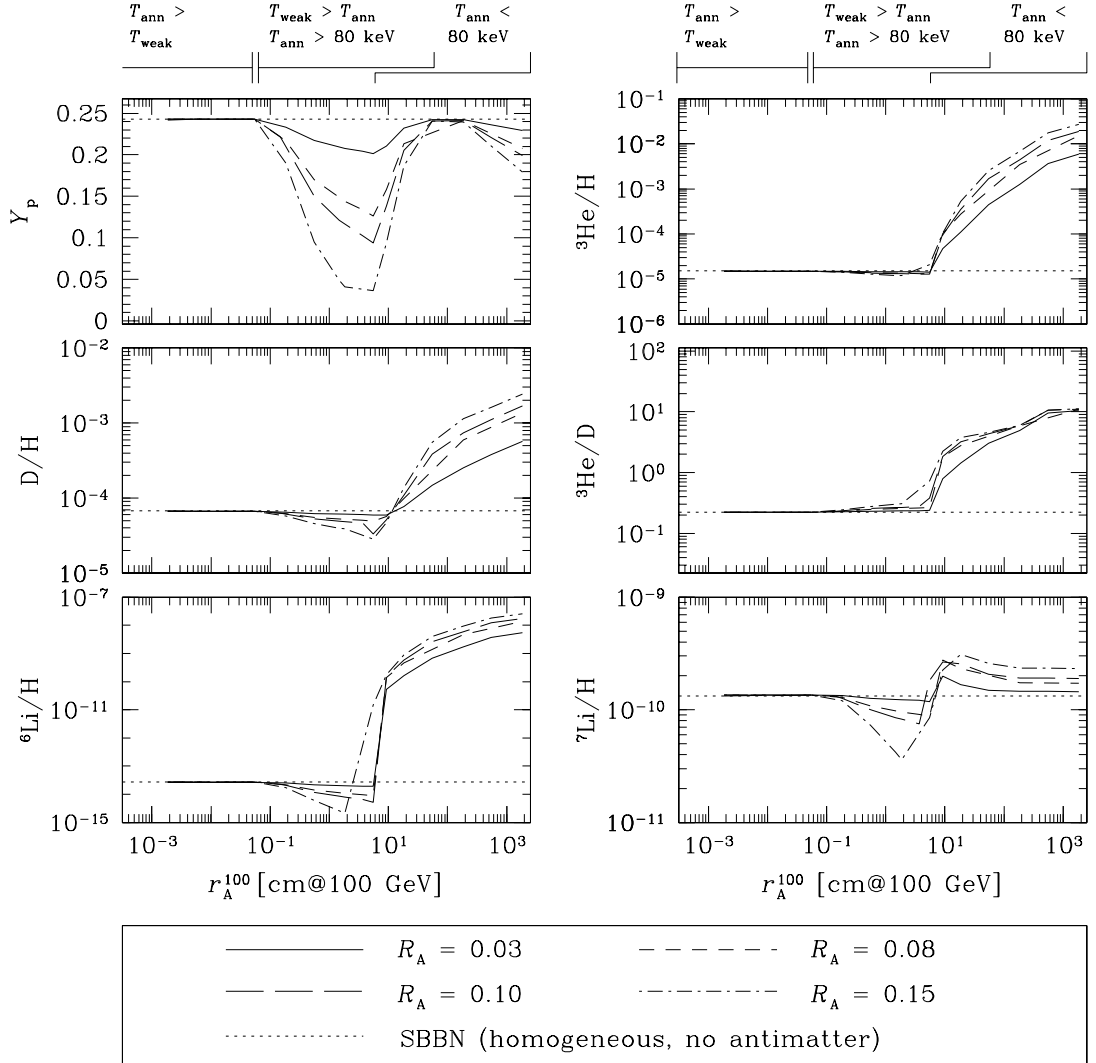


Figure 5.11: Results of BBN calculations in a Universe with antimatter domains. Shown are the ^4He mass fraction, the abundances of D, ^3He , ^6Li and ^7Li relative to hydrogen and the ratio of ^3He over D for some intermediate values of R_A (see legend).

$R_A = 10^{-3}$ may already be in conflict with the observations for $r_A^{100} \approx 10^3$ cm. While no generally accepted observational limit for the primordial abundance of ^6Li exists yet, it still seems reasonable to adopt the bound $^6\text{Li}/\text{H} \lesssim 7 \times 10^{-12}$ (cf. Sec. 3.3). In doing so, an antimatter fraction as small as $R_A \approx 10^{-4}$ may be excluded for $r_A^{100} \gtrsim 10^3$ cm (see lower left panel of Fig. 5.10).

The results for intermediate antimatter fractions $0.03 \lesssim R_A \lesssim 0.15$, i.e. still small

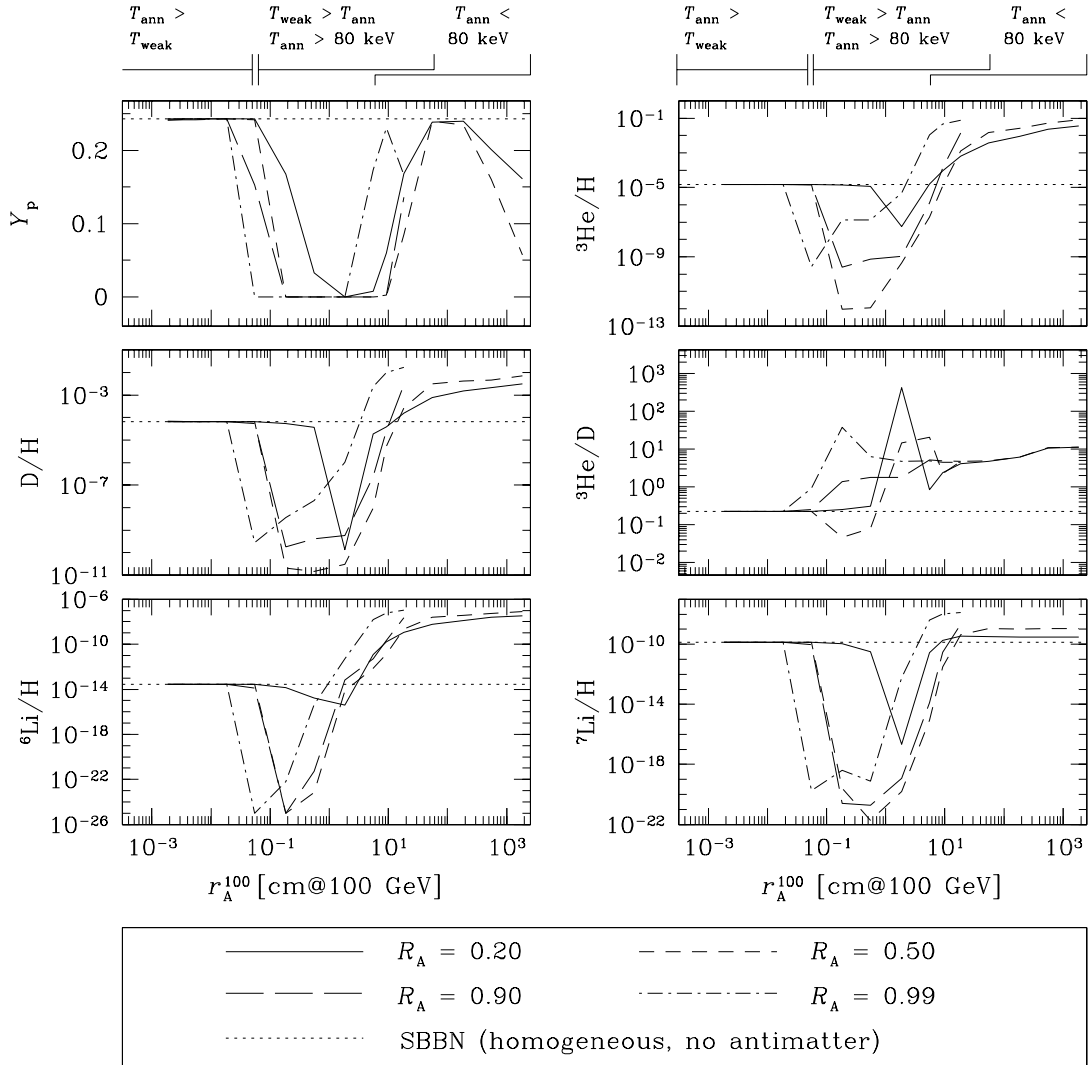


Figure 5.12: Results of BBN calculations in a Universe with antimatter domains. Shown are the ${}^4\text{He}$ mass fraction, the abundances of D, ${}^3\text{He}$, ${}^6\text{Li}$ and ${}^7\text{Li}$ relative to hydrogen and the ratio of ${}^3\text{He}$ over D for high values of R_A (see legend). Note that the abundance yields for extremely large R_A , i.e. $R_A = 0.9$ and $R_A = 0.99$ are only shown for $r_A^{100} \lesssim 20$ cm.

enough to allow for light-element nucleosynthesis in case of early annihilation, are presented in Fig. 5.11. If annihilation occurs at temperatures after weak freeze out but prior to $T_{4\text{He}}$, the ${}^4\text{He}$ mass fraction is strongly decreased, only for antimatter domains of size $r_A^{100} \approx 0.06 - 0.1$ cm consistency with the data may be achieved (top left panel of Fig. 5.11). Whenever the antimatter domains are larger than $r_A^{100} \gtrsim 6$ cm, late time anni-

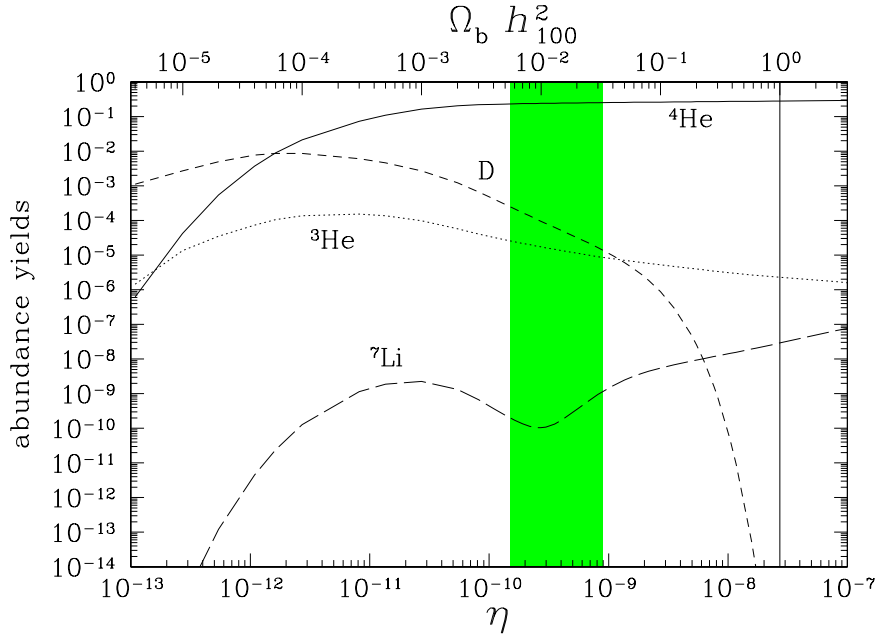


Figure 5.13: Nucleosynthesis yields as a function of η and $\Omega_b h_{100}^2$. Shown are the ${}^4\text{He}$ mass fraction and the number densities relative to hydrogen for deuterium, ${}^3\text{He}$, and ${}^7\text{Li}$. The shaded region marks the SBBN range for the cosmic baryon density while the vertical line indicates a Universe in which the baryon density is as high as the critical density.

hilation will violate the bounds on ${}^3\text{He}/\text{D}$ and ${}^6\text{Li}$, as is apparent in the lower left and middle right panel of Fig. 5.11.

Even larger antimatter fractions, $0.2 \lesssim R_A \lesssim 0.99$, may only be consistent with the observations in the trivial case of annihilation well before weak freeze out, which leaves enough time for the neutron-to-proton ratio to readjust to the equilibrium value, i.e. for $r_A^{100} \lesssim 2-6 \times 10^{-2}$ cm, depending on the exact value of R_A (Fig. 5.12). Whenever neutron diffusion is effective prior to ${}^4\text{He}$ synthesis, but after weak freeze out, the neutron-to-proton ratio is strongly decreased and an unacceptable low ${}^4\text{He}$ mass fraction will be synthesized, compared to the observations. Complete annihilation off all neutrons and thus a Universe without any pre-galactic ${}^4\text{He}$ or other light-element production is possible for all antimatter fractions $R_A > 0.20$ on some length scale range (see top left panel of Fig. 5.12). This is of course in contradiction with the observations. Late time annihilation of large antimatter fractions results in gross overproduction of the mass two and three elements as well as of ${}^6\text{Li}$, while the ${}^4\text{He}$ mass fraction is again decreased due to the effects of photodisintegration and $\bar{p}{}^4\text{He}$ annihilations.

I do not expect the experimental uncertainties in the annihilation cross sections to significantly affect my results for annihilation prior to ${}^4\text{He}$ synthesis. During that epoch, annihilation mainly proceeds via neutrons, and the annihilation reactions are always

rapid compared to the competing nuclear reactions. The precise value is thus not extremely important, all which counts is that neutrons *do* annihilate. At late times, annihilation proceeds via antiproton-proton, antiproton-nucleus, and proton-antinucleus reactions. In this case, the relative strength of the reactions is of importance, since it determines the fraction of ${}^4\text{He}$ which is annihilated and thus the amount of secondary ${}^3\text{He}$, and of the eventually synthesized ${}^6\text{Li}$. The uncertainty in the theoretical calculations used to obtain the $\bar{p}{}^4\text{He}$ annihilation cross section at low energies (Eq. 4.32 and 4.33) are expected to be approximately around 30 % (K. Protasov, private communication). However, more important are the branching ratios for the production of ${}^3\text{He}$ and deuterium in $\bar{p}{}^4\text{He}$ annihilation which have only little uncertainty (see Tab. 4.2). Altogether I expect the annihilation cross sections uncertainties not to have significant effects on my results.

In the past, the possibility to reconcile BBN with a value for Ω_b as high as unity seemed desirable, but is currently disfavoured by recent CMBR and lensing data, high- z supernova observations, and structure formation theory. The most robust upper bound on the cosmic baryon density from SBBN considerations is set by the deuterium abundance $(\text{D}/\text{H})_{\text{ISM}} \approx 1.6 \times 10^{-5}$ measured in our vicinity, in the interstellar medium (cf. Fig. 3.4). Since BBN is believed to be the only significant source for deuterium in the Universe (Epstein, Lattimer & Schramm 1976), at least that amount of deuterium has to be produced in the early Universe and thus $\Omega_b^{\text{SBBN}} h_{100}^2 \lesssim 3 \times 10^{-2}$ ($\eta_{\text{SBBN}} < 9 \times 10^{-10}$). For reference, Fig. 5.13 shows the abundance yields as a function of η for a wide range from 10^{-13} to 4×10^{-7} . Also indicated on the top axis are the corresponding values for $\Omega_b h_{100}^2$.

It is nevertheless still of interest, whether the SBBN upper bound on the cosmic baryon density might be relaxed in models with antimatter domains. As I have shown, annihilation of antimatter domains may well reduce Y_p , either by decreasing the n/p ratio prior to ${}^4\text{He}$ synthesis or by direct late time annihilation on, and photodisintegration of, ${}^4\text{He}$ nuclei. It is thus possible to produce the observed ${}^4\text{He}$ mass fraction of $Y_p \approx 0.24$ with arbitrarily large values for η_{net} . But in neither of the two cases the observational data for deuterium, ${}^3\text{He}/\text{D}$, and ${}^7\text{Li}$ may be matched. In a Universe at high baryonic density, ${}^7\text{Li}$ is greatly overproduced (see Fig. 5.13). The dominant production channel at high values of η_{net} is ${}^3\text{He}(\alpha, \gamma){}^7\text{Be}$, followed by the eventual decay to ${}^7\text{Li}$ much later in the evolution of the Universe. At a temperature slightly below $T_{4\text{He}} \approx 80$ keV the ${}^7\text{Be}$ nucleus may however easily be transformed by neutrons into ${}^7\text{Li}$ via ${}^7\text{Be}(n, p){}^7\text{Li}$, which is in turn subject to destruction by protons. But free neutrons after the synthesis of ${}^4\text{He}$ are neither available in the standard BBN scenario, nor in a scenario with matter-antimatter domains. In contrast, Domínguez-Tenreiro & Yepes (1987) and Yepes & Domínguez-Tenreiro (1988) found that homogeneous, exponential injection of antimatter by, e.g., the hadronic decay of some exotic particle with a life time such that the decay occurs at a temperature of $T_{\text{dec}} \approx 50$ keV may lead to a substantial ${}^7\text{Li}$ destruction. Free neutrons may now arise directly in the decay and may be provided via ${}^4\text{He}$ disruption. Thus ${}^7\text{Be}$ may be transformed to ${}^7\text{Li}$ and subsequently be destroyed at that temperature by thermal protons. Due to the occurrence of the ‘gap’ in the annihilation time, or temperature, scale, which is characteristic for a scenario with annihilating domains (see Fig. 5.8), this

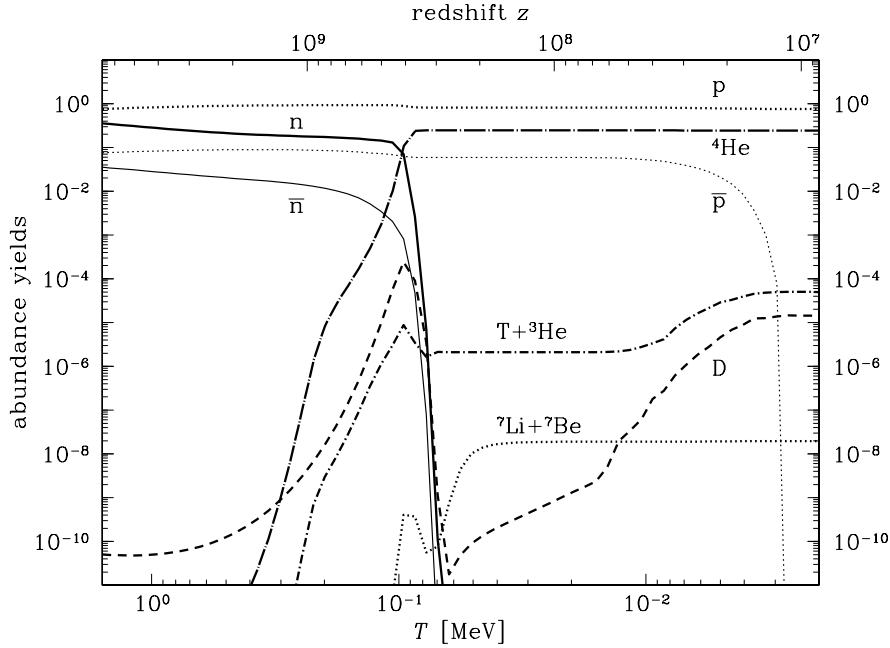


Figure 5.14: Abundance yields as a function of temperature for $R_A = 0.1$, $r_A^{100} = 3.6$ cm in a Universe with $\Omega_b = 1$. Shown are the mass fractions of $n(\bar{n})$, $p(\bar{p})$ and ${}^4\text{He}$, and the number density of $T + {}^3\text{He}$ and of ${}^7\text{Li} + {}^7\text{Be}$ relative to hydrogen.

process of ${}^7\text{Li}$ destruction is not effective in the scenario studied in this work and the ${}^7\text{Li}$ abundance remains high for high cosmic densities. Also the deuterium yields in a high η_{net} Universe with matter-antimatter domains does not match the observations. Generally, deuterium is extremely low for high values of η_{net} (see Fig. 5.13). In case of early annihilation where no additional deuterium may be produced, the yields are typically below the SBBN results. Significant amounts of deuterium may only be produced via late time annihilation on ${}^4\text{He}$, but in that case the abundance yields conflict with both the ${}^3\text{He}/\text{D}$ and ${}^6\text{Li}$ data. This may be seen in Fig. 5.14, where I show a simulation for Universe with $\Omega_b h_{100}^2 = 1$. While $Y_p \approx 0.24$ and D/H is very close to the observationally acceptable range, the ${}^3\text{He}/\text{D}$ ratio exceeds unity and the ${}^7\text{Li}$ abundance is much too high. A Universe with significantly higher baryon density is thus not readily achievable in the scenarios with antimatter domains studied in this work.

Even if I drop the assumption of a Universe in which the baryon-, or antibaryon-, to-photon ratio has initially the same value throughout the Universe, and furthermore allow the antimatter fraction and domain length scale to take different values at different locations in space, it still seems very difficult to match the observational constraints in a Universe with η_{net} well in excess of the SBBN value. Let us assume that the Universe consists of two different types of regions. In regions of type A with net baryon-to-photon ratio η_{net}^A , the antimatter fraction is high, $R_A \lesssim 0.25$, and mixing is effective between weak freeze out and $T_{4\text{He}} \approx 80$ keV. Note that irrespective of the value for η_{net}^A

the region consists of protons only, after the annihilation is complete. In region B, with net baryon-to-photon ratio η_{net}^B , antimatter domains are larger, so they annihilate after the BBN epoch and light element synthesis may take place. If I further assume that region B is at high baryonic density, $\eta_{\text{net}}^B \gg \eta_{\text{SBBN}}$, the production of deuterium and ${}^3\text{He}$ is negligible prior to annihilation (cf. Fig. 5.13). Mass 2 and 3 elements will however be produced during the course of late time annihilation of \bar{p} on ${}^4\text{He}$. It is then easily feasible to find a ratio between the volumes of the two regions such that the average ${}^4\text{He}$ mass fraction \bar{Y}_p is diluted to the observed value of $Y_p \approx 0.24$,

$$\bar{Y}_p \approx \frac{(Y_p)_B}{1 + \frac{\eta_{\text{net}}^A V_A}{\eta_{\text{net}}^B V_B}}, \quad (5.14)$$

where $V_{A,B}$ are the volumes of the two zones, respectively. The ${}^4\text{He}$ mass fraction converges to $Y_p \approx 0.36$ for high baryonic densities, the required dilution factor is thus at most $(Y_p)_B/Y_p \approx 1.5$ in order to obtain $Y_p \approx 0.24$. While the ${}^4\text{He}$ mass fraction may again be matched in such a model for an arbitrarily large average baryon density, we face the same problems with production of deuterium, ${}^3\text{He}$ and ${}^6\text{Li}$ via late time annihilation as discussed above for a one zone model. Furthermore, in region B, ${}^7\text{Li}$ is produced well in excess of the observed values and the dilution by mixing with the proton-only zones of type A may not reduce the ${}^7\text{Li}$ abundance by more than a factor of 1.5. From my results, it thus seems very unlikely that a valid scenario for a high density Universe might be possible.

Chapter 6

Big Bang Nucleosynthesis and Antimatter

– Summary and Conclusions –

In this work I have studied the mixing and subsequent annihilation of antimatter domains in the early Universe during a period from a cosmological temperature of about 10 MeV, well above the epoch of weak freeze out, down to the formation of neutral hydrogen (recombination) at about 0.2 eV. Such distinct domains of antimatter may arise in some electroweak baryogenesis scenarios (Comelli et al. 1994, Giovannini & Shaposhnikov 1998a), and also in other baryogenesis scenarios (for a review see e.g. Dolgov 1996). Annihilation of antimatter domains may substantially modify the light element abundances as compared to the predictions of a standard Big Bang Nucleosynthesis, or SBBN, scenario. Any valid scenario for the evolution of the early Universe has however to reproduce the primordial light element abundances as they are inferred from observations. Due to the remarkable success of the SBBN scenario, only comparably small variations of the predicted abundances are tolerable. One may thus derive stringent constraints on the existence of small-scale matter-antimatter domains during early cosmological epochs. A second aspect of my work is that the presence of small amounts of antimatter, separated from matter within some length scale regime may, in fact, even improve the agreement between BBN theory and observations.

In order to properly simulate the evolution of the early Universe in the presence of antimatter domains, I developed a numerical code. This code describes, on the background of the expansion of the Universe, the thermodynamic evolution, all relevant nuclear reactions, baryon-antibaryon annihilations, and the dissipation processes which lead to mixing of the matter and antimatter regions. To this end, I substantially modified an inhomogeneous nucleosynthesis code originally developed by Jedamzik & Fuller (1994), as described in the appendix. Actual mixing of matter and antimatter over the domain boundary is always accomplished by baryon diffusion on a typical length scale much smaller than the size of the domains. Thus the annihilation occurs in a small annihilation region close to the boundary. Transport of baryon number over

distances of the order of the domain sizes towards the annihilation region is controlled by two different physical processes. As long as baryonic density gradients in the early Universe may be supported by opposing temperature gradients, transport of baryon number is described by baryon diffusion. Below a temperature of a few keV, the photon mean free path increases enormously, temperature and thus pressure gradients may not be maintained any more. Existing baryon density gradients are quickly washed out by hydrodynamic expansion of regions at higher baryonic density towards the low density annihilation region. The epoch, when antimatter regions of some specific size annihilate thus either depends on the baryon diffusion time scale, or on the hydrodynamic expansion time scale.

Annihilation of antimatter domains at different times during the evolution of the Universe may have different consequences. For annihilations occurring prior to the incorporation of neutrons into ${}^4\text{He}$, which takes place at a temperature of about 80 keV, annihilation proceeds via neutron diffusion. Protons remain however confined to the matter region, since their diffusion length is much shorter. Thus annihilation occurs preferentially on neutrons. This may lead to a decrease of the neutron-to-proton ratio, which in turn leads to a reduction of the primordially synthesized ${}^4\text{He}$ mass fraction, as compared to the SBBN scenario. In contrast, if annihilation occurs after the completion of ${}^4\text{He}$ synthesis, free neutrons are not longer abundant and annihilation mainly proceeds via protons. Apart from antiproton-proton annihilations, annihilation on, and photodisintegration of, the now abundant light nuclei is also possible. In particular, the antimatter induced disruption and the photodisintegration of ${}^4\text{He}$ nuclei yields energetic ${}^3\text{He}$ and deuterium nuclei. This may lead to an increase of the abundances of these nuclei beyond observationally allowed values. Further, energetic ${}^3\text{He}$ nuclei may also produce an appreciable amount of ${}^6\text{Li}$.

The two most important aspects of my results are summarized in Figs. 6.1 and 6.2. Let me first discuss my results in view of constraining the presence of antimatter domains in the early Universe, as presented in Fig. 6.1. Shown are the regions in the parameter plane spanned by the antimatter fraction, R_A , and the length scale of the antimatter regions, r_A^{100} , where observationally acceptable abundance yields for the light elements result. Note that all length scales in this work are given on a comoving scale fixed at a temperature of 100 GeV (see Sec. 4.1). Since there still exists some degree of controversy about the actual primordial abundances, I will interpret my results twice; once from a conservative and once from a more speculative angle. While there is currently a lively debate about which of the two independent ${}^4\text{He}$ determinations reflects the primordial value (see Sec. 3.3), it seems reasonable to assume a ${}^4\text{He}$ mass fraction not lower than $Y_p \approx 0.22$ (Olive et al. 1997). I will thus employ this value as a lower bound. Similarly, the primordial deuterium abundance derived from observations is still controversial, even though the majority of scientists working in this field would probably tend towards the ‘low’ value of $\text{D}/\text{H} \approx 3.4 \times 10^{-5}$ determined in quasar absorption spectra (Burles & Tytler 1998b). The situation is even worse for ${}^3\text{He}$, since the chemical evolution of ${}^3\text{He}$ over the history of the Universe is only poorly understood. Thus no reliable limit on the ${}^3\text{He}$ abundance alone may be invoked. These problems may however be avoided if the constraint ${}^3\text{He}/\text{D} < 1$ is used (Sigl et al. 1995). This

limit together with $Y_p < 0.22$ constitutes the conservative data set, which I have used to derive limits on the antimatter domain parameters as shown in Fig. 6.1. High antimatter fractions, $R_A \gtrsim 0.1$ may only be consistent with the observationally inferred light element abundances if annihilation occurs close to weak freeze out, i.e. $r_A^{100} \lesssim 10^{-1}$ cm. In this case, the weak interactions are still rapid enough to at least partially reproduce any annihilated neutrons and thus drive the n/p ratio back towards the SBBN value. Antimatter fractions larger than $R_A \gtrsim a\ few\ 10^{-2}$ on length scales $r_A^{100} \gtrsim 10^{-1}$ cm result in an unacceptable low ${}^4\text{He}$ mass fraction, $Y_p < 0.22$, which is indicated by the black shaded region. Even larger antimatter regions, $r_A^{100} \gtrsim 6$ cm, annihilate at least partially via $\bar{p}{}^4\text{He}$ disruptions. Since the destruction of only a minute fraction of ${}^4\text{He}$ leads to an observationally unacceptable enhancement of the ${}^3\text{He}/\text{D}$ ratio, the limits on the allowed antimatter fraction in this regime may be as stringent as $R_A \lesssim a\ few\ 10^{-4}$ for length scales $r_A^{100} \gtrsim 2 \times 10^2$ cm (dark grey shaded region).

Recently, a number of ${}^6\text{Li}$ abundance determinations have been reported for stars in the disk and in the halo of our galaxy (Smith, Lambert & Nissen 1998, Nissen et al. 1999, Cayrel et al. 1999). All observations are consistent with a ${}^6\text{Li}/{}^7\text{Li}$ ratio of about 0.05, implying a ${}^6\text{Li}/\text{H}$ ratio of $\sim 7 \times 10^{-12}$. Energetic ${}^3\text{He}$ nuclei may lead to the formation of ${}^6\text{Li}$ via nonthermal reactions (Dimopoulos et al. 1988, Jedamzik 1999). Provided that ${}^6\text{Li}$ has not been depleted in these stars, I may significantly tighten the constraints on the amount of antimatter by requiring that pre-galactic production of ${}^6\text{Li}$ is not to exceed the above value. This leads to an improvement of the limit on R_A by up to two orders of magnitude as is evident from the light grey shaded region of Fig. 6.1. Nevertheless, due to the loophole of possible ${}^6\text{Li}$ depletion in stars, this limit should be regarded as tentative at present.

The limits derived from annihilations below $T \lesssim 4.5 \times 10^{-5}$, corresponding to antimatter domain sizes of $r_A^{100} \gtrsim 10^3$ cm, have to be interpreted with care, since the photodisintegration yields in that regime are uncertain due to the unknown photon spectrum (see Sec. 5.5). But even if I completely ignore photodisintegration, meaningful limits due to direct production of ${}^3\text{He}$ (and the subsequent ${}^6\text{Li}$ synthesis) via ${}^4\text{He}$ disruption by antiprotons may still be derived. These limits are indicated by the dashed lines in Fig. 6.1. Due to the increasing inefficiency of photodisintegration at low temperatures, both limits converge for large antimatter domain sizes.

Note that the limits derived here on the basis of the ${}^3\text{He}/\text{D}$ and ${}^6\text{Li}$ data are also of relevance for scenarios where antimatter is homogeneously injected into the plasma, for example by the decay of a relic particle after the nucleosynthesis epoch, since they rely on the production of these nuclei from ${}^4\text{He}$ disruption and photodisintegration. Both processes are generic for scenarios with injection of antimatter. Nevertheless, the efficiency of transport of the produced ${}^3\text{He}$ nuclei away from the annihilation region is particular to a scenario with individual domains. Furthermore, the reduction of the ${}^4\text{He}$ mass fraction also only applies to models where antimatter is confined to well defined domains. Only in this case annihilation proceeds via baryon diffusion and thus the differential diffusion of charged and neutral baryons may lead to a significant decrease of the neutron-to-proton ratio prior to the epoch where ${}^4\text{He}$ is formed.

For comparison, I have also shown in Fig. 6.1 the limits on annihilation which may

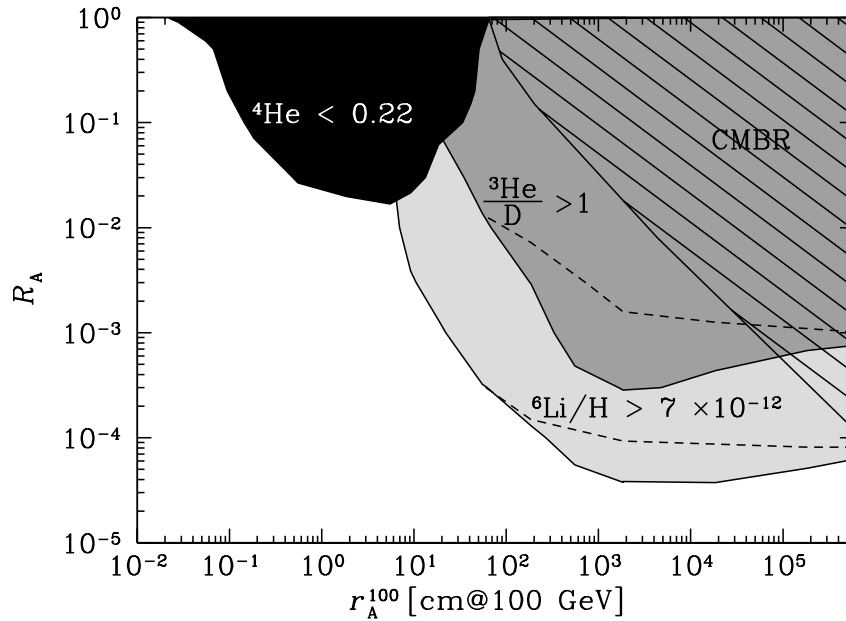


Figure 6.1: Limits on the presence of antimatter in the early Universe. Parameter combinations within the black shaded region result in a ${}^4\text{He}$ mass fraction below 0.22, while in the dark grey shaded region the bound ${}^3\text{He}/\text{D} < 1$ is violated. The excluded range is extended by the light grey shaded region, if one adopts the tentative bound ${}^6\text{Li}/\text{H} < 7 \times 10^{-12}$. The dashed lines indicate the results when ${}^4\text{He}$ photodisintegration is ignored. Also shown are the usually weaker limits on the presence of antimatter from CMBR considerations (hatched region).

be derived from the upper limits on distortions of the spectrum of the cosmic microwave background radiation (CMBR). The very precise CMBR data allow one to place constraints on the amount of non thermal energy input at redshifts below $z \approx 3 \times 10^6$. Each annihilation transforms about 2/3 of the rest mass of the particles into electromagnetic energy, thus the limits given in the right panel of Fig. 2.4 may directly be converted into a limit on R_A , which is indicated by the hatched region in Fig. 6.1. Here, I used the scale given in Fig. 5.8 to associate an annihilation redshift with a particular antimatter domain size r_A^{100} . Using the above conservative data set, I find stronger limits than the ones provided by the CMBR data for annihilations occurring at temperatures above $T_{\text{ann}} \gtrsim 10^{-6} \text{ MeV}$ ($r_A^{100} \lesssim 10^5 \text{ cm}$), corresponding to a redshift of $z \gtrsim 4 \times 10^3$. If I adopt the ${}^6\text{Li}$ bound, the presence of antimatter is more tightly constrained by BBN considerations, rather than by CMBR considerations, for the whole parameter range down to the recombination epoch at $z \approx 10^3$.

Apart from providing stringent constraints on the parameters of putative scenarios which predict antimatter domains in the early Universe, I find that the existence of antimatter domains within some length scale regime may, in fact, improve the agreement

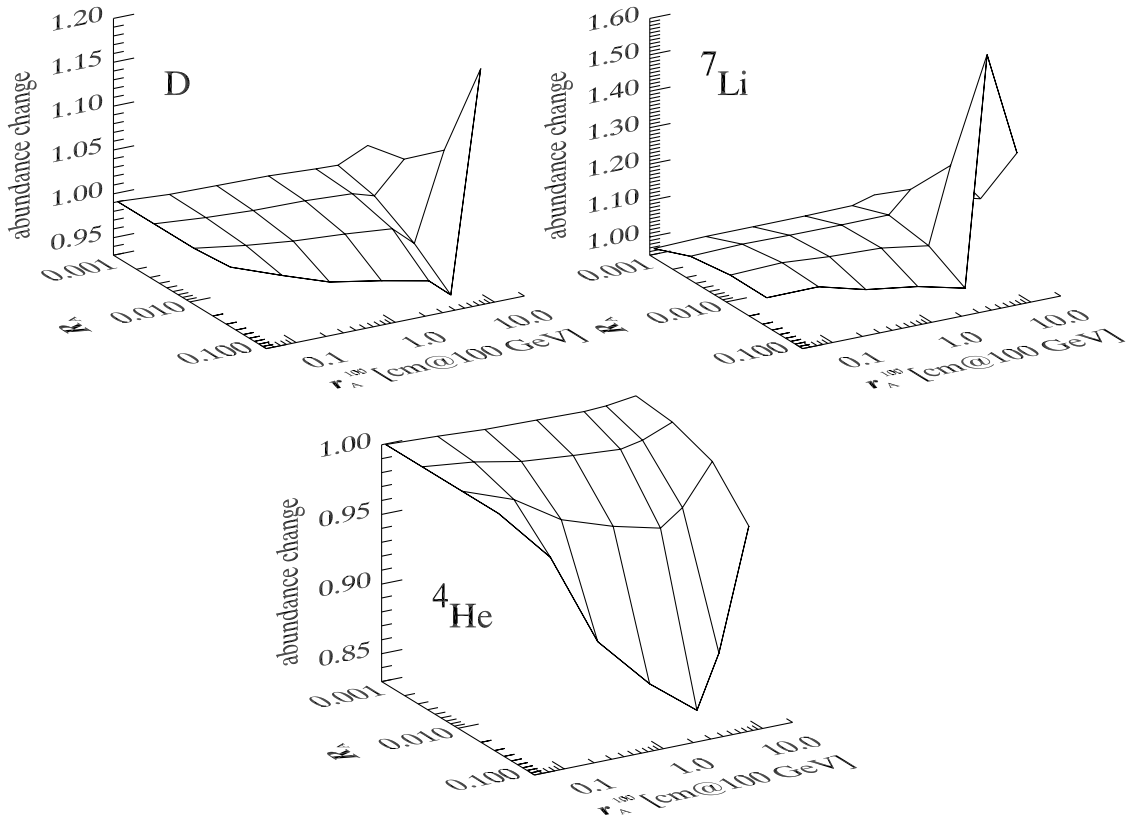


Figure 6.2: Relative change of the light element abundances in a Universe with annihilating antimatter domains as compared to a SBBN scenario at the same net baryon-to-photon ratio of $\eta = 3.4 \times 10^{-10}$. Shown are the ratios of the deuterium, ${}^4\text{He}$, and ${}^7\text{Li}$ mass fractions to their corresponding SBBN values as a function of antimatter fraction R_A and domain length scale r_A^{100} .

between the predicted and observational inferred light element abundances. In particular, the currently favoured ‘low’ deuterium determination in quasar absorption systems, and the long standing, ‘low’ ${}^4\text{He}$ value require mutually inconsistent values of η within the framework of SBBN. This discrepancy might be healed, if a mechanism to reduce the ${}^4\text{He}$ mass fraction by about 5 % as compared to the SBBN prediction was active in the early Universe. This may be achieved by a small admixture of antimatter domains in the early Universe which annihilate after weak freeze out, but before effective ${}^4\text{He}$ synthesis takes place. I display in Fig. 6.2 the relative change of the abundances for deuterium, ${}^4\text{He}$, and ${}^7\text{Li}$. Shown are the respective mass fractions as a function of the antimatter fraction R_A and domain length scale r_A^{100} , divided by the unperturbed mass fraction obtained in an SBBN calculation using the same baryon-to-photon ratio. Thus a ‘low’ ${}^4\text{He}$ at the central value of $Y_p \approx 0.234$ (Olive et al. 1997) is possible for a baryon-to-photon ratio of $\eta \approx 5 \times 10^{-10}$, which corresponds to the low deuterium abundance

measured in high redshift quasars, $D/H \approx 3.4 \times 10^{-5}$ (Burles & Tytler 1998b).

Finally, it is of some interest to contemplate if a BBN scenario with matter-antimatter domains may reconcile the observationally inferred element abundances with the theoretically predicted ones for a baryonic density exceeding the upper bound from SBBN, $\Omega_b h_{100}^2 \lesssim 0.02$. In the standard BBN scenario, such a Universe suffers from overproduction of ${}^4\text{He}$ and ${}^7\text{Li}$, and from too little synthesized deuterium. In a scenario with annihilating antimatter domains, there exist two possibilities to reduce the primordial ${}^4\text{He}$ mass fraction to the observed value. Early annihilation, prior to ${}^4\text{He}$ synthesis, may reduce the n/p ratio and thus the ${}^4\text{He}$ mass fraction synthesized, while during late annihilation ${}^4\text{He}$ nuclei may be destroyed via antiproton induced disruption and via photodisintegration. At first sight, the possibility to achieve observationally acceptable ${}^4\text{He}$ mass fractions at high baryon-to-photon ratios looks promising. But upon closer inspection, some severe shortcomings of such models arise. Scenarios at high net baryon-to-photon ratio and with annihilation prior to ${}^4\text{He}$ formation still overproduce ${}^7\text{Li}$ relative to the observational constraints. Furthermore, no additional source of deuterium exists in this model, which is thus ruled out. In the complementary case, where annihilation is delayed until after the epoch of ${}^4\text{He}$ synthesis, production of deuterium and ${}^3\text{He}$ due to disruption and photodisintegration of ${}^4\text{He}$ arises. Even though it is possible to find models where late time deuterium production may reproduce the observationally inferred value, the ratio of ${}^3\text{He}/D$ will exceed unity. This is observationally unacceptable. Further, such a scenario would produce ${}^6\text{Li}$ in abundance, which is most likely in conflict with recent observations. I thus conclude that it seems difficult to relax the SBBN upper bound on Ω_b by the existence of antimatter domains in the early universe.

Appendix

Numerical Methods

In this appendix I will describe some aspects of the numerical code which I used to simulate the evolution of the early Universe in the presence of matter and antimatter regions. The task of performing detailed numerical Big Bang Nucleosynthesis calculations was first fulfilled by Wagoner et al. (1967). In the present code, the nuclear reaction network and the thermodynamic evolution of the homogeneous radiation background is treated as in an updated version of this original code (Kawano 1992). Jedamzik & Fuller (1994) developed a code to describe the evolution of subhorizon-scale baryon-to-photon fluctuations in the early Universe and the resultant modifications of the light element abundances. To this end, the BBN network was coupled to all relevant hydrodynamic processes (see Sec. 4.2.3), such as diffusion of baryons, photon diffusive heat transport, neutrino heat transport and late-time hydrodynamic expansion of high-density regions. In this work, I extended the code used by Jedamzik & Fuller (1994) to include antielements and adapted it to the present problem.

Short Description of the Numerical Code

The nuclear reactions are described by a set of coupled differential equations (Eq. 3.9),

$$\frac{\partial n_i}{\partial t} = \sum_{k,l} \langle \sigma v \rangle_{kl} n_k n_l - \sum_j \langle \sigma v \rangle_{ij} n_i n_j.$$

As in the original Wagoner code, these equations are written in form of a matrix equation, which is solved by Gaussian elimination. The right hand side of the above equation consists of small differences of very large numbers, due to the near equality of the forward and reverse rates at high temperatures. This would require very small time steps and eventually lead to numerical instabilities, as is discussed e.g in the *Numerical Recipes* (Press, Teukolsky, Vetterling & Flannery 1992). The suggested cure is to use implicit differencing, which utilizes the derivative at the new time step as opposed to explicit differencing, which evaluates the derivative at the old time step. This method is absolutely stable.

Since the nuclear reaction rates depend not only on the nuclear densities, but also on the thermal energy of the nuclei, as well as on the electron and positron density in

the case of the weak interactions, the thermal evolution of the early Universe has to be calculated parallel to the matrix evaluation. The thermal history of the early Universe is described by the Friedmann-Equation (Eq. 3.4),

$$H^2 \equiv \left(\frac{\dot{R}}{R} \right)^2 = \frac{8\pi G}{3} \sum_i \varepsilon_i(t).$$

As long as the energy densities of the various species are given by a highly relativistic equilibrium distribution with negligible chemical potential, the thermal evolution is straightforward to calculate. But when electrons and positrons start to become non-relativistic and annihilate below temperatures of $T \lesssim 1$ MeV, the equilibrium distribution function cannot be solved in closed form. At this time, their entropy is transferred to the radiation component and the adiabatic cooling of radiation is slowed down until annihilation is complete. This process has to be followed in detail, since it happens during the time of BBN and thus affects the elemental abundances. In order to calculate the electron and positron densities, the distribution functions have to be integrated numerically. This is done using modified Bessel functions (see e.g. Abramowitz & Stegun 1972). The condition of charge neutrality allows the calculation of the electron chemical potential. Cosmic temperature, nuclear density and electron chemical potential are evolved using a second order Runge-Kutta driver to ensure the required stability and accuracy (for details see again Press et al. 1992). This procedure requires to perform all computations twice for each single time step.

To allow for inhomogeneities in the baryon density, Jedamzik & Fuller (1994) modified the original code in that they introduced a Lagrangian grid of zones in which the various thermodynamic quantities and the nuclear densities may deviate from the respective horizon average value. In order to describe the diffusion of neutrons, an extra term was added in the evolution equation for the nuclear densities. Since neutron diffusion and incorporation of neutrons into nuclei also proceeds on a very fast time scale, it was again necessary to treat neutron diffusion implicitly. Further, neutrino and photon heat transport and hydrodynamic processes were included in the code. The evolution of density fluctuations was treated in a simple intuitive manner. Each zone was taken to be initially in pressure equilibrium. This pressure equilibrium configuration is characterized by temperature and baryonic density fluctuations in each zone. Diffusive processes during a time step will change the temperatures and baryonic densities in the different zones. This will perturb the existing pressure equality and will result in an adiabatic expansion or contraction of the zones, until pressure equilibrium is reestablished at new values for the temperatures and densities. When the photon mean free path becomes larger than the size of the fluctuations, the assumption of pressure equilibrium breaks down, since temperature gradients cannot be maintained any more. In this regime, the pressure gradients result in local accelerations of the fluid elements. The expansion of high density regions is rapid compared to the Hubble time and has to be treated with great numerical care. The fluid velocities rapidly obtain terminal velocities due to photon-electron Thomson drag (see Sec. 4.2.3), thus acceleration times may be neglected and the terminal velocities treated as being attained instantaneously.

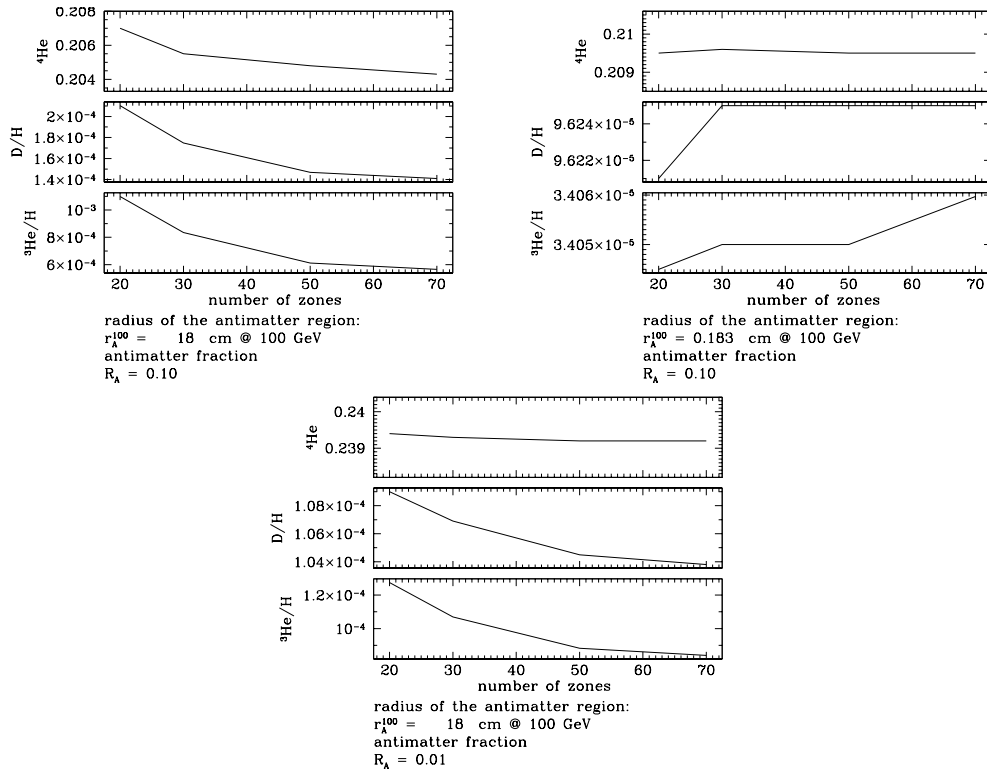


Figure A.1: Element abundances obtained in simulations with three different combinations of the antimatter parameters (see legend). The number of zones was varied between 20 and 70 to check for convergence of the results. See text for discussion.

The terminal velocities are determined by balancing local pressure-gradient-induced stresses against radiation drag forces (see Jedamzik et al. (1994) for details regarding this procedure).

In order to treat the evolution of small-scale antimatter regions numerically, I further modified Jedamzik's code. Specifically, the matrix describing the nuclear reactions had to be extended to incorporate antielements. Since I also examine scenarios where antimatter is still present during the epoch of BBN, synthesis of antielements may also occur. Thus, antielements up to ${}^7\overline{\text{Be}}$ have to be taken into account and not only matter-antimatter annihilations, but also antimatter-antimatter reactions had to be included. It turned out, that diffusion of nuclei is of importance and has to be treated implicitly, owing to the potentially fast diffusion and annihilation processes. The treatment of diffusion of all nuclei and antinuclei up to ${}^4\text{He}$ and ${}^4\overline{\text{He}}$ is now fully implicit. Besides the antielements, pions and pion-nucleon interactions are also included in the matrix.

Spatial Resolution and Baryon Number Conservation

I use a set of concentric spherical shells with radii $r_{100,i}$ and (anti-)nuclear densities $n_{\bar{b},i}$ and $n_{b,i}$, respectively, to describe the distribution of matter and antimatter. Initially, all zones have identical baryon, or antibaryon, density and photon temperature. The number of zones in the simulations has to be chosen such, that the spatial resolution of the volume is sufficient to adequately describe the relevant physical processes. The simulation volume is divided in n_z zones with equal volume. If the number of zones covering the antimatter regions is smaller than about 25% of the total number of zones, I slightly modified the initial zoning to guarantee sufficient resolution of the antimatter region. In such a case the antimatter region is described by $n_z/4$ zones with equal volume. The matter region then contains another $n_z/4$ zones of the same volume and the rest of the simulation volume is filled with $n_z/2$ zones with exponentially increasing volume. It turned out that 30 zones are sufficient to resolve diffusion of the nuclei and obtain reasonable convergence in the final abundances (see Fig. A.1). The region where most of the annihilations occur, on the other hand, has not been resolved in my simulations. The results should be fairly insensitive to the actual structure of the thin annihilation layer, as I discussed in Sec. 4.2.2.

With the initial conditions mentioned above, not all of the parameters can be chosen independently. In my simulations, I use the following three physical parameters as independent variables: (1) the size of the antimatter regions r_A^{100} , (2) the initial matter-to-antimatter ratio R_A , which is defined as the ratio of the total amount of antimatter $N_{\bar{b}}$ to the total amount of matter N_b ,

$$R_A = \frac{N_{\bar{b}}}{N_b} = \frac{\sum_{i=1}^{n_z} n_{\bar{b},i} (r_i^3 - r_{i-1}^3)}{\sum_{i=1}^{n_z} n_{b,i} (r_i^3 - r_{i-1}^3)} \quad (\text{A.1})$$

and (3) the net baryon density

$$n_{\text{net}} = \frac{\sum_{i=1}^{n_z} (r_i^3 - r_{i-1}^3) (n_{b,i} - n_{\bar{b},i})}{(r_{100}^{\text{cell}})^3}. \quad (\text{A.2})$$

Further, I define the volume filling factor $f_{\bar{b}} \equiv (r_A^{100})^3 / (r_{100}^{\text{cell}})^3$. Here, r_A^{100} and r_{100}^{cell} are the radius of the antimatter region and the total radius of the simulation volume, respectively. Thus, with the assumption of identical initial matter and antimatter densities in the respective zones, $n_b(r_{100} > r_A^{100}) = n_{\bar{b}}(r_{100} < r_A^{100})$, I obtain

$$n_b(r_{100} > r_A^{100}) = n_{\bar{b}}(r_{100} < r_A^{100}) = \frac{1}{1 - 2f_{\bar{b}}} n_{\text{net}}, \quad (\text{A.3})$$

The radius r_{100}^{cell} is used to adjust the matter-antimatter ratio to the desired value, after the radius of the antimatter region has been set, and is thus given by

$$r_{\text{cell}} = \frac{r_A}{\sqrt[3]{R_A / (1 + R_A)}}. \quad (\text{A.4})$$

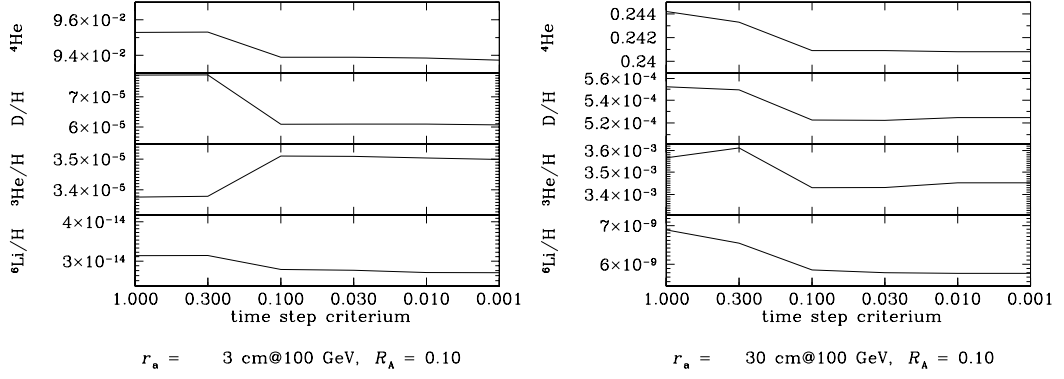


Figure A.2: Element abundances obtained in a simulation with 30 zones and different values for the time step determination criterium c_y , which is described in the text.

The whole procedure of solving the nuclear reaction matrix and the treatment of the hydrodynamical processes is included in the Runge-Kutta scheme, i.e. it has to be done twice per time step. The results of the two Runge-Kutta steps are averaged at the end of each time step. Since not only the densities within each zone, but also the radii of the zones may change, this has to be done very carefully in order to minimize errors. An adequate independent check of the numerical simulations is the achieved accuracy in baryon number conservation. Generally, the baryon number, which is defined as

$$\left| \frac{\sum_{i=1}^{n_z} (n_{b,i} - n_{\bar{b},i})(r_i^3 - r_{i-1}^3)}{n_{\text{net}}(r_{100}^{\text{cell}})^3} - 1 \right|, \quad (\text{A.5})$$

is conserved on the level of $\Delta N_b/N_b \lesssim \mathcal{O}(10^{-6})$ for those regions of the parameter space relevant for the derivation of my limits. Only for large antimatter fractions, $R_A \gtrsim 0.5$ on length scales $r_A^{100} \gtrsim 10$ cm, numerical conservation of baryon number deteriorates. It seems however very unlikely to find an observationally acceptable scenario for combinations of the parameters in that range such that the simulation of such scenarios is of little interest.

Determining the Time Step

I also tested the stability of the results against relaxing or tightening the time step determination criterium c_y . The new time step is determined on the basis of the abundance change for each element during the old time step,

$$\Delta t_i = \left| \frac{Y_i(t)}{\frac{dY_i(t)}{dt}} \right| c_y \left[1 + \left(\frac{\log(Y_i(t))}{\log(Y_{\text{min}})} \right)^2 \right]. \quad (\text{A.6})$$

The code utilizes another time step determination criterium, c_t , which limits the size of the time steps on grounds of change of the cosmic temperature,

$$\Delta t = \left| \frac{T}{\frac{dT}{dt}} \right| c_t. \quad (\text{A.7})$$

In Fig. A.2, I show the results for six different values of c_y . The second time step criterium c_t was fixed at $c_t = 2 \times 10^{-3}$ for $c_y \leq 0.1$, at $c_t = 2 \times 10^{-2}$ for $c_y = 0.3$, and at $c_t = 1$ for $c_y = 1$. Reasonable convergence of the abundances is reached for $c_y = 0.1$ and $c_t = 2 \times 10^{-3}$. These values were thus used in the simulations presented in this work.

Bibliography

- Abramowitz M. & Stegun I.S. (Eds.): *Handbook of mathematical functions*, Dover Publications Inc., New York (1972)
- Adams T.F., *Astron. Astrophys.* **50** (1976) 461
- Aharonian F.A., Kirillov-Ugryumov V.G. & Varadanian V.V., *Astrophys. Sp. Science* **115** (1985) 201
- Ahlen S. et al., *Nucl. Instrum. Meth.* **A350** (1994) 351 (*Sov. Astron. Lett.* **4** (1978) 4)
- Alcock C.R. et al., *Phys. Rev. Lett.* **64** (1990) 2607
- Alpher R.A. & Herman R., *Phys. Today* (1988) 24
- Alpher R.A., Bethe H. & Gamow G., *Phys. Rev.* **73** (1948) 803
- Alpher R.A., Follin Jr J.W. & Herrmann R.C., *Phys. Rev.* **92** (1953) 1347
- Aly J.J., *Astron. Astrophys.* **64** (1978) 273
- Anderson C.D., *Phys. Rev.* **43** (1933) 491
- Applegate J.H., Hogan C.J. & Scherrer R.J., *Phys. Rev.* **D35** (1987) 1151
- Armstrong T. et al., *Phys. Rev.* **D36** (1987) 659
- Bahcall N.A., Lubin L.M. & Dorman V., *Astrophys. J.* **447** (1995) L81
- Balestra F. et al., *Nuovo Cim.* **100A** (1988) 323
- Banerjee B. & Chitre S.M., *Phys. Lett.* **B258** (1991) 247
- Batusov Yu.A. et al., *Nuovo Cim. Lett.* **41** (1984) 223
- Berezinskii V.S., Bulanov S.V., Dogiel V.A. & Ptuskin V.S.: *Astrophysics of cosmic rays*, Amsterdam: North-Holland, 1990, edited by Ginzburg, V.L. (1990)
- Bertin A. et al. (OBELIX Collaboration), *Phys. Lett.* **B369** (1996) 77
- Boezio M. et al., *Astrophys. J.* **487** (1997) 415
- Bogomolov E.A. et al., in: *Proceedings, 16th International Cosmic Ray Conference, Kyoto*, Vol. 1 (1979)
- Bonifacio P. & Molaro P., *Mon. Not. Roy. Astron. Soc.* **285** (1997) 847
- Burles S. & Tytler D., *Astrophys. J.* **499** (1998a) 699
- Burles S. & Tytler D., *Astrophys. J.* **507** (1998b) 732
- Burles S., Kirkman D. & Tytler D., *Astrophys. J.* **519** (1999) 18
- Carbonell J. & Protasov K., *Hyperfine Interactions* **76** (1993) 327

- Carbonell J. & Protasov K.V., *Z. Phys. A* **355** (1996) 87
- Carbonell J., Protasov K.V. & Zenoni A., *Phys. Lett.* **B397** (1997) 345
- Carswell R.F., Weymann R.J., Cooke A.J. & Webb K.J., *Mon. Not. Roy. Astron. Soc.* **268** (1994) L1
- Cayrel R. et al., *Astron. Astrophys.* **343** (1999) 923
- Chaboyer B. & Demarque P., *Astrophys. J.* **433** (1994) 510
- Chamberlain O., Segre E., Wiegand C. & Ypsilantis T., *Phys. Rev.* **100** (1955) 947
- Chandrasekhar S. & Henrich L.R., *Astrophys. J.* **95** (1942) 288
- Chechetkin V.M., Khlopov M.Yu. & Sapozhnikov M.G., *Riv. Nuovo Cim.* **5** (1982a) 1
- Chechetkin V.M., Khlopov M.Yu., Sapozhnikov M.G. & Zel'dovich Ya.B., *Phys. Lett.* **B118** (1982b) 329
- Cohen A., de Rújula A. & Glashow S., *Astrophys. J.* **495** (1998) 539
- Cohen A.G. & de Rújula A., *Astrophys. J.* **496** (1998) L63
- Cohen A.G., Kaplan D.B. & Nelson A.E., *Ann. Rev. Nucl. Part. Sci.* **43** (1993) 27
- Combes F., Fassi-Fehri O. & Leroy B., *Astrophys. Sp. Science* **37** (1975) 151
- Comelli D., Pietroni M. & Riotto A., *Nuc. Phys.* **B412** (1994) 441
- Corradini M. (Obelix Collaboration), in: *Proceedings of the 4th Biennial Conference on Low Energy Antiproton Physics, Dinkelsbühl, Germany* (Edited by Koch H., Kunze M. & Peters K.), Vol. 56 A of *Nuc. Phys. B Proc. Suppl.* (1997)
- Danese L. & De Zotti G., *Astron. Astrophys.* **107** (1982) 39
- Dearborn D., Steigman G. & Tosi M., *Astrophys. J.* **465** (1996) 887
- Dekel A., *Ann. Rev. Astron. Astrophys.* **32** (1994) 371
- Dekel A., Burstein D. & White S.D.M., in: *Critical Dialogues in Cosmology. Proceedings of a Conference held at Princeton, New Jersey* (Edited by Turok N.), World Scientific (1997), p. 175
- Dimopoulos S., Esmailzadeh R., Hall L. & Starkmann G., *Astrophys. J.* **330** (1988) 545
- Dirac P.A.M., *Proc. Roy. Soc. Lond.* **126** (1930) 360
- Dirac P.A.M., *Proc. Roy. Soc. Lond.* **A133** (1931) 60
- Domínguez-Tenreiro R., *Astrophys. J.* **313** (1987) 523
- Domínguez-Tenreiro R. & Yepes G., *Astrophys. J.* **317** (1987) L1
- Dolgov A., *Phys. Rep.* **222** (1992) 309
- Dolgov A. & Pagel B., *New Astronomy* **4** (1999) 223
- Dolgov A. & Silk J., *Phys. Rev.* **D47** (1993) 4244
- Dolgov A.D., in: *Proceedings of International Workshop on Future Prospects of Baryon Instability Search in p -Decay and $n \rightarrow \bar{n}$ Oscillation Experiments, Oak Ridge, TN, USA ; 28 - 30 Mar 1996* (Edited by Ball S.J. & Kamyshev Y.A.), National Laboratory, Oak Ridge (1996), p. 101 (available as hep-ph/9605280)
- Edmunds M.G., *Mon. Not. Roy. Astron. Soc.* **270** (1994) L37
- Ellis J. et al., *Nuc. Phys.* **B373** (1992) 399

- Ellis J., Nanopoulos D.V. & Sarkar S., *Nuc. Phys.* **B259** (1985) 175
- Epstein R.I. & Petrosian V., *Astrophys. J.* **197** (1975) 281
- Epstein R.I., Lattimer J.M. & Schramm D.N., *Nature* **263** (1976) 198
- Falco E.E., Kochanek C.S. & Muñoz J.A., *Astrophys. J.* **494** (1998) 47
- Fields B.D. & Olive K.A., *New Astronomy* **4** (1999) 255
- Fixsen D.J. et al., *Astrophys. J.* **473** (1996) 576
- Fuller G.M., Mathews G.J. & Alcock C.R., *Phys. Rev.* **D37** (1988) 1380
- Gaisser T.K. & Schaefer R.K., *Astrophys. J.* **394** (1992) 174
- Gamow G., *Phys. Rev.* **70** (1946) 572
- Geiss J., in: *Origin and Evolution of the Elements* (Edited by Prantzos N., Vagioni-Flam E. & Cassé M.), Cambridge University Press, Cambridge, UK (1993)
- Giovannini M. & Shaposhnikov M.E., *Phys. Rev. Lett.* **80** (1998a) 22
- Giovannini M. & Shaposhnikov M.E., *Phys. Rev.* **D57** (1998b) 2186
- Gisler G.R., Harrison E.R. & Rees M.J., *Mon. Not. Roy. Astron. Soc.* **166** (1974) 663
- Golden R.L. et al., *Phys. Rev. Lett.* **43** (1979) 1196
- Gunderson B., Learned J., Mapp J. & Reeder D.D., *Phys. Rev.* **D23** (1981) 587
- Halm I., *Phys. Lett.* **B188** (1987) 403
- Hayashi C., *Progr. Theo. Phys.* **5** (1950) 224
- Hobbes L.M. & Thorburn J.A., *Astrophys. J.* **491** (1997) 772
- Hobbs L.M. & Thorburn J.A., *Astrophys. J.* **428** (1994) L25
- Izotov Y.I. & Thuan T.X., *Astrophys. J.* **497** (1998a) 227
- Izotov Y.I. & Thuan T.X., *Astrophys. J.* **500** (1998b) 188
- Izotov Y.I., Thuan T.X. & Lipovetsky V.A., *Astrophys. J. Suppl. Ser.* **108** (1997) 1
- Jackson J.D.: *Classical Electrodynamics*, John Wiley & Sons, New York (1975)
- Jedamzik K., *astro-ph/9909445* (1999)
- Jedamzik K. & Fuller G., *Astrophys. J.* **423** (1994) 33
- Jedamzik K. & Fuller G.M., *Astrophys. J.* **452** (1995) 33
- Jedamzik K., Fuller G.M. & Mathews G.J., *Astrophys. J.* **423** (1994) 50
- Kappadath S.C. et al., *Astron. Astrophys.*, *submitted* (1996)
(available at ftp://unhgro.unh.edu/pub/papers/kappadath_cdg_24icrs.ps.gz)
- Kawano L., *FERMILAB-Pub-92/04-A* (1992) (unpublished)
- Kawasaki M. & Moroi T., *Astrophys. J.* **452** (1995) 506
- Khlopov M.Yu. & Linde A.D., *Phys. Lett.* **B138** (1984) 265
- Kinney W.H., Kolb E.W. & Turner M.S., *Phys. Rev. Lett.* **79** (1997) 2620
- Kirkman D. et al., *astro-ph/9907128* (1999)
- Kolb E.W. & Turner M.S.: *The Early Universe*, Frontiers in Physics, Addison-Wesley, Reading, MA (1990)

- Kurki-Suonio H. et al., *Phys. Rev.* **D38** (1988) 1091
- Kurucz R.L., *Astrophys. J.* **452** (1995) 102
- Levshakov S.A. & Kegel W.H., *Mon. Not. Roy. Astron. Soc.* **288** (1997) 787
- Levshakov S.A., Kegel W.H. & Mazets I., *Mon. Not. Roy. Astron. Soc.* **288** (1997) 802
- Levshakov S.A., Kegel W.H. & Takahara F., *Astrophys. J.* **499** (1998) L1
- Levshakov S.A., Agafonova I.I. & Kegel W.H., *astro-ph/9911261* (1999a) (submitted to *Astron. Astrophys.*)
- Levshakov S.A., Kegel W.H. & Takahara F., *Mon. Not. Roy. Astron. Soc.* **302** (1999b) 707
- Lightman A.P., *Astrophys. J.* **244** (1981) 392
- Lindley D., *Mon. Not. Roy. Astron. Soc.* **193** (1980) 593
- Lindley D., *Phys. Lett.* **B171** (1986) 235
- Malaney R.A. & Mathews G.J., *Phys. Rep.* **229** (1993) 145
- Mathews G.J., Alcock C.R. & Fuller G.M., *Astrophys. J.* **349** (1990) 449
- Meyer J.P., *Astron. Astrophys. Suppl.* **7** (1972) 417
- Mitchell J.W. et al., *Phys. Rev. Lett.* **76** (1996) 3057
- Moiseev A. et al. (BESS collaboration), *Astrophys. J.* **474** (1997) 479
- Molaro P., Bonifacio P., Centurion M. & Vladilo G., *Astron. Astrophys.* **349** (1999) L13
- Mutchler G.S. et al., *Phys. Rev.* **D38** (1988) 742
- Nissen P.E., Lambert D.L., Primas F. & Smith V.V., *Astron. Astrophys.* **348** (1999) 211
- Nollet K.M., Lemoine M. & Schramm D.N., *Nuc. Phys. C* **56** (1997) 1144
- Olive K.A., Skillman E. & Steigman G., *Astrophys. J.* **483** (1997) 788
- Ormes J.F. et al. (BESS collaboration), *Astrophys. J.* **482** (1997) L187
- Peebles P.J.E.: *Physical Cosmology*, Princeton University Press, Princeton, NJ (1971)
- Peimbert M. & Torres-Peimbert S., *Astrophys. J.* **193** (1974) 327
- Persic M. & Salucci P., *Mon. Not. Roy. Astron. Soc.* **258** (1992) 14
- Pinsonneault M.H., Deliyannis C.P. & Demarque P., *Astrophys. J. Suppl. Ser.* **78** (1992) 179
- Pinsonneault M.H., Walker T.P., Steigman G. & Narayanan V.K., *Astrophys. J.* **527** (1999) 180
- Press W.H., Teukolsky S.A., Vetterling W.T. & Flannery B.P.: *Numerical recipes - the art of scientific computing*, Cambridge University Press, Cambridge, UK, 2nd edition (1992)
- Protheroe R., Stanev T. & Berezhinsky V., *Phys. Rev.* **D51** (1995) 4134
- Ramaty R., Scully S.T., Lingenfelter R.E. & Kozlovsky B., *astro-ph/9909021* (1999)
- Rehm J.B. & Jedamzik K., *Phys. Rev. Lett.* **81** (1998) 3307
- Reno M.H. & Seckel D., *Phys. Rev.* **D37** (1988) 3441
- Riotto A. & Trodden M., *hep-ph/9901362* (1999) (to appear in *Ann. Rev. Nucl. Part. Sci.* **49**, 1999)
- Ryan S.G. et al., *astro-ph/9905211* (1999a)

- Ryan S.G., Norris J.E. & Beers T.C., *Astrophys. J.* **523** (1999b) 654
- Saeki T. et al., *Phys. Lett.* **B422** (1998) 319
- Sakharov A.D., *Pis'ma Zh. Eksp. Teor. Fiz.* **5** (1967) 32 (*J. Exp. Theor. Phys. Lett.* **5** (1967) 24)
- Sarkar S., *Rept. Prog. Phys.* **59** (1996) 1493
- Sato K. & Terasawa N., *Physica Scripta* **36** (1991) 60
- Schramm D.N. & Turner M.S., *Rev. Mod. Phys.* **70** (1998) 303
- Shapiro F.L., *Zh. Eksp. Teor. Fiz.* **34** (1958) 1648
- Sigl G., Jedamzik K., Schramm D.N. & Berezhinsky V.S., *Phys. Rev.* **D52** (1995) 6682
- Smith V.V., Lambert D.L. & Nissen P.E., *Astrophys. J.* **408** (1993) 262
- Smith V.V., Lambert D.L. & Nissen P.E., *Astrophys. J.* **506** (1998) 405
- Songaila A., Cowie L.L., Hogan C. & Rugers M., *Nature* **368** (1994) 599
- Songaila A., Wampler E.J. & Cowie L.L., *Nature* **385** (1997) 137
- Spite F. & Spite M., *Astron. Astrophys.* **115** (1982) 357
- Steigman G., *Cal-Tech Orange Aid OAP* **280** (1972) (unpublished)
- Steigman G., *Ann. Rev. Astron. Astroph.* **14** (1976) 339
- Sunyaev R.A. & Zel'dovich Ya.B., *Astrophys. Sp. Science* **7** (1970) 20
- Tytler D. et al., *Astron. J.* **117** (1999) 63
- Vainer B.V., Dryzhakova O.V. & Naselskii P.D., *Pis'ma Astron. Zh.* **4** (1978) 344
- Vangioni-Flam E. et al., *New Astronomy* **4** (1999) 245
- Vauclair S. & Charbonnel C., *Astron. Astrophys.* (1995) 715
- Vauclair S. & Charbonnel C., *Astrophys. J.* **502** (1998) 372
- Wagoner R.V., *Astrophys. J.* **179** (1973) 343
- Wagoner R.V., Fowler W.A. & Hoyle F., *Astrophys. J.* **148** (1967) 3
- Webb J.K. et al., in: *Structure and Evolution of the Intergalactic Medium from QSO Absorption Line System, Proc. 13th IAP Astroph. Coll.*, Editions Frontières (1997a), p. 345
- Webb J.K. et al., *Nature* **388** (1997b) 250
- Willick J.A., Strauss M.A., Dekel A. & Kolatt T., *Astrophys. J.* **486** (1997) 629
- Yepes G. & Domínguez-Tenreiro R., *Astrophys. J.* **335** (1988) 3
- Yoshimura K. et al., *Phys. Rev. Lett.* **75** (1995) 3792
- Zel'dovich Yu.B., Starobinskii A.A., Khlopov M.Yu. & Chechetkin V.M., *Pis'ma Astron. Zh.* **3** (1977) 208 (*Sov. Astron. Lett.* **3** (1977) 110)

Danksagung

Mein Dank gebührt vor allem meinem Betreuer, Karsten Jedamzik, der immer Zeit für meine Fragen hatte und es immer wieder verstanden hat, mir Spaß an der Arbeit im jungen Universum zu vermitteln. Er hat es mir einerseits ermöglicht selbstständig zu arbeiten, stand mir aber trotzdem immer zur Seite, wenn's mal gar nicht mehr voran ging. Nicht vergessen werden sollen natürlich auch diverse nicht ausschließlich streng wissenschaftlichen Zwecken dienende gemeinsame Unternehmungen, wie zum Beispiel die immerhin teilweise erfolgreichen Versuche so divergierende Sportarten wie Snowboarding und Skifahren unter einen Hut zu bringen.

Hier am Max-Planck-Institut für Astrophysik in Garching habe ich hervorragende Arbeitsbedingungen vorgefunden. Mein besonderer Dank gilt den „Systemleuten“, Norbert Grüner und Hans-Werner Paulsen, die für meine alltäglichen und weniger alltäglichen Computerprobleme immer ein offenes Ohr hatten. Nicht vergessen werden sollen natürlich auch „unsere“ Sekretärinnen Cornelia Rickl, Maria Depner und Kate O'Shea.

Meine beiden Diplomarbeiten-Betreuer Georg Raffelt und Achim Weiß haben mich ermutigt, diese Arbeit anzufertigen, und neben vielen anderen Mitarbeitern hier am Institut zu ihrem Gelingen beigetragen.

Peter Schneider danke ich für die Übernahme des offiziellen Teils der Betreuung, er hat mir damit erst ermöglicht, meine Arbeit hier am Institut anzufertigen.

Ich habe während meiner Zeit hier eine Reihe guter Freunde gefunden; Ignasi, Wendy, Rüdiger, Gerti, Micha, Volker, Andreas, Conrad, Guido und Patrick. Ungezählte Kinobesuche, Studentenstammtische, Kneipen- und Wies'nbesuche und natürlich der schon traditionelle Skiurlaub in den französischen Alpen haben für den hin und wieder nötigen Ausgleich zur Wissenschaft gesorgt.

Very special thanks to Lindsay for reading the whole manuscript and pointing out a few minor typos :-)

Meinem langjährigen Bürokollegen Helmut verdanke ich eine angenehme und teilweise sogar produktive Arbeitsatmosphäre, anfangs noch im „Diplomandenstall“, später dann im inoffiziellen \LaTeX -, idl-, xldb-, etc. Beratungszimmer. Viel Glück weiterhin auf der Suche nach der unentdeckten CPU!

Meine Mutter und mein Vater haben mich während meines gesamten Studiums und auch während der Doktorarbeit immer unterstützt, jeder auf seine Weise, dafür danke ich ihnen.

Ganz speziell gilt mein Dank natürlich dem einen ganz besonderen Menschen in meinem Leben, der in den letzten Jahren den ganzen Stress mit mir geteilt hat und mir besonders am Ende der Arbeit ermöglicht hat, mich ganz und gar auf meine Dissertation zu konzentrieren.

Curriculum Vitae

Persönliche Daten

Name Jan Bernhard Rehm
geboren 29. April 1969 in München
ledig

Ausbildung

1975 – 1977 Montessori Grundschule München
1977 – 1979 Grundschule Brannenburg
1979 – 1982 Ignaz-Günther-Gymnasium, Rosenheim
1982 – 1988 Stiftung Landheim Schondorf
1988 Abitur, Leistungskurse Englisch und Mathematik
1989 – 1990 Grundwehrdienst
1990 – 1992 Studium der Physik an der
Rheinisch-Westfälischen Technischen Hochschule, Aachen
1992 Vordiplom
1992 – 1995 Studium der Physik mit Nebenfach Astronomie an der
Ludwig-Maximilians-Universität, München
1995 – 1996 Diplomarbeit am
Max-Planck-Institut für Astrophysik, Garching
Thema der Arbeit:
„Der Einfluss neuer Neutrinoeigenschaften
auf die Kernsynthese im frühen Universum“
1996 Diplom in Physik
1996 – 2000 Promotionsstipendium am
Max-Planck-Institut für Astrophysik, Garching
2000 Promotion zum Dr. rer. nat. durch die Fakultät für Physik der
Ludwig-Maximilians-Universität, München
